Structural preferences and biomolecular interactions visualized by infrared spectroscopy/mass spectrometry

Structural preferences and biomolecular interactions visualized by infrared spectroscopy/mass spectrometry
Bin Yan
PhD Thesis Radboud University Nijmegen, The Netherlands

Printed by IPSKAMP

ISBN 978-94-6259-636-8

The work in this dissertation was carried out at the Molecular and Laser-Bio Physics groups, Radboud University Nijmegen (The Netherlands). This work was financially supported by the EU ITN network ICONIC, Project No. 238671 and the Netherlands Organisation for Scientific Research (NWO).

Structural preferences and biomolecular interactions visualized by infrared spectroscopy/mass spectrometry

Proefschrift

ter verkrijging van de graad van doctor
aan de Radboud Universiteit Nijmegen
op gezag van de Rector Magnificus prof. dr. Th.L.M. Engelen,
volgens besluit van het college van decanen
in het openbaar te verdedigen op woensdag 13 mei 2015
om 14:30 uur precies

door

Bin Yan

geboren op 23 augustus 1985
te Zhenjiang, China

Promotiecommissie

Promotor:	Prof. dr. David H. Parker Prof. dr. Wim J. van der Zande
Co-promotor:	Dr. Anouk M. Rijs

Manuscriptcommissie:

Prof.dr. Andrei I. Kirilyuk
Prof. dr. Michael Schmitt (Heinrich-Heine-Universität Düsseldorf)
Dr. Thomas L.C. Jansen (Rijksuniversiteit Groningen)

Structural preferences and biomolecular interactions visualized by infrared spectroscopy/mass spectrometry

Doctoral Thesis

to obtain the degree of doctor
from Radboud University Nijmegen
on the authority of the Rector Magnificus prof. dr. Th.L.M. Engelen,
according to the decision of the Council of Deans
to be defended in public on Wednesday, 13 May, 2015
at 14:30 hours

by

Bin Yan

Born on 23 August, 1985
in Zhenjiang, China

Supervisors: Prof. dr. David H. Parker
Prof. dr. Wim J. van der Zande

Co-supervisor: Dr. Anouk M. Rijs

Doctoral Thesis Committee:

Prof.dr. Andrei I. Kirilyuk
Prof. dr. Michael Schmitt (Heinrich-Heine-Universität Düsseldorf)
Dr. Thomas L.C. Jansen (Rijksuniversiteit Groningen)

To my parents, jiyu and my upcoming baby

Contents

1 Introduction

Abstract

This thesis deals with visualizing intramolecular interactions in small biomolecules. These intramolecular interactions drive the formation of structures that allow biomolecules to execute their functions. Visualizing of these interactions in our research takes place through interpretation of the results of infrared spectroscopy and mass spectrometry. The infrared response and molecular fragmentation reveal the relative strengths of different interactions. In this introduction the main class of molecules studied in this thesis is introduced as well as the techniques used during the research.

1.1 Proteins: functionalities and structures

1.1.1 Properties of protein structure

Among the immense collection of functional and structural biomacromolecules, the class of proteins plays a special role. Proteins are ubiquitous in living organisms. Several thousand different functional proteins are found in each cell. Growth, motion, breathing, muscle contraction, immunization, digestion, photosynthesis, transportation of cellular components, sensation, reaction to external changing environment, retention of genetic traits, etc. are just a few examples, which all made possible by specific proteins. The function of each protein is encoded in its structure. The question of structure - function relations of proteins has attracted attention of scientists from various disciplines.

A protein molecule consists of one or more so-called peptide chains, which are strings of different amino acids. Amino acid molecules, the elementary building blocks of proteins, compose the second largest component (water is the largest) of human cells, tissues, etc. Proteins make up about 20% of the weight of human beings. Only 20 standard amino acids are found in our proteins out of the potentially infinite that could be formed by altering the side chain. From the small number of 20 amino acids a huge number of proteins can be built by rearranging their sequence. Nineteen amino acids are built up from a central carbon atom (C_α), with an amino group (-NH_2), a carboxylic acid group (-COOH), a hydrogen atom and a side chain (see Fig 1.1). The 20^{th} amino acid is Proline, in which the side chain connects to the α-carbon, and also to the nitrogen atom forming a cyclic structure. Figure 1.1 shows the chemical structure shared by these 20 amino acids in their L type orientation.

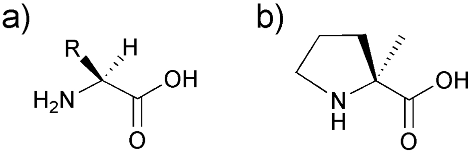

Figure 1.1: General chemical structures of L-type α-amino acids (a) with an exception of L-Proline (b)

One may ask why the proteins are built from only these 20 α-amino acids, rather than β-, γ-amino acids, or the chemically even simpler hydroxyl acids. These 20 α-amino acids form peptide chains in a reaction between the basic amino group and the acid carboxylic acid group, forming a so-called amide linked peptide bond and releasing a water molecule. The formed planar amide bond allows intramolecular hydrogen bonding and stabilizes the higher order protein structures that dictate the functions of these biomolecules. Hydroxyl acids would make up chains upon formation of ester links which would not allow hydrogen bonds. Insertion of β- or γ-amino acids would lengthen the distance between two amide bonds and affect the stability of a peptide backbone. The backbone fold is more compact when the peptide is made of the nature preferred α-amino acids. The hydrogen atom present in the α position of an α-amino acid (except for Proline) helps to reduce steric hindrance when the protein folds into higher order three-dimensional structures. The sequence of amino acids with their different side chains causes the linear chain to fold and curl trying to maximize the interactions between all amino acids. This folding process into a particular spatial configuration forms the essence of the functionality of proteins. Their shape is adapted to the numerous functions they have. The three dimensional realizations of proteins are called conformations.

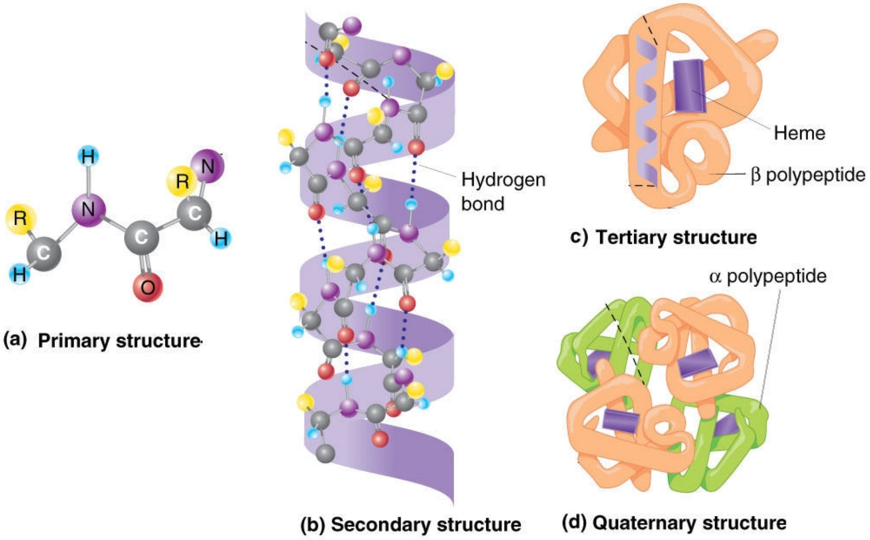

(a) Primary structure

(b) Secondary structure

c) Tertiary structure

(d) Quaternary structure

Figure 1.2: Schematic diagram of four levels of protein structure. The primary structure describes the sequence of amino acid residues in a peptide chain. The secondary structure deals with the formation of local hydrogen bond (such as C_{13} H-bond (the donor and acceptor together with the chain connecting them form a closed 13-members ring) shown here) through interactions between backbone NH and C=O. The tertiary structure refers to the folding pattern (such as α-helix included here) of a whole peptide, caused by not only the local backbone hydrogen bonding, but also the interactions involving side chains. The quaternary structure depicts the composition and connection of the peptide chains making up a whole protein. Figure adopted from *iGenetics*[1]

Theoretically, because of the flexibility of a protein, it can adopt numberless conformations. Under physiological conditions, nearly always a specific conformer is observed, stabilized by the multitude of intramolecular interactions. The study and classification of structures of proteins dates back to a little over 60 years ago. In 1952, the Danish biochemist Kaj Ulrik Linderstrom-Lang defined levels in protein structure. He distinguished a primary, a secondary, a tertiary and a quaternary structure of each protein (as can be seen in Fig. 1.2).[2] The primary structure of protein describes the sequence of amino acid residues in the polypeptide chain. At this moment, of more than one hundred thousand proteins the primary structure is known. The secondary structure refers to the local conformation of the backbone of the polypeptide chain. Intramolecular hydrogen bonding forces segments of a peptide chain to adopt a regular folding pattern. Depending on the number of amino acids involved in forming hydrogen bond and the torsional angles of the backbone, patterns such as an α-helix, a β-sheet, a β-turn or a γ-turn can be observed in the secondary structure of protein, see Fig. 1.3. The tertiary structure refers to the more subtle folding of the whole peptide, including not only forces originating from the backbone but also interactions such as hydrogen bonds involving side chain groups. The tertiary structure refers to the spatial arrangement of all atoms in a peptide chain. When more than one peptide chain is involved in a single protein, the non-covalent bonds between the peptide chains cause them stay together, forming the quaternary structure of the protein.

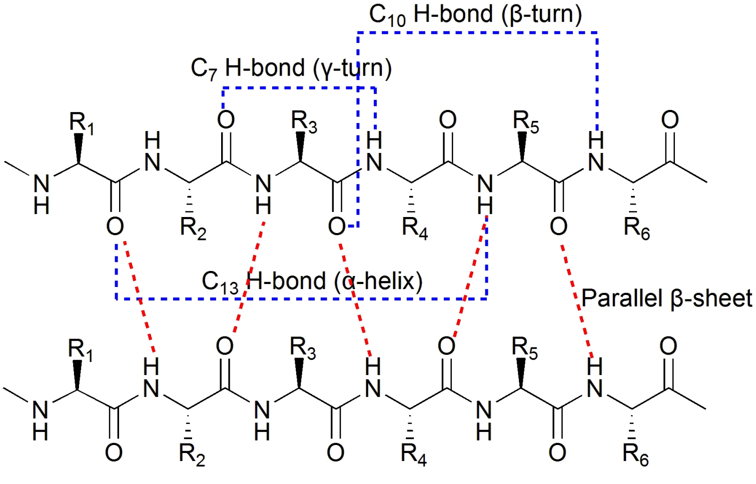

Figure 1.3: Hydrogen bonding schemes in a model peptide chain or between two separate chains. C_7 refers to a γ-turn, C_{10} to a β-turn, C_{13} to a α-helix, and hydrogen bonds between two parallel stretched chains indicated by red dash lines refer to β-sheet.

1.1.2 Forces in stabilization of protein structure

Why does a protein molecule fold into a conformation? What is the meaning of stability of a conformer? Which factors control this process? Of course, the external environment, in the form of the watery matrix or the lipid membranes, influences the 3-dimensional structure adopted by a protein, since interactions of parts of the protein with the environment will compete with intramolecular interactions. But intra-molecular interactions are of prime importance in the folding process. The forces that influence folding and conformational selection are well known and are shown in Figure 1.4.

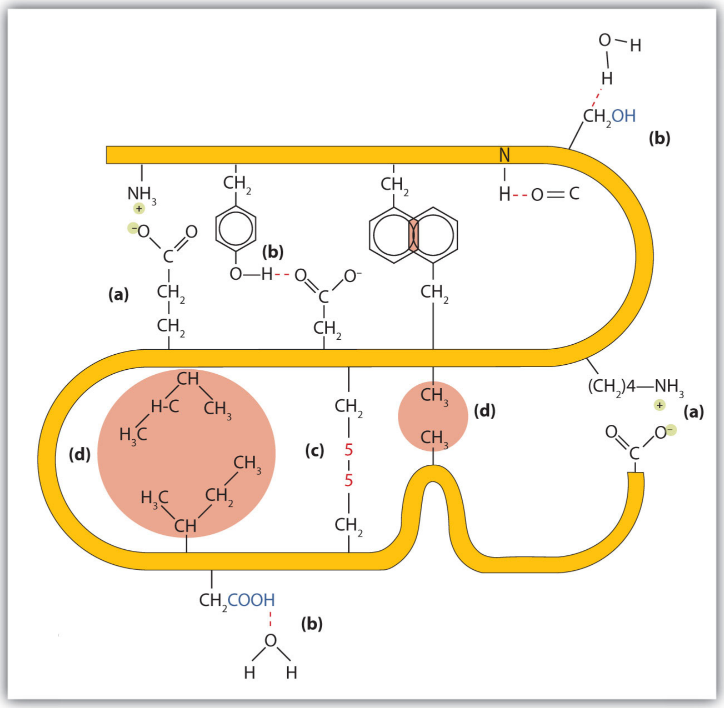

Figure 1.4: Interaction force for stabilization of three dimension structure of protein: (a) ionic bond (salt bridge), (b) hydrogen bond, (c) disulfide linkages, and (d) dispersion forces. Figure adopted from *The Basics of General, Organic, and Biological Chemistry*[3]

The typical bond strength and contribution a bond makes to the stability of a protein structure are summarized in Table 1.1. Traditionally, these energies are expressed in kcal/mol, a unit referenced to the energy needed to heat water. More scientifically used quantities are kJ/mol (1 kcal/mol = 4.2 kJ/mol) or eV/molecule (1 eV/molecule = 96.5 kJ/mol). By using the equation $E=kT$ ($k=8.31$ J/(mol·K)) we can transfer energies to a temperature. Formally speaking a temperature is connected to ensemble energies and is not directly useful, but the temperature associated with a binding energy allows to obtain an estimate of the stability under various circumstances. In the remaining the unit of energy is wavenumber for light or kcal/mol for molecules. Among these, the electrostatic interaction (also called salt bridge interaction, ***main topic of chapter 5***) is the most strong non-covalent interaction. The electrostatic interaction occurs between side chains of opposite charges, for instance a positively charged guanidine side chain of arginine and a negatively charged carboxylic acid side chain of glutamic acid. The electrostatic interaction can also occur between an induced dipole from polar function groups or between an induced dipole and a charged group. Secondly, the hydrogen bond (***main topic of chapter 4***), is everywhere present and due to its directional nature important for stabilization of protein structure. Hydrogen bonds connect an XH group (X=N, O, S etc.) with an atom with large electronegativity. The hydrogen bonds formed by backbone NH and C=O groups, determine the local folding pattern of the peptide chain. A special interaction found to be important in folding and conformational dynamics is the stable but relatively weak covalent disulfide bond. This disulfide bond is found in proteins containing cysteine residues (***relevant peptides discussed in chapter 4***) or methionine residues. The disulfide bond often connects different peptide chains. It is observed that the protein will lose its activity once the disulfide bond is broken. Lastly, the weakest interaction, but one that is present between nearly all atoms, is the Van der Waals force resulting in so-called dispersion interaction (***discussed in chapter 4***). Also the dispersive interaction is important for protein structure. It is an interaction that results from instantaneous dipoles and often appears when group such as NH, SH or OH gets close to phenyl ring (H-π bonding) or two phenyl rings are near each other (π-π stacking).

Table 1.1: Typical bond strength of the commonly seen intramolecular interactions in proteins and their contributions to stabilize the structures of proteins

Type of forces	Bond strength (kcal/mol)	Structural energy lowered (kcal/mol)
Salt bridge	3-8	0.5-5[4]
Hydrogen bond	2-7	0.5-6[5;6]
Disulfide bond	60	1-3[7]
Dispersion interaction	1-2[8]	1-2[9]
Peptide bond	100	Not applicable

1.1.3 Methods for characterization of protein structure

We now know the properties of protein structures and the important interactions that determine folding and stabilize structure. The next question is how to characterize the three-dimensional structure. The most widely used techniques probably are X-ray crystallography (also called X-ray diffraction or XRD) and nuclear magnetic resonance (NMR) spectroscopy. X-ray crystallography emerged as the first reliable technique for elucidating the three dimensional structure of large biomolecules in the early 1950s.[10;11] At this moment, more than 90% of the known protein structures have been determined using X-ray crystallography. The technique requires proteins to be in a crystalline form. The crystal structures may differ from the structure in their native environment e.g. in solution. In practice, a significant amount of purified protein is required for a successful diffraction pattern. These aspects cause that the structures of many proteins await for the arrival of another technique. For proteins that cannot be crystallized, NMR may provide a solution. NMR can be used on proteins in solution and sometimes can reveal even their dynamical behavior. Because of the improved strategies for isotope labeling and continuous development in multidimensional heteronuclear experiments, structural studies on proteins with molecular weights up to 70 kDa are becoming possible.[12–14] However, NMR also requires relatively large amounts of sample.

In addition to the aforementioned methods, aspects of the three-dimensional structure of proteins can be revealed by many other techniques including infrared spectroscopy[15–17], fluorescence methods[18–20], circular dichroism[21;22], 2D-IR[23;24], etc. These methods study the structure of protein in solution, which is the most biologically relevant environment. The structures identified may still differ from those in the native environment. For example, trans-membrane proteins have nonpolar side chains outside and are found in the hydrophobic environment. This is very different with an aqueous solution. Clearly, acquiring the structural properties of a protein molecule while being in the local functional environment is very complicated and no generic solution exists to date.

Apart from the classic techniques for structural determination of proteins, XRD, NMR and solution-based spectroscopic methods, several complementary approaches which rely on gas phase measurements can also be employed to investigate structures of proteins. Properties of biomolecules such as intramolecular interactions, conformational preferences, population distributions, dynamics, etc. are affected by interaction with the environment. Taken out of its natural environment the intrinsic properties not only dominate but can often be studied with much higher precision. Isolating molecules is an accomplishment in itself certainly in the case of large biomolecules. Under the collision free conditions in vacuum, gas phase techniques such as high resolution spectroscopy or mass spectrometry can reveal many of the intrinsic properties of the individual molecules. The gas phase in principle provides a controllable platform to reconstitute in a stepwise manner the environment by adding solvent molecules, metal ions, etc.[25;26]

1.2 Structural characterization of cold and isolated biomolecules

1.2.1 Gas phase study of biomolecules

Gas phase measurements of biomolecules require bringing molecules out of a solid or liquid phase into the gas phase. Heating can only be applied to thermally stable molecules with a sufficiently high vapor pressure. However, most biomolecules do not survive heating. Large molecules decompose upon heating, a process also called pyrolysis. Laser desorption[27;28] has been found to transport large molecules from the complex environment and bring them intact into the gas phase. In 1987, matrix-assisted laser desorption/ionization (MALDI) was discovered and developed. Sample molecules are mixed with a matrix that strongly absorbs the desorption light. Using this technique, large peptides (mass up to 10^6 amu) have been investigated. The developer Koichi Tanaka was awarded one-quarter of the 2002 Nobel Chemistry Prize[29] for this soft ionization technique. The laser desorption method used in our experiments is adapted from this MALDI technique. Here, we use a graphite matrix and a low intense Nd:YAG laser operating at 1064 nm to bring the molecules of interest as neutral molecules into the gas phase. Due to the laser heating the temperature rises rapidly with an estimated rate of $\sim$ 1000 K/ns. This heating process induces a thermal explosion. The fact that large molecules escape intact remains surprising and is attributed to a bottleneck in energy transfer between the matrix and the internal degrees of freedom, and due to the rapid cooling since the desorbed molecules are entrained in a molecular beam supersonic expansion. Nevertheless, some biomolecules for instance the Arginine containing tri-peptides studied in Chapter 5 inevitably partially decompose. Reducing the desorption energy (normally a few μJ) could possibly lower the decomposition ratio, however, at the cost of decreasing the number density of the desorbed molecules.

A method to obtain large charged biomolecules is electrospray ionization (ESI)[29],in which a sample solution is nebulized through a capillary producing charged droplets. The highly charged droplets undergo rapid evaporation and fragmentation by Coulomb explosion. However, this results in isolated, but charged molecules. ESI coupled to mass spectrometry (ESI-MS) is routinely used to determine the primary structure of mass-selected peptide ions. Using collisions in a process called collision induced dissociation (CID)[30;31] or photons in photo-induced dissociation (PID)[32;33], sequence information is obtained. Mass spectrometry can also provide partial information on the structure. Using deuterium gas, hydrogen atoms are replaced by deuterium provided they are accessible in gas phase collisions and hence are on the outside[34;35]. Another technique that can be performed on ions is ion chromatography, in which the shape of integral molecules is deduced from the molecular collision cross-section with an inert buffer gas[36;37].

Although the in vacuo experiment do not directly imitate the environment that nature prefers for functioning of protein, these gas phase methods are still believed to be biologically relevant by adding elements such as ions or individual water molecules. For example, in our study of Adenosine Tri-Phosphate (ATP) hydrolysis by ATPase (ATP hydrolase) at the molecular level (chapter 6), we did not look at the entire protein ATPase. Instead, we characterize the gas phase complex between ATP and an active site mimic of ATPase by ESI ion trap mass spectrometry with CID and IR action spectroscopy. Gas phase measurements minimize the heterogeneity originating from different environment for each molecule in a solution. Besides, because of collision free environment, the lifetime of less stable transition states will become much longer, which allows a study of aquatic unstable systems by using the gas phase. The aforementioned mass-spectrometric based methods lacks conformation selectivity and thus not permit us to gain detailed insight into the conformational structure of charged gas phase biomolecules. Therefore, a spectroscopic technique which involves neutral molecules has been developed to obtain structural information[38;39].

1.2.2 Laser spectroscopy on biomolecules

Spectroscopy probes the quantized absorption of photons, the energy of which depends on a sensitive but sometimes complex manner to molecular structure. In the infrared and far-infrared, the molecular response is especially sensitive to intramolecular interactions as these interactions affect the spring constants within the molecule.

Historically, the first gas phase spectra of biomolecules were acquired in the ultraviolet (UV) region. In the UV region, electronic excitations define the spectrum from which the structure of the molecules can be found indirectly[40]. The particular strength of UV spectroscopy is situated in double resonance techniques such as UV-UV hole burning. In this technique, one can distinguish the presence of different conformers of otherwise identical molecules[41]. Infrared (IR) spectra are more directly connected to structural information and therefore drew more interest. The innovative double resonance spectroscopic technique IR-UV ion dip spectroscopy, together with mass spectrometry, allows us to acquire mass and conformation selected infrared spectra of molecules of interest. With the help of sophisticated quantum chemical calculations, some secondary structural elements of the peptide backbone, such as β- and γ- turns or 3_{10}-helices can be discovered in sample molecules from IR spectra.[42–44] Moreover, the studied system grow in size and complexity (from amino acids, di-, tri- and large peptides to complexes between peptides with water molecules)[38;45–48]. Even when two conformers have an identical electronic spectrum, conformer-specific vibrational spectra can be obtained using an IR-IR-UV triple resonance spectroscopic method[49]. Conformer-specific measurements all require spectra that are highly resolved so that structural information can be extracted efficiently. Highly resolved spectra demand very low internal temperatures in the order of 10 Kelvin, making the use of a solution impossible for these questions.

1.2.3 Low temperature biomolecules

Due to large number of rotational excited and low-energy vibrational excited states at room temperature, IR spectra are broad even for relative small biomolecules. As mentioned above, lowering the molecular temperature simplifies the spectra. At 0 Kelvin under thermal equilibrium conditions all molecules are in the same state. At non-zero temperature, the collection of molecules become distinguishable. Cooling to low temperature in the gas phase is relatively easy.

When a static gas under high pressure (a few bars) is allowed to expand into a vacuum chamber through an orifice, the size of which is larger than the mean free path of the gas, both a narrowing of the velocity distribution and a cooling of the rovibrational degrees of freedom are observed. This process is called a molecular beam supersonic expansion[50]. Since the degree of freedom (n=3) for translation and rotation of nonlinear polyatomic molecules is equal, the cooling effect on these two kinds of molecular motion is very similar, namely

$$\Delta T = 2\Delta E/3R \tag{1.1}$$

for 1 mol molecules, with ΔE a characteristic amount of energy taken away in a single collision .For molecular vibrations, due to its much larger number of degrees of freedom (n=3N-6 with N equals to number of atoms), the cooling effect decreases a lot.

$$\Delta T = 2\Delta E/(3N-6)R \tag{1.2}$$

In addition, as the quantum step between different vibrational levels [0.05-1 ev (∼ 400 - 8000 cm^{-1})] is larger than that between different rotational [0.0005-0.05 ev (∼ 4 - 400 cm^{-1})] or translational levels (continuum), the vibrational cooling efficiency is also for this reason small. In a good expansion, temperatures of ∼ 1 K for the translational degrees of freedom, of a few degrees Kelvin for the rotational degree of freedom and a few tens of degrees Kelvin for vibrations are attained[51].

With the development of the pulsed molecular beam source, in which the orifice is only opened during a short time, the load of the pump to maintain the setup in a low pressure is reduced and measurements are performed in which the gas flow is synchronized with pulsed laser methods. Our work on a short-pulse molecular beam valve with high beam density and efficient cooling is described in detail in chapter 3. Moreover, reduction of the temperature yielded several other meaningful results which are not possible under room temperature conditions: 1) different conformers were distinguished and recognized because of high resolution spectra. 2) The energy barrier for conformational conversion and relevant dynamics was investigated. 3) Short life-time intermediate states in conformational dynamics are more stable and were probed. 4) Conformational distributions have been determined for the majority of the peptides studied.

Regarding the last aspect, we observe the number of conformers observed in the laser-desorbed supersonic expansion to be smaller than that of theoretically calculated low energy conformations[52], especially when using Ar as carrier gas. The population distribution over the different conformers in a supersonic expansion is not easily predicted nor characterized. In a thermal equilibrium this distribution is determined by the difference in energy and by the density of vibrational states, the latter being a sort of degeneracy factor, at relevant total energies. An expansion is not expected to produce a distribution that can be described easily by a single temperature. During cooling, the presence of high-lying energetic barriers, that separate different conformers, causes the molecules to undergo vibrational cooling within each conformer geometry without further exchange between different conformers. In fact, for this reason one can observe relatively high lying conformers, whereas other conformers with lower energy have disappeared by further cooling. The studies of small molecules with only several atoms show that the population of a high energy conformer with an isomerization barrier of about 2.9 kcal/mol (1014 cm^{-1}) can be trapped in a supersonic expansion.[53;54] However, for larger molecules such as di- tri- peptides at room or higher temperature, the amount of internal energy stored (many low-frequency modes below 100 cm^{-1} having about a value of kT being about 300 cm^{-1} at room temperature in each mode) is higher and can be used early in the expansion to overcome large barriers to conformational isomerization. Hence, it is reasonable that the number of high-energy conformers observed for larger molecules may be less. The number of measurable conformers is seen to increase when He or Ne is chosen as a carrier gas. He or Ne is expected to remove the internal energy of laser-desorbed species less efficiently than Ar and hence leads to less conformational relaxation.[55;56] As a result, room temperature energetics predicts the conformational distribution after expansion more accurately than zero point energetics does.[57;58]

1.3 IR action spectroscopy

Based on the aforementioned introduction and discussion, it is clear that IR spectroscopy on cold and isolated molecules is selected as the main technique to study three dimensional structures and intramolecular interactions in small peptides. Within IR spectroscopy one records the absorption of infrared light as a function of wavelength. Once the frequency of the radiation matches the energy difference between two stationary states, absorption of this electromagnetic radiation occurs. The vibrational frequencies depend not only on the intrinsic properties of infrared active bonds, but also on the molecular environment. For this reason, knowing the collection of vibrational transitions of a molecule makes it possible to deduce the local interactions and from this knowledge we derive the three dimensional structures of molecules. Gas phase characteristic vibrational frequencies of several structural relevant bonds in peptides are summarized in Figure 1.5 for the amide A and the amide I, II and III regions.

In traditional IR spectroscopy, the intensity of light before and after a sample is recorded as a function of frequency of light (expressed by wavenumber here). Based on the Lambert-Beer Law, an absorbance is then derived, and an infrared absorption spectrum is acquired. This direct absorption measurement requires a measurable difference between incident and transmitted light. However, if the number of molecules under study is very low, the absorbance might simply be unmeasurably small. A solution is lengthening the path of light transmitted such as used in White cell spectroscopy or more advanced in Cavity Ring Down Spectroscopy[62]. Another method is to perform action spectroscopy, in which the absorbance of photons is monitored by another signal instead of a change in light

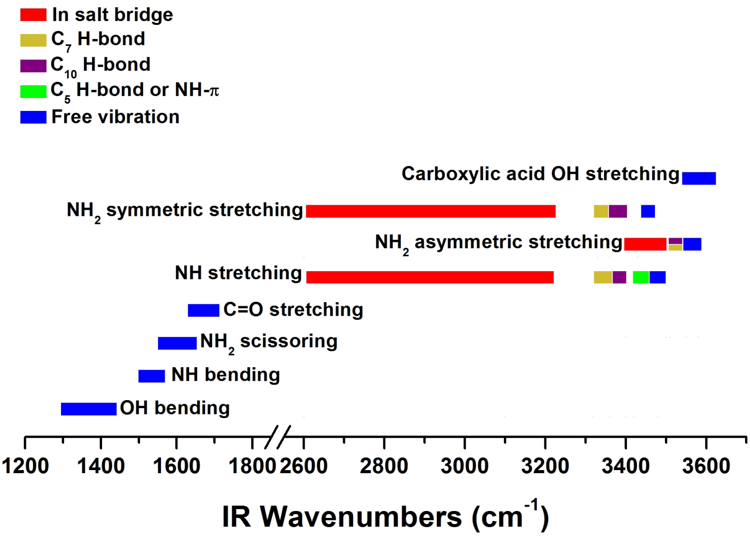

Figure 1.5: Overview of the frequencies of the amide A (NH stretch), amide I (C=O stretch), amide II and III (NH bend) in free and H-bonded interactions, derived from gas phase measurements[59–61] and theoretical calculations using B3LYP/6-311+G(d,p) level of theory.

intensity. In this thesis, we use IR-UV ion dip spectroscopy to acquire vibrational frequencies of samples. In this method the IR response is measured as a change in REMPI (UV) signal. The requirement for this technique to work is that a UV chromophore part of the molecule so that the UV REMPI scheme can be applied.

Action spectroscopy removes the drawback in traditional IR spectroscopy mentioned above. Maybe as important is the fact that action spectroscopy is a non-linear technique as two radiation fields are employed. This non-linearity is necessary to obtain conformation resolved information. More detail about our double resonance spectroscopic technique is discussed in Chapter 2.

1.4 Outline of this thesis

Following this chapter, the experimental setups and methodologies will be discussed in detail in *chapter* 2. First, the setup for acquiring mass-selected conformer specific IR spectra is introduced together with several spectroscopic methods. Subsequently, the theoretical tool based on density function theory (DFT) for geometry optimization and vibrational frequency computation is described. Secondly, another setup employing an ESI ion trap mass spectrometer with CID technique to study molecular level ATP hydrolysis is illustrated. A sigmoid function and energy-dependent kinetic method for data interpretation is discussed at the end.

In ***chapter 3***, a new home-built pulsed molecular beam source called the Nijmegen Pulsed Valve (NPV) is introduced. The NPV operation is based on the Lorentz force created by a pulsed current passing through an aluminum strip located within a magnetic field. Several measurements were performed to characterize the performance of the NPV. The main output characteristics include a short pulse width (as short as 20 μs) combined with operating rates up to 30 Hz. We show that a effectively cooled molecular beam ($\sim$ 1K rotational temperature and $\sim$ 50 for the deduced speed ratio) was generated by the NPV.

In ***chapter 4***, two very similar dipeptides Ac-Phe-Ser-NH2 (FS)(Ser side chain: CH_2OH) and Ac-Phe-Cys-NH2 (FC)(Cys side chain: CH_2SH) were investigated using IR-UV ion dip spectroscopy. This subtle alternation allows us to study the effect of the difference in hydrogen bonding for an OH and SH group, and consequences for the secondary structure. Intramolecular interactions include backbone hydrogen bond and dispersion interactions. Both are found to play an important role in the stabilization of the conformational structures. Besides, due to slight weaker hydrogen bond $SH\cdots O$ in FC than $OH\cdots O$ in FS, two conformers (one with γ-folded backbone and the other with β-turn interaction) were identified for FC while only one (with γ-folded backbone) was observed for FS.

In ***chapter 5***, tripeptides in form of Z-Glu-Xxx-Arg-NH_2 (Xxx = Gly, Ala or Pro) were studied by a double resonance spectroscopic method in order to investigate the effect of backbone flexibility or rigidity on the salt bridge formation and the three dimensional structure of peptides. A salt bridge occurs between a positively and a negatively charged group. In gas phase peptides, this type of interaction occurs when a proton is transferred between two moieties. In a solution, this charge separation is stabilized using the polarizability of the solvent molecules. But also in the gas phase without this stabilization, a salt bridge can be formed if the charges stay in each other's vicinity. Such is the case for the tripeptides studied here. Measured IR spectra are compared with DFT calculated spectra. In addition, the effect of flexibility of the spacing residue (Gly, Ala, Pro: flexible to rigid) between Glu and Arg on the three dimensional structure is also discussed.

In ***chapter 6***, we employ ESI ion trap mass spectrometry together with a CID technique to probe ATP hydrolysis by ATPase on the molecular level. Instead of study the entire protein ATPase, we designed several mimics all representing key elements of the active site of ATPase. The stability of the complex formed by ATP (or other phosphorylated biomolecules) and mimics is first probed by CID. It is found that ATP has a higher binding affinity than other phosphorylated biomolecules for the active site mimics of ATPase, which indicates the binding preference for ATP based on the derived phenomenological binding energies. In addition, for the selected complex which shows not only simple dissociation, but also hydrolysis-like fragmentation, energy-dependent kinetic method is employed to explore the preferences between these different dissociation pathways in CID measurements. Based on the lower activation energy for latter case, hydrolysis-like fragmentation is found to be favored by natural selection. The experiments in this chapter are the first steps towards a detailed illustration of the mechanism of ATP hydrolysis on the active site of ATPase at the atomic level, allowing us to bridge the gap between global and atomic scale. This should ultimately provide more insight into this fascinating system.

Through the studies described above, many meaningful results were obtained, among which the one most worthy to notice should be the formation of salt bridge in gas phase. It is known that under natural conditions proton transfer is supported by water or other polar solvent molecules. However, there was not any experimental evidence for salt bridge formation in gas phase overall neutral peptides until isolated peptides including basic Arg residue and acidic Glu residue were investigated. Previous studies show that lengthening the spacing residue (no intermediate residue to 3 Ala) between Arg and Glu does not affect the salt bridge type and the present backbone interactions. In our study described in chapter 5, we found that with the increase of the size and rigidity of the spacer residue (from Gly, Ala to Pro), proton transfer always occurs although backbone interactions were different. Besides, DFT calculations show that the relative energy of non-zwitterionic structure to zwitterionic structure of capped Glu-Pro-Arg is smaller than that of capped Glu-Ala-Arg or Glu-Gly-Arg, indicating that forming salt bridge becomes more difficult when steric hindrance is higher. Columbic attraction between charged groups is strong enough to overcome the steric hindrance in the folding of a peptide and plays an important role in structural determination.

2 Methods

Abstract

In this chapter the experimental and theoretical techniques used in this thesis will be discussed. First (in Sec. 2.1), the experimental setup which consists of a laser desorption source, a pulsed molecular beam valve and a time-of-flight mass spectrometer will be explained. Employing double resonance spectroscopy, medium high-resolution IR absorption spectra of isolated biomolecules have been acquired using this setup. Secondly (in Sec. 2.2), the computational methods used for the interpretation of the IR spectra will be described. Finally (in Sec. 2.3), the techniques to investigate bond strengths and dissociation pathways of selected complexes as described in Chap. 6 are introduced. These techniques include ion trap mass spectrometry and collision induced dissociation method. In addition, the experimental setup used for Chap. 3 will be discussed in more detail in the chapter itself.

2.1 IR action spectroscopy

Mass and conformation selective IR spectra of biomolecules and oligopeptides are obtained using a laser-desorption molecular beam set-up in combination with various IR and UV based spectroscopic methods. A schematic representation of the set-up is shown in Figure 2.1. To study the intrinsic properties of biomolecules, laser desorption method[46;48;63–65] is employed to bring solid state sample into gas phase as this allows us to study isolated molecules without any external interference, for example resulting from solvent molecules. A pulsed molecular beam of noble gas entrains the desorbed molecules into the supersonic expansion to cool them down into their lower vibrational and rotational levels.[65–69] The molecular beam is skimmed 10 cm downstream into a reflector time-of-flight mass spectrometer where ions are created by UV one color resonance enhanced multi-photon ionization (REMPI) scheme or IR-UV double resonance technique and subsequently detected. Scanning the UV wavelength in one color or IR wavelength in two color scheme and monitoring the ion signal, well-resolved UV and IR spectra could be obtained for a specific mass. Finally, by comparing experimental with calculated IR spectra, structures are assigned to the investigated neutral conformers. In the following sections, each step will be elucidated in more detail.

2.1.1 Laser desorption source

The experiments described in this thesis are performed in the gas phase. As mentioned earlier, most biomolecules and oligopeptides are solids at room temperature and desintegrated upon heating. Ideally there is a substantial vapour pressure at room temperature such that part of the solid sample can be converted into gas phase directly. For molecules which are thermally stable, it is also possible to heat the sample to produce a proper vapour pressure. Nevertheless, for molecules with a low vapour pressure and thermally labile samples, laser desorption is the method of choice to bring the sample into gas phase as intact molecules.

Laser desorption, initially developed for mass spectrometry, normally requires a mix of large biological sample and intense UV light absorbing matrix such as 2,5-dihydroxybenzoic acid (DHB), etc.[70] However, in our experiments, we aim to produce the sample molecules in their neutral state, which means that we want to prevent proton transfer to occur between matrix and sample. In addition, the sample of interest should be transparent at the desorption light wavelength to avoid fragmentation. Therefore, combination of near-infrared light for desorption[71] and graphite[72] for matrix is an ideal option to fulfil these requirements.

In the laser desorption source of our setup, a small amount (a few milligrams) of powder of sample and fine graphite are mixed homogeneously in a ratio of about 5:1 under dry conditions and then applied onto the surface of a solid graphite sample bar (50 × 15 × 1 mm). This solid graphite sample bar is placed directly under the orifice of a pulsed valve, on a translation stage which is moving

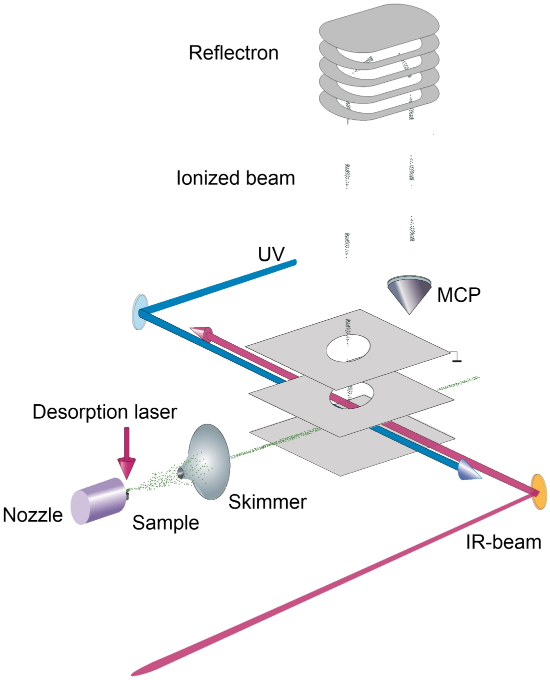

Figure 2.1: Experimental setup consisting of pulsed molecular beam valve equipped with a laser desorption source and a time-of-flight mass spectrometer.

horizontally at a speed of ~5 μm/s to provide a fresh sample every laser shot. As a result, each sample bar which is 50 mm long, lasts for 2 - 3 hours of continuous measurement (or 10^5 laser shots) before it needs to be replaced. In addition, the position of sample bar can also be aligned vertically to optimize the focus of desorption laser and the distance to the nozzle orifice so that the sample will be in the most efficient cooling part of the supersonic molecular beam. For desorption, a pulsed Nd:YAG laser (Polaris II, New Wave research) with a pulse energy of about 1 mJ and width of 5 ns at wavelength of 1064 nm is focused on the surface of sample bar. Although the mechanism is not fully understood, we believe that the graphite particles absorb the infrared photons and the temperature rises very rapidly which leads to a thermal explosion around the irradiated area. As a result, sample molecules and graphite are ejected in the gas phase. Because of short, nanosecond of heating time (of about 1000 K/ns), the whole process occurs under thermal non-equilibrium conditions so sample molecules are ejected before fragmentation can take place. After desorption, the isolated gas-phase molecules are introduced into a temporally synchronized supersonic jet molecular beam for cooling.

2.1.2 Supersonic molecular beam source

Laser desorption is a very powerful tool to bring a wide range of samples into gas phase. The molecule of interest can be studied under isolated conditions where information about intrinsic properties could be acquired without any interference from intermolecular interaction with its environment.

However, with this method, the molecules enter the gas phase at temperatures of several hundreds Kelvin,[73;74] which would result in very congested absorption spectra because a large number of vibrational and rotational states are populated each contributing to an absorption signature. For better spectra, the desorbed molecules have to be cooled down both vibrationally and rotationally. The molecular beam technique, in which the molecules are seeded in a supersonic expansion of a noble gas, is often used to generate such kind of cold and isolated molecules.[75–79]

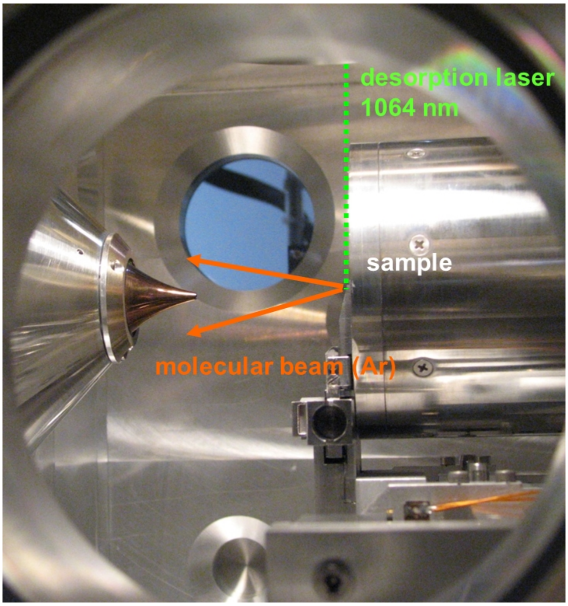

Figure 2.2: A picture of source chamber of experimental setup (the schematic drawing can be seen as the region between nozzle and skimmer in Fig. 2.1). The desorbed molecules are entrained into the Ar molecular beam and cooled down inside supersonic expansion before entering into ionization region through the skimmer.

A supersonic molecular beam is generated when a noble gas (here: Argon) is expanded from a certain backing pressure through a small opening or nozzle into a high vacuum chamber.[50] Considering the limited pumping capacity of the experimental apparatus and the synchronization requirement of pulsed laser detection methods, pulsed sources are more widely used to create cold molecular beam with high density. In our setup, a commercially available Jordan valve (R.M. Jordan Co.) is used. The working principle of this valve is based on magnetic repulsion between two metal strips through which a large opposing current is sent.[80] Operated at 10 Hz, it is capable of producing 100 μs pulses. In addition, because of frequent collisions inside the supersonic expansion, the cooling effect in the molecular beam could be very efficient. The whole process is able to produce sample molecules with a translational temperature below 1 Kelvin[81], while the rotational and vibrational temperatures will usually be around 2 - 5 Kelvin and 10 - 50 Kelvin, respectively[65;82;83]. Nevertheless, all the molecules of interest could be brought to their vibrational ground state at these temperatures, leading to the possibility to accomplish high-resolution spectroscopy where absorptions from different vibrational levels or different conformations can be well resolved. For visual impression, a picture of source chamber is shown in Figure 2.2, in which a laser desorption source is coupled to pulsed molecular beam producing cooled molecules of interest which can fly through a skimmer (2 mm) efficiently.

2.1.3 Spectroscopic techniques

Once the molecular beam enters into the region between repeller and extractor of the TOF mass spectrometer, a laser ionization method must be applied to convert molecules of interest from the neutral to the ionic state for later detection. For molecules with a UV chromophore (such as a phenyl group in our sample molecules), the ideal way to ionize it is via UV REMPI. However, for molecules which do not absorb in the UV region, VUV one photon ionization is an alternative method. No matter which technique is selected, an intense laser beam is a prerequisite. For the experiment presented in this thesis, the UV beam is produced by frequency-doubling (BBO) output of a Nd:YAG (Innolas GmbH, Spitlight 1200 or Spectra-Physics Quanta-Ray Lab Series) pumped dye laser (Radiant Dye, Narrowscan) using Coumarin 153, and it is operated at 10 Hz with typical pulse energies of about 1 - 2 mJ. To carry out VUV one photon ionization, frequency tripling of 355 nm (third harmonic output of a Nd:YAG laser) in a xenon gas filled cell could be employed to generate 118.2 nm ($h\nu$ = 10.6 eV) light. The output of this VUV light is estimated to be a few μJ and it exhibits great capability in many applications[84–86] especially for biomolecules with ionization potential lying around 10 eV.

REMPI spectroscopy

REMPI is a very effective approach to resonantly ionize molecules and study their electronic structures. In the research described in this thesis, the molecules of interest are resonantly ionized by only two photons (R2PI). In this technique, the ground state molecule is first excited to an intermediate electronically excited state by absorbing a photon of which the energy equals to the gap between ground and excited state. Subsequently, absorption of a second photon leads to ionization of the molecules. Depending on the source of the two photons, this technique could be distinguished between one colour R2PI (same source for excitation and ionization) or two colour R2PI (two sources for excitation and ionization, respectively). In most cases, one colour R2PI is efficient enough to ionize molecules with a UV chromophore. However, for molecule of which the ionization potential is more than two photon energies of the excitation laser, the two colour R2PI method could be employed. The first laser is normally fixed at the wavelength which matches the main transition, and the second laser is tuned to a frequency which maximizes the ionization efficiency. In practice, the two lasers should be overlapped both spatially as well as temporally in view of the limited lifetime of the electronically excited state, which makes it more complicated than the one color R2PI technique.

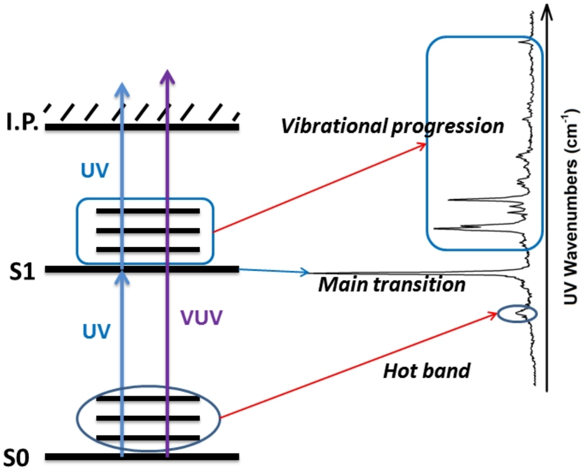

Figure 2.3: Schematic overview of R2PI spectroscopy and VUV one photon ionization.

As shown in Figure 2.3 , monitoring the ion yield as a function of excitation laser wavelength, an electronic excitation spectrum (REMPI spectrum) is acquired. In a typical REMPI spectrum, the main $S_1 \leftarrow S_0$ transition (transition from the electronic and vibrational ground state to vibrational ground state in electronic first excited state) gives the strongest peak. The spectrum also reveals a vibrational progression at higher energies (transitions from the electronic and vibrational ground state to electronic and vibrational excited states). This part of the spectrum contains information about vibrational levels in the excited state. On the red side of the main transition (origin), a hot band may appear due to the transition originating from a vibrational excited state in the electronic ground state, which indicates a incomplete cooling. If several conformers coexist for these conformers will display an unique $S_1 \leftarrow S_0$ transition. Thus,the absorption peaks in a REMPI spectrum may corresponds to different conformers. To maintain a high resolution and selectivity, it is very important to cool down the molecules before ionizing them. Poor resolution spectra due to hot temperature may result in difficulties in discriminating between vibrational structure in the first excited states and conformers.

Figure 2.3 shows that one photon of VUV light is capable of bringing the molecule above its ionization potential without an intermediate state. Although, it will lack conformation selectivity, it will offer a way to study molecules where UV REMPI can not be applied.

UV-UV ion-dip and hole-burning spectroscopy

Due to the complexity of the biomolecules, more than one stable conformation can exist. To identify different conformations from the complex excitation spectra, UV-UV ion-dip[47;87–89] and hole-burning[38;90;91] techniques can be employed. The concept of these two techniques is depicted in Figure 2.4.

In fact, these two techniques adopt the same principle which is based on electronic resonance depopulation of ground state, but differs only in the choice

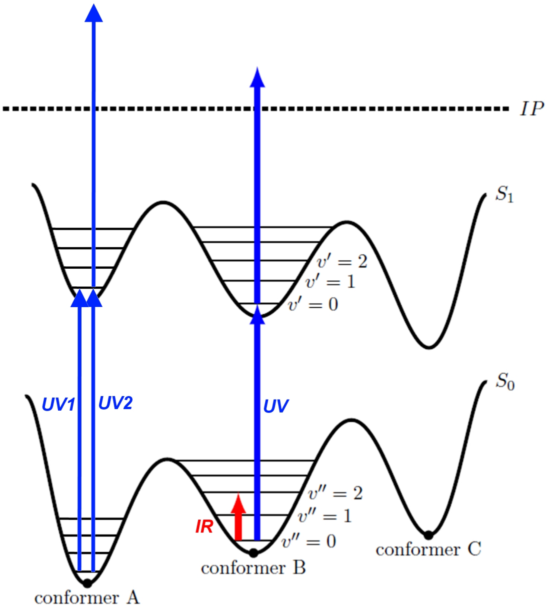

Figure 2.4: Schematic representation of conformation selective ion dip / hole burning spectroscopy. To distinguish different conformers, one of the two UV lasers is fixed at the $S_1 \leftarrow S_0$ transition of the selected conformer while the other one is tuned; to acquire conformation selective IR spectra, prior to the incident of UV probe laser, IR laser is scanned.

which laser (pump or probe) is scanned. For the UV-UV depletion technique, the probe laser (UV_2) is fixed at a wavelength corresponding to ground state excitation of a specific conformation, so a constant ion signal is produced. About 200 ns prior to the incident beam of the probe laser, pump laser (UV_1) irradiates the molecular beam at the same spatial position. If the pump laser could also excite the ground state of this selected conformation, then depopulation occurs for this state. As a result, there will be a dip in the ion signal created by the probe laser. By fixing the probe laser while scanning the pump laser, a UV-UV ion dip spectrum could be acquired. In this spectrum, all the wavelengths where ion dip is observed originate from the same conformation as the one selected by the probe laser.

In the UV-UV hole-burning technique, the pump laser is fixed while the probe laser is scanned. In this case, the conformation is selected by the pump laser which is used for ground state excitation and depopulation. During the scan of the probe laser, the main transition and relevant vibrational progression of the same conformation will be less intense when compared with original UV REMPI spectrum. Consequently, the peaks which belong to the same conformation can be distinguished immediately.

In both cases, it should be noted that a hot band is not affected since only the ground state is depopulated. The condition for both methods is that the pump laser must be sufficiently intense to obtain sufficient ground state depopulation. The time delay between the two lasers needs to be optimized to avoid two colour REMPI (too short a delay) or disappearance of the depopulation effect (too long a delay). Besides, to minimize signal fluctuation due to long-term UV power drifts and changing source conditions, alternating pump laser-off and pump laser-on signals could be measured by operating the pump laser at 5 Hz and the probe laser at 10 Hz.

IR-UV ion-dip and hole-burning spectroscopy

The goal of the present study is to elucidate their 3-dimensional structures and intramolecular interactions in small biomolecules. This is achieved by acquiring the IR absorption spectra and comparing these spectra with theoretically calculated spectra. IR-UV ion dip spectroscopy[92–95] is used to record the IR spectra. The principle is very similar to that of UV-UV ion dip method. First, the conformer of choice is selectively ionized by fixing the UV laser on its $S_1 \leftarrow S_0$ transition, resulting in a constant ion signal. About 300 ns prior to the probe laser, a YAG-pumped optical parametric oscillator (Laser Vision) produced IR light, which is spatially overlapped with the UV laser interacts with the molecular beam. Whenever the IR laser is resonant with a vibrational transition of the selected conformation, population is transferred from the ground state to a vibrational level and a dip in the ion signal is observed. By measuring the ion yield of the mass of interest as a function of the IR avelength, a mass-selected IR ion dip spectrum is obtained. Also, on/off measurements could be utilized here to minimize the influence by signal fluctuation.

Besides, IR-UV hole burning spectra are obtained by fixing the IR pump laser on a vibrational transition of the electronic ground state while scanning UV probe laser. Since the fixed IR pump laser depopulates a large amount of the specific conformer in ground state, the peaks in REMPI spectrum which belong to the same conformation will be much less intense or even will disappear during the UV probe scan. However, one must be aware that different conformers can absorb at the same IR wavelength. Therefore, one need to select the wavelength of the IR pump laser carefully in order to ensure conformer discrimination.

2.2 DFT computation: structure optimization and frequency calculation

After acquiring the IR spectra of studied biomolecules, the structure of a specific conformer is determined by comparing its spectrum to calculated spectra of several theoretically optimized structures. The first step is to perform a search to obtain low energy structures using the simulated annealing approach. Here, the temperature is raised to about 1300 Kelvin) so that all transition barriers in the potential energy surface are overcome and any conformational state is reachable. Then the system is cooled exponentially to low temperatures (e.g. 5 Kelvin) at which structures are recorded.

This simulation is based on molecular dynamics, in which Newton's equations of motion are solved to study molecular motion and conformational transitions. In molecular dynamics, atoms and bonds are treated as spheres and springs. The mathematics of spring deformation can be applied to describe the ability of bonds to stretch, bend and twist. However, the behaviour of different kinds of atoms and bonds are different in same molecule due to different atom diameters, bonds lengths and angles. A set of parameters is required to describe the structure. These parameters are included in a force field, which is an essential part in calculating the energy of a system. Over the past decades, many different kinds of force fields have been developed and applied to various molecular systems. The amber99sb[96] force field is selected in our simulation since it is suitable for biomolecules such as peptides, proteins, etc. To predict the energy associated with a given conformation of a molecule, a simple equation is given as follows[97]:

$$\begin{aligned} E_{total} &= \sum_{bonds} K_b \left(r - r_o\right)^2 + \sum_{angles} K_\theta \left(\theta - \theta_o\right)^2 \\ &+ \sum_{dihedrals} \frac{V_n}{2} \left[1 + cos(n\phi - \gamma)\right] + \sum_{i<j} \left[\frac{-A_{ij}}{r_{ij}^6} + \frac{B_{ij}}{r_{ij}^{12}} + \frac{q_i q_j}{\epsilon r_{ij}}\right] \end{aligned} \tag{2.1}$$

The first three terms describe the energy of bonded interactions (stretching, bending and torsion) and the fourth term stands for the energy of non-bonded interaction. Among numerous parameters, "K_b (K_θ)" controls the stiffness of a bond (angle) spring while "r_o (θ_o)" define its equilibrium length (angle). Unique parameters for bond stretching (angle bending) are assigned to each bonded doublet (triplet) of atoms based on their types (e.g. C-C, C-H, C-O-C, etc.). "V_n (barrier height associated with torsion), n (multiplicity, giving the number of minima as the torsion is rotated through 360°) and γ (phase factor indicating where the cosine function has its minimum)" parameters for torsional rotation are assigned to each bonded quartet of atoms such as H-N-C-O and the variable ϕ describe the relevant dihedral angle, i.e. angle between H-N bond and C-O bond in above mentioned system. The final term, non-bonded energy, represents the pair-wise sum of the energies of all possible interacting non-bonded atoms i and j. Therein, three sub-terms respectively accounts for repulsion, van der waals attraction and electrostatic interactions.

Knowing the total energy of a system, the force on an atom can be calculated from the change in energy between its current position and its position at a small distance away.

$$-\frac{dE}{dr_i} = F_i \tag{2.2}$$

Then the atomic acceleration is computed based on the following relationship

$$F_i = m_i a_i \tag{2.3}$$

Lastly, the common approach "leapfrog" method in which velocity and position information successively alternate at 1/2 time step intervals is used to predict the position of the atom at time "$t + \Delta t$ (time step of the simulation)".

$$v_i(t + \Delta t/2) = v_i(t - \Delta t/2) + a_i(t)\Delta t \tag{2.4}$$

$$r_i(t + \Delta t) = r_i(t) + v_i(t - \Delta t/2)\Delta t \tag{2.5}$$

The position at "$t + \Delta t$" is used to calculate the position at "$t + 2\Delta t$", and so on. Therefore the system can be propagated in time. After a suitable time, the optimized structure is stored for later evaluation and the molecular dynamics simulation is restarted to generate a next structure.

Using the molecular dynamics method, a large number of structures are found. However, the stability of these structures is mainly determined by the force field parameters, which makes them not necessarily the lowest energy conformers at high levels of theory. Therefore, geometries obtained from the conformational search have to be submitted to a full structural optimization using density functional theory (DFT) methods. For electronic wavefunctions related calculation, due to the rapidly growing cost and decreasing accuracy when number of electrons increases, its applications is greatly limited. Alternatively, DFT, which regards the properties of a many-electron system to be determined by the spatially dependent electron probability density, is used to study large system.

The relation between the energy of a multi-electron molecule E$_i$ and electron density ρ can be expressed using the so-called Kohn-Sham equations[98]:

$$\begin{aligned}\{-\frac{1}{2}\nabla^2 + v(r) + \int dr' \frac{\rho(r')}{|r-r'|} + \frac{\delta E_{xc}[\rho(r)]}{\delta\rho(r)}\}\psi_i(r) \\ = \{-\frac{1}{2}\nabla^2 + V_{ks}[\rho(r)]\}\psi_i(r) = E_i\psi_i(r)\end{aligned} \tag{2.6}$$

In which the kinetic energy (term -$\frac{1}{2}\nabla^2$) and the potential energy from the external field (term $v(r)$) are independent with electron density, while electron-electron Coulomb repulsion (term $\int dr' \frac{\rho(r')}{|r-r'|}$) and exchange-correlation potential ($\frac{\delta E_{xc}[\rho(r)]}{\delta\rho(r)}$) are affected. All the potential energy terms could be merged and expressed as Kohn-Sham potential $V_{ks}[\rho(r)$. By solving this equation with a self-consistent field method, the orbital together with its energy could be determined.

In practice, many functionals differing in their description of exchange- correlation energy exist, of which the very popular B3LYP[99] functional and dispersion interaction corrected B97-D[100] functional are used in our study. Besides, the Pople style basis sets 6-31G(d,p) and 6-311+G(d,p), which consist of a finite number of functions, are employed to describe molecular orbitals. For more explanation of relevant information, it can be found elsewhere[101].

Once the stable structure which corresponds to a local minimum of the PES is found, its harmonic frequency could be calculated from the second derivatives of the potential energy with respect to the displacement of nuclear coordinates. Scaling factors between 0.9 and 1 are normally used to correct for anharmonicity since the harmonic approximation is only valid at the position infinitesimal close to the local minima of PES. In addition, the IR intensities could also be computed by second derivatives of the dipole moment with respect to the normal coordinates.

2.3 Ion trap mass spectrometry

To explore ATP hydrolysis at the molecular level, an ion trap mass spectrometer is employed to study fragmentation behavior and the binding energy of ATP with ATPases' active site mimics. The experimental setup will be discussed in detail below. The theoretical methods employed to determine bond strengths and activation energies will be treated in Sec. 2.3.2 and 2.3.3.

2.3.1 Experimental set-up

The apparatus in which our experiments are performed is a commercial LCQ Classic quadrupole ion trap mass spectrometer (Thermo Finnigan) with electrospray ionization source. It consists of an electrospray ionization source, two focusing octapole ion guides and a quadrupole ion trap, in which an ion of interest can be selectively stored for collision-induced dissociation study.

Electrospray ionization With electrospray ionization (ESI), we can bring solution-phase molecules into the gas phase as ions. In constrast with other techniques, such as evaporation of the solvent by means of heating, or electron impact ionization, ESI prevents the ions from fragmenting when they are transferred to the gas phase. This method is therefore classified as a 'soft ionization' technique[102].

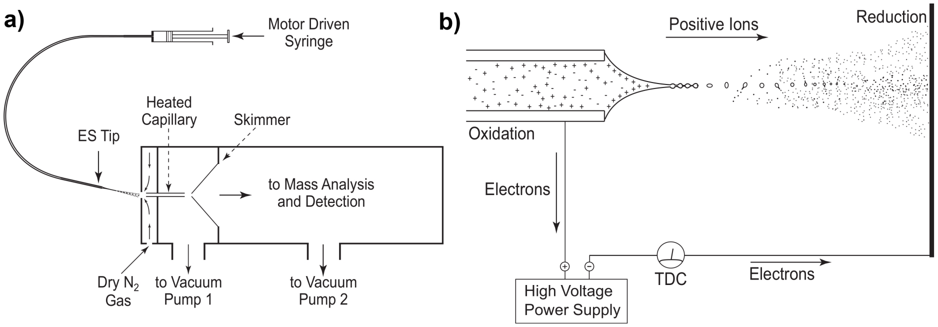

Figure 2.5: Overview of ESI. a) Electrospray ion source and interface to mass spectrometer. b) Major processes in atmospheric pressure region of ESI ion source run in positive mode. Taken from Kebarle and Verkerk[103].

The complexes of interest can be formed by dissolving the composing molecules in a 1:1 (v:v) mixture of water and methanol at a concentration of approximately 50 μmol/L for each component. These solutions are transferred to the ESI source using a motor-driven syringe, which injects the solution into the ESI source at a flow rate of 4 μL/min. There, the solution enters a capillary with its tip at high potential 3.79 kV, leading to a strong electric field. Due to this strong field, either positive or negative ions (depending on the voltages applied) will pile up at the tip of the capillary, form a cone-shaped meniscus, and emerge from the cone as a jet of charged droplets. The ions in these droplets spread over the droplet surface due to their mutual Coulombic repulsion. The droplets move through the air towards the opposing electrode while solvent is evaporated, aided by a weak nitrogen (N_2) flow, leading to increasing repulsion between the ions and, eventually, to a Coulomb explosion of the droplets into much tinier, highly charged droplets. After a few subsequent explosions, the 'droplets' that are left will only contain a single ion, and all solvent is evaporated, i.e. gas-phase ions are formed. The process of ESI is schematically displayed in Fig. 2.5.

Ion trap After ESI, the gas-phase ions of the complexes are transferred via a heated capillary and two focussing octapole ion guides into a quadrupole ion trap, where the ions of interest can be stored and experiments can be performed. A quadrupole ion trap consists of two endcap electrodes and a ring electrode (Fig. 2.6), together enclosing a volume in which a quadrupole electric field can be established by applying a radio frequency (RF) alternating voltage to the ring electrode while the endcap electrodes are grounded. When ions enter the trap via a small hole in one of the endcap electrodes, they will be trapped inside the trap only if the RF frequency is correct, which depends on the mass-to-charge ratio, m/z, of the ions. Therefore, by tuning the RF frequency resonant to a certain value of m/z, the corresponding ions can be trapped while the other ions are ejected from the trap. This allows us to store only the ions of interest in the trap. The exact mathematical and physical background of the quadrupole ion trap is complicated. March provides a comprehensive overview of the quadrupole mass spectrometer and the underlaying principles[104].

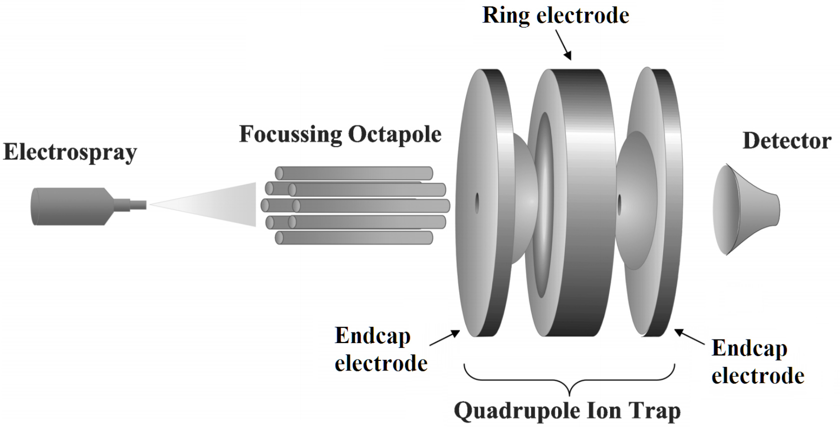

Figure 2.6: Overview of quadrupole ion trap. Adopted from O'Hair[105]. Details can be found in main text.

Collision-induced dissociation Once stored in the trap, the ions of interest can be fragmented by collision-induced dissociation (CID)[105]. The trapped ions will move along complex trajectories through the trap in the quadrupole field generated by the RF voltage on the ring electrode. CID can be stimulated by applying a RF pulse on the endcap electrodes to resonantly accelerate the ions to be fragmented. While being excited, these ions will undergo multiple collisions with neutral helium buffer gas present in the trap, leading to the conversion of their kinetic energy into internal energy. Eventually, one of the bonds of the ion will break, usually the weakest bond. Therefore, CID can be used to probe bond strengths by probing various fragmentation channels. The amount of collisional excitation can be tuned by varying the collision energy, or by varying the collisional activation time. However, due to the complexity of processes in ion traps[105;106], it is not straightforward to convert the experimental data into absolute binding energies. In the software of Finnigan ion traps, normalized collision energy (NCE)[107], which is given as a percentage of a standard excitation amplitude is used. Within this value the mass of the selected ion is taken into account and no further mass corrections are needed. For derivation of relative bond strength, there exist a more sophisticated methods which will be discussed in Sec. 2.3.2 and 2.3.3.

Mass spectrometry Ions can not only be stored in the trap based on their m/z values, but ions with certain m/z values can also be ejected selectively from the trap by adjusting the RF frequency[105]. By placing an electron multiplier detector behind the second endcap electrode, through which the ions will be ejected, ion intensities as a function of m/z can be measured, yielding a mass spectrum. Additionally, it is possible to perform multiple-stage mass spectrometry $(\text{MS})^n$. Here, after a first cycle of CID on trapped ions and subsequent selection of certain fragment ions, additional cycles of CID followed by selection of fragments can be implemented, allowing for the exploration of fragment ions using fragmentation experiments.

2.3.2 Breakdown diagrams

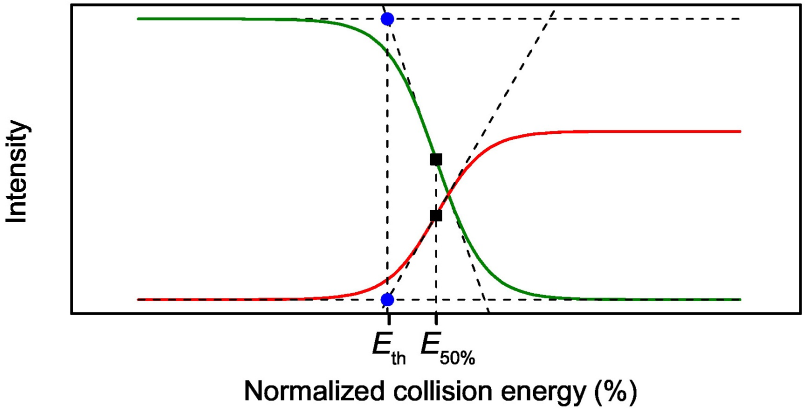

Figure 2.7: Typical breakdown diagram. Green and red lines represent parent and fragment ion intensity, respectively, as a function of normalized collision energy. $E_{50\%}$ is the collision energy for which half of the initial amount of parent is fragmented, or half of the final amount of fragment is formed. E_{th} is calculated as described in the text.

Bond strengths of complexes can be probed by measuring breakdown diagrams. The complexes of interest are fragmented by CID with 50 ms of collisional activation time, and the resulting parent and fragment ion intensities are recorded as a function of normalized collision energy (NCE). The resulting breakdown diagrams, i.e. plots of parent and fragment intensities versus NCE, show decreasing parent and increasing fragment intensities with increasing NCE, starting from a threshold NCE. A typical breakdown curve is presented in Fig. 2.7. This threshold NCE can be interpreted as the dissociation energy of the bond that breaks during the fragmentation process[108]. Zins et al. measured a series of benzylpyridinium ions, often exploited as ‘thermometer ions’ to evaluate internal energy distributions, and concluded that the threshold energies deduced from the breakdown curves correlate more or less linearly with zero-point corrected bond dissociation enthalpies at $0K$, calculated using density functional theory at the B3P86/6-31+G* level of theory. Although this correlation could well be molecule-specific, we assume that this linear relationship holds for our complexes as well, allowing us to compare threshold energies among different complexes.

Threshold energies can be deduced by fitting the breakdown curves with sigmoid functions of the form

$$I(E) = \frac{I_0}{1 + \exp\left[-k(E - E_{50\%})\right]} \tag{2.7}$$

where I is the intensity, E the normalized collision energy, and I_0, $E_{50\%}$ and k are the fitting parameters optimized using a least-squares criterion. In order to minimize the signal fluctuation due to long term operation of instrument, normalized ions' intensities are employed in fitting curves. Here, I_0 represents the initial amount of parent ion or the final amount of fragment ion, $E_{50\%}$ is the normalized collision energy for which 50% of the parent ion is fragmented or the fragment ion is formed, and k is a measure of the slope of the breakdown curve. More precisely, $kI_0/4$ equals the slope of the breakdown curve at $E = E_{50\%}$. Threshold energies E_{th} are given by the intersection of the tangent line to the breakdown curve at $E = E_{50\%}$ with the line $I = I_0$ for parent ions or $I = 0$ for fragments, i.e.

$$E_{\mathrm{th}} = E_{50\%} - \frac{2}{|k|}, \tag{2.8}$$

as derived as follows:

- $E \to -\infty$, collisions and therefore fragmentation are not possible, we obtain the initial amount of parent ion. The limit $E \to \infty$, all parent ions have been fragmented, we obtain the final amount of fragment ion. Since parent breakdown diagrams have negative k whereas fragment curves have positive k, we obtain

$$\lim_{E\to-\infty} I_{\mathrm{parent}}(E) = \lim_{E\to-\infty}\left(\frac{I_0}{1 + \exp\left[-k_{\mathrm{parent}}(E - E_{50\%})\right]}\right) = \frac{I_0}{1+0} = I_0 \tag{2.9}$$

$$\lim_{E\to\infty} I_{\mathrm{fragment}}(E) = \lim_{E\to\infty}\left(\frac{I_0}{1 + \exp\left[-k_{\mathrm{fragment}}(E - E_{50\%})\right]}\right) = \frac{I_0}{1+0} = I_0. \tag{2.10}$$

Thus, I_0 represents the initial amount of parent ion or the final amount of fragment ion.

- When 50% of parent is fragmented or 50% of fragment is formed, the measured intensity will be $I_0/2$. In that case, $\exp\left[-k(E - E_{50\%})\right]$ must equal 1, which implies that $E = E_{50\%}$, as anticipated.

- The slope of the breakdown curve is given by the derivative of I with respect to E,

  $$\frac{\mathrm{d}I(E)}{\mathrm{d}E} = \frac{kI_0 \exp\left[-k(E - E_{50\%})\right]}{\left(1 + \exp\left[-k(E - E_{50\%})\right]\right)^2}. \tag{2.11}$$

  Evaluated at $E = E_{50\%}$, this equation yields

  $$\left[\frac{\mathrm{d}I(E)}{\mathrm{d}E}\right]_{E=E_{50\%}} = \frac{kI_0}{4}. \tag{2.12}$$

  This shows that indeed the slope of the breakdown curve at $E = E_{50\%}$ equals $kI_0/4$.

.

2.3.3 Energy-Dependent Kinetic method

Complexes may exhibit multiple fragmentation channels by breaking different bonds. Relative activation energies of multiple fragmentation channels within one complex can be determined by the energy-dependent kinetic method[109].

Central to this method are measurements of the rates k_j for the formation of fragment j. Rates of fragment formation can be determined by measuring parent and fragment intensities as a function of collisional activation time. We assume that all fragmentation processes follow simple first-order kinetics, where the parent intensity I_{parent} is given as a function of activation time t by

$$I_{\text{parent}}(t) = I_0 \exp\left(-k_{\text{parent}} t\right) \tag{2.13}$$

where I_0 is the parent intensity without collisional activation. The fragment intensities I_j are given by

$$I_j(t) = \frac{k_j}{k_{\text{parent}}} \left[I_0 - I_{\text{parent}}(t)\right]. \tag{2.14}$$

From Equations 2.13 and 2.14, we can derive that plots of $-\ln\left[I_{\text{parent}}(t)/I_0\right]$ and $I_j(t) \ln\left[I_{\text{parent}}(t)/I_0\right] / \left[I_{\text{parent}}(t) - I_0\right]$ versus t should yield straight lines with slopes equal to k_{parent} and k_j, respectively.

We assume that the rates k_j obey Arrhenius' law,

$$k_j = A_j \exp\left(-\frac{E_{\text{act},j}}{RT_{\text{eff}}}\right), \tag{2.15}$$

Or the natural logarithm of Equation 2.15,

$$\ln k_j = \ln A_j - \frac{E_{\mathrm{act},j}}{RT_{\mathrm{eff}}}, \tag{2.16}$$

where $E_{\mathrm{act},j}$ is the activation energy of fragmentation process j, the pre-exponential constant A_j accounts for the entropy of activation of this process, and T_{eff} is the effective temperature of the parent ion. The activation energy $E_{\mathrm{act},1}$ of a single fragmentation process (process 1) could be determined by measuring its rate k_1 as a function of effective parent temperature. A plot of $\ln k_1$ versus $1/RT_{\mathrm{eff}}$ would yield a straight line with its slope equal to $-E_{\mathrm{act},1}$. Although we know that the effective parent temperature increases with increasing NCE, we cannot control T_{eff} directly.

Nevertheless, we can use a second fragmentation process (process 2), for which Equations 2.15 and 2.16 also hold, as a reference to eliminate the factor $1/RT_{\mathrm{eff}}$ from Equation 2.16:

$$\ln k_1 = \ln A_1 - \frac{E_{\mathrm{act},1}}{E_{\mathrm{act},2}} \ln A_2 + \frac{E_{\mathrm{act},1}}{E_{\mathrm{act},2}} \ln k_2. \tag{2.17}$$

We can vary the values of k_1 and k_2 by measuring ion intensities as a function of activation time for varying NCE. According to Equation 2.17, a plot of $\ln k_1$ versus $\ln k_2$ will yield a straight line with slope $E_{\mathrm{act},1}/E_{\mathrm{act},2}$, i.e. the activation energy of fragmentation process 1 relative to the activation energy of process 2. Thus, this method allows us to measure *relative* activation energies for competing fragmentation channels within a single complex.

3 A new high intensity and short-pulse molecular beam valve

Abstract

In this chapter, we report on the design and performance of a new home-built pulsed gas valve, which we refer to as the Nijmegen Pulsed Valve (NPV). The main output characteristics include a short pulse width (as short as 20 μs) combined with operating rates up to 30 Hz. The operation principle of the NPV is based on the Lorentz force created by a pulsed current passing through an aluminum strip located within a magnetic field, which opens the nozzle periodically. The amplitude of displacement of the opening mechanism is sufficient to allow the use of nozzles with up to 1.0 mm diameter. To investigate the performance of the valve, several characterizations were performed with different experimental methods. First, a fast ionization gauge was used to measure the beam intensity of the free jet emanating from the NPV. We compare free jets from the NPV with those from several other pulsed valves in current use in our laboratory. Results showed that a high intensity and short pulselength beam could be generated by the new valve. Second, the NPV was tested in combination with a skimmer, where resonance enhanced multiphoton ionization combined with velocity map imaging was used to show that the NPV was able to produce a pulsed molecular beam with short pulse duration (~20μs using 0.1% NO/He at 6 bars) and low rotational temperature (~1 K using 0.5% NO/Ar at 6 bars). Third, a novel two-point pump-probe method was employed which we label double delay scan. This method allows a full kinematic characterization of the molecular beam, including accurate speed ratios at different temporal positions. It was found that the speed ratio was maximum (S = 50 using 0.1% NO/He at 3 bars) at the peak position of the molecular beam and decreased when it was on the leading or falling edge.

3.1 Introduction

During the past several decades, the generation of atomic and molecular beams has attracted much attention because of their importance in many fields of research.[110;111] Pulsed beam sources can create a short gas pulse with improved beam characteristics compared to continuous types, including a higher beam density, colder internal rotational state distributions, and a more narrow velocity distribution.[110;111] In addition, due to the very short pulse duration, the pumping requirement of the experimental apparatus is greatly reduced and the production of the molecules can also be synchronized with pulsed laser detection methods. As a result of above mentioned advantages, a large amount of effort has been made to develop and improve pulsed beam sources.

A wide variety of pulsed valve designs have been reported in the past.[112;113]In 1978, Gentry and Giese[114] developed a pulsed valve (precursor to the present-day Jordan valve) based on the principle of magnetic repulsion between two metal strips through which a large opposing current was pulsed. This design produces gas pulses with a full width at half maximum (FWHM) down to about 10 μs when expanding pure helium gas at high pressure (25 bars). Later on, from the 1980s, pulsed valves based on the rapid deformation of piezoelectric crystals were developed and improved by several groups.[115–118]These valves typically apply a short high voltage (HV) pulse to a disc-shaped piezoelectric crystal, producing gas pulses with ~100-150 μs pulse widths. Solenoid valves such as the robust, commercially available General Valve Series 9 with its magnetically activated plunger are also widely used in the field of atomic and molecular beams. These types produce pulses with a typical width of a few hundreds of microseconds.[119] Around anno 2000, an optimized magnetically activated plunger pulsed valve operated at high pressure was developed by Even and co-workers,[120;121] referred to as the Even-Lavie valve. It has been shown that their valve is able to produce beams with a pulse duration down to about 10 μs and speed ratio S = $v/\Delta v$ up to S $\approx$ 100 in helium. Recently, a pulsed valve based on a cantilever piezo was reported by Janssen and co-workers,[122;123] based on an original design by Gerlich (Chemnitz). This valve could be operated in a continuous mode or a pulsed mode (up to 5 kHz repetition rate) and is reported to produce short and rotationally cold pulsed molecular beams with a speed ratio up to 135 at the central coldest part of a short gas pulse. In this chapter, we present a new pulsed valve design based on the Lorentz force on a current in a magnetic field. This design, which is extremely simple and inexpensive to build, shows the desired characteristics of a short, intense, and cold molecular beam. Our design is related to a pulsed valve reported in 1986 by Barry et al.[124] also using the Lorentz force but with a different mechanism for closing the valve. The use of modern materials and the design of the closing mechanism make the Nijmegen Pulsed Valve (NPV) much more compact, robust, and inexpensive compared to older designs, as discussed later in this chapter.

The principle of the NPV is shown schematically in Fig. 3.1. Basically, a large

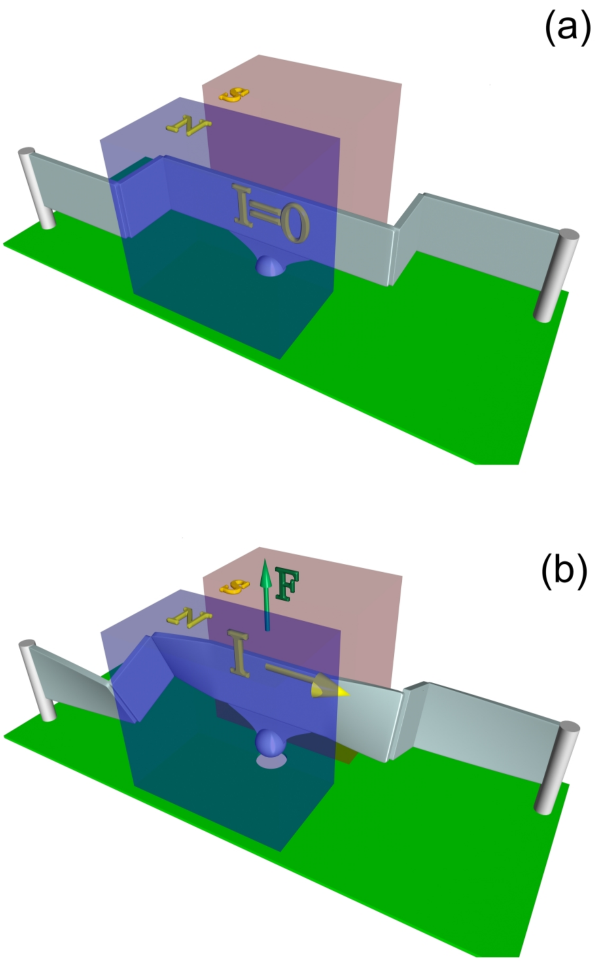

Figure 3.1: Schematic view of principle of the Nijmegen Pulsed Valve: (a) no current passing through the aluminum, valve is closed. (b) Lorentz force lifts the strip up, opening the valve. The distortion of the aluminum strip due to the Lorentz force is exaggerated for clarity.

(400-1000 A) short-pulsed (30-50 μs) current $\boldsymbol{I}$ passes through an aluminum strip bent in a **Z**-shape ($l = 6$ mm interaction length perpendicular to magnetic field), which is located in a magnetic field $\boldsymbol{B}$ (~1.45 **T**) created by permanent magnets (Quadermagnet $5 \times 5 \times 3$ mm N52 Nickel coated on NdFeB, from magnets4you, GmbH). Attached to the middle of the aluminum strip is a pin with a small spherical tip. The ends of the aluminum strip are fixed to two electrodes, used to supply the current pulse, with enough tension to force the tip to close off an O-ring centered on the nozzle hole. The shape of the strip is such that the closing force (vertical) is high, but the sideways movements are still possible. This enables the tip to find the O-ring center automatically. When the current passes through the strip, the Lorentz force $\boldsymbol{F} = (\boldsymbol{I} \times \boldsymbol{B}) \cdot l$ ($\boldsymbol{F} \sim 7$ N when $\boldsymbol{I} = 1$ kA) forces the aluminum strip upwards, opening the nozzle hole for a short time, until the current pulse ends. The tension force in the strip causes the valve to close again at the end of the current pulse. As in any design for rapid motion, the mass of the moving part must be kept as low as possible, in our case the mass of the metal strip together with spherical tip is 23 mg. Furthermore, a large instantaneous current $\boldsymbol{I}$ is created by short-circuiting a large capacitance via field effect transistors, and a large magnetic field $\boldsymbol{B}$ is formed by placing the strong field magnets close to the strip.

In this chapter, we report our first results on the characterization of this valve. In Sec. 3.2, we describe the details of the NPV design and its operation principle, and give an overview of the experimental apparatus and measurement techniques. In Sec. 3.3, we present and discuss our first results using the NPV. The conclusions are summarized in Sec. 3.4.

3.2 Valve design and characterization methods

3.2.1 Design of the NPV

A nearly to-scale drawing of the valve construction is shown in Fig. 3.2 , where the diameter of the valve base plate is 30 mm. During assembly the strip is mounted on the two electrodes and the closing tension is adjusted while detecting leakage with a He leak detector. A yoke containing the two permanent magnets is then installed. A low voltage (10-15 V) short pulse (30-50 μs, 10 Hz) is applied between the electrodes, moving the strip up by the Lorentz force, which opens the nozzle of the valve. For a good operation with enough strip deformation to fully open the valve, it is important that the strip is a very light, strong, and flexible conductor. The lighter the strip, the faster it will react, resulting in the shortest molecular pulse. Aluminum alloy (1-3 % silicon in aluminum) was selected as the material for making the strip.

For the geometry of the nozzle, Even and co-workers[121;125] have shown that a conical nozzle produces downstream beam densities which are higher by an order of magnitude than the densities produced by a simple pinhole (sonic) nozzle. A conical shape of about 40° appears to be a good compromise between maximum forward centerline beam intensity and efficient translational cooling. For the NPV, a conical shape nozzle with 50° full opening angle and 500 μm opening diameter was employed to produce a high density pulsed beam.

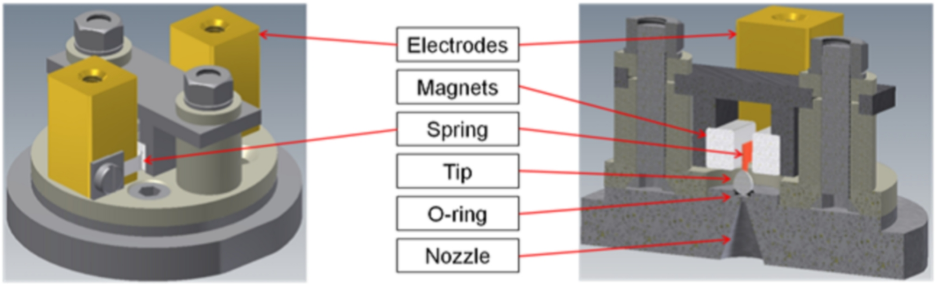

Figure 3.2: Schematic view of the actual construction of the Nijmegen Pulsed Valve. The left picture shows an overview and the right picture displays a cross section view of the valve.

3.2.2 Electronics

In Fig. 3.3 , a block diagram of the electronics which delivers the drive pulse to the NPV is shown. The NPV (not shown in the figure) is connected at the right hand side of the diagram. A capacitor C1 (10000 μF) is charged by a floating power supply, which is adjustable between 0 and 20 V. Ten 1000 μF capacitors with low series resistance (16 mΩ per capacitor) were connected in parallel; this allows for a current of up to 1 kA.

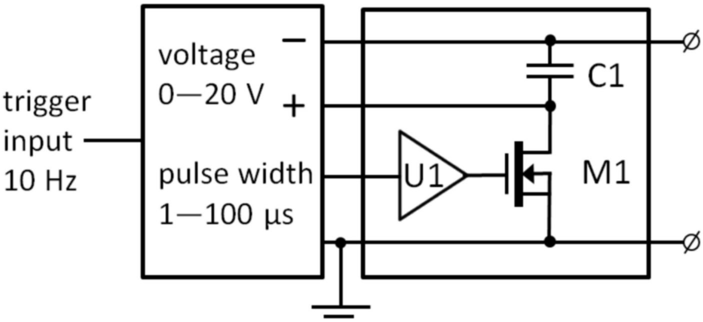

Figure 3.3: Block diagram of the electronics used to drive the NPV.

A transistor-transistor logic (TTL) pulse is delivered to the buffer amplifier U1 to drive the MOSFET M1 at 15 V. U1 and M1 are connected at short distance, because M1 has a high input impedance. We used four MOSFETs parallel (IRLU9743), with a low drain-source resistance ($R_{DS(ON)}$ = 3.1 mΩ) and high peak current (640 A per FET).

When the drive pulse is delivered to M1, C1 is directly connected to the NPV and is partially discharged. At the end of the drive pulse, the connection is opened again and the current is stopped. The rise and fall times of the drive pulse will be fast because of the low inductance in the current path.

We observe that the NPV physical opening time is a combination of the driving voltage and pulse width. This opening time becomes longer with higher voltages and/or longer pulse widths. Using higher backing pressures the voltage needed to open the valve becomes larger, indicating that more power is needed to overcome the blocking force exerted by the gas on the closing tip.

In the design of Gentry and Giese,[80] the two repelling metal strips needed high voltages and currents (kV and kA). In contrast, the NPV uses low voltages, which makes it safe to touch the NPV electrodes during operation. Due to the low heat dissipation (1-2 W), the valve body stays cool during operation, which is important for low beam temperatures. The thyristors used in the Barry et al.[124] design also required a high working voltage than the modern transistors used in the NPV.

3.2.3 Experimental setup and methods

A single chamber setup (see Fig. 3.4a) with fast ionization gauge (FIG, see Fig. 3.4b) was used to measure beam densities and pulse lengths of NPV and some other pulsed valves currently used in our lab. In addition, other experiments were performed in a new home-built velocity map imaging (VMI) apparatus (see Fig. 3.5).

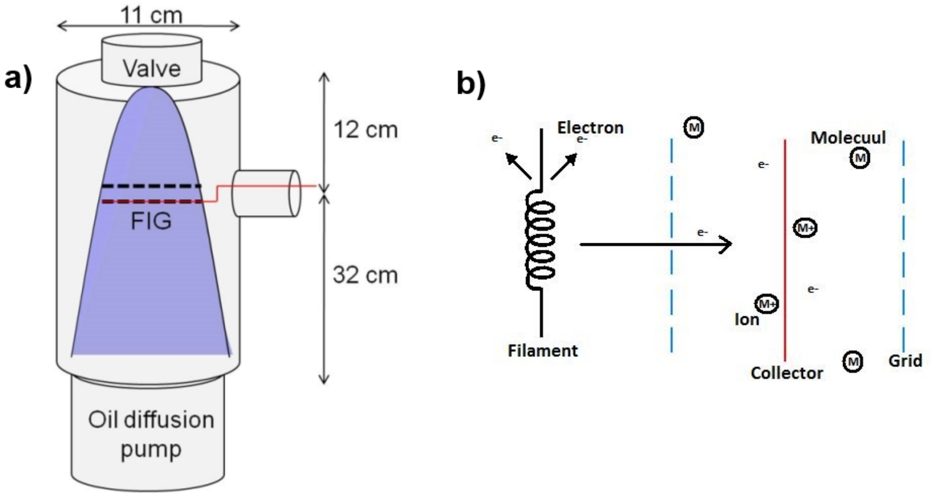

Figure 3.4: Schematic diagram of a) the valve testing apparatus and b) the operation of fast ionization gauge.

In the single chamber setup, a FIG was mounted 12 cm downstream from the valve to monitor the molecules in the pulsed beam. An oil diffusion pump with 500 L s^{-1}) pumping speed was used to maintain the chamber pressure below 10^{-6} mbar background pressure (monitored by a Varian pressure gauge). The FIG consists of three electrodes/parts, namely the filament, the grid and the collector. The filament is used for the production of electrons. Due to the positive charge on the grid, the electrons were attracted away from the filament and circulate around the grid. When the pulsed molecular beam drifts close to the FIG, the molecules will be ionized by the electrons around the grid and the positive ions are detected by the collector which connects to an oscilloscope. As a result, the pulsed molecular beam density and width could be derived from the oscilloscope recorded signal. Detailed method will be discussed in sec. 3.3.1

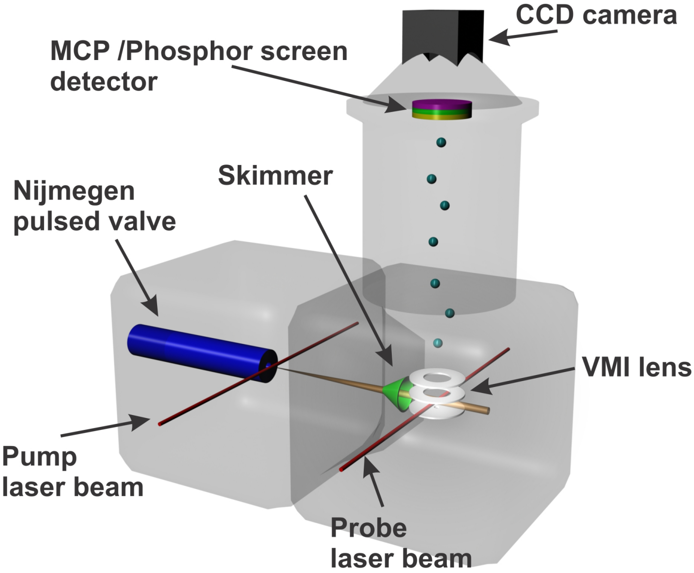

Figure 3.5: Schematic view of the VMI setup using two lasers crossing the molecular beam at two points A and B. The double resonantly ionized NO^+ ions are detected by VMI

The basic details of the new built VMI apparatus are almost the same as the conventional VMI setup as described by Eppink and Parker.[126] However, the propagation direction of the molecular beam is perpendicular to the time-of-flight (TOF) axis in our setup and the setup is based on two small cubic chambers with a length of only 12.2 cm, which is very similar in concept to that of Chandler et al.[127] The NPV with flange is mounted in the first chamber and aligned with the help of a telescope. Additional experimental details will be discussed in sections where the relevant results are described.

In order to characterize the performance of the NPV, several aspects were investigated. First of all, the density of the NPV produced jet was measured by a FIG and compared with that of two other pulsed valve designs. Second, the beam pulse duration could also be determined using pulsed laser ionization by detecting the ion intensity when scanning the time delay between the drive pulse of NPV and the crossing time of the nanosecond laser pulse with the gas pulse. Third, by taking a resonance enhanced multiphoton ionization (REMPI) spectrum of the molecular beam, internal rotational temperatures (T_{rot}) of the NO molecules could be determined. Fourth, a novel two-point pump-probe scheme (Fig. 3.5) was used, which we label *double delay scan* (DDS). This method allows for a full kinematic characterization of the molecular beam by measuring the speed distributions at different positions of the molecular beam pulse. In this scheme, the pump laser excited molecules to a long-lived rovibrational state that is not populated in the original molecular beam. The probe laser subsequently state-specifically ionizes these molecules in the detection area, which is located 11 cm further downstream. By scanning the time delay between the drive pulse of the NPV and the pump laser beam, different positions of the molecular beam pulse packet could be selected; after the selection, by detecting the NO^+ when scanning the time delay between pump laser and probe laser, we obtain the speed distribution of this position since the travelling distance of the investigated position (i.e., the distance between the crossing points of the pump and probe laser with the gas pulse) is accurately known. In addition, the overall speed distribution of the entire molecular beam could be determined by integrating speed distributions of different beam positions.

3.3 Results and discussion

3.3.1 Beam density

Previously reported beam densities for pulsed molecular beams are in the range of 10^{13}-10^{14} particles / cm^3.[110;123;128;129]We measure beam densities using a FIG in a single chamber setup, and after a skimmer in the differentially pumped two-chamber setup.

In the two-chamber setup, the distance between nozzle and skimmer is about 80 mm and the skimmer has a diameter of 1 mm. We discuss here the results for the NPV operating at 10 Hz and 3 bars pressure of 0.1% NO/He behind the nozzle. The pressure in the source and detection chamber typically increases by about 2.6 $\times 10^{-5}$ mbar and 1.1 $\times 10^{-6}$ mbar, respectively. We note that these values are for normal operation; the intensity can be increased ~tenfold by lengthening the opening time of the valve. However, at these conditions the skimmer started to show choking effects (lower S, higher T_{rot} , and a long tail), therefore, we worked with the shorter opening time conditions.

Although calibrating the density of a molecular beam pulse is notoriously difficult and prone to error, we estimate the beam density simply from the pressure rise. Since the turbo molecular pump has a pumping speed of 65 L s^{-1} for helium, the detection chamber has a load of 7.2 $\times 10^{-8}$ bars L s^{-1}. Because the repetition rate of the valve was 10 Hz, a single gas pulse creates a load of 7.2 $\times 10^{-9}$ bars L, which is equivalent to 3.2 $\times 10^{-10}$ mol or $N_0 = 1.9 \times 10^{14}$ particles per pulse in the detection chamber. The gas pulse is assumed to be a Gaussian function with a temporal shape $f(t) = N_0 \frac{1}{\sigma\sqrt{2\pi}} \exp(-t^2/2\sigma^2)$, with FWHM $\approx 20\mu s = 2.355\sigma$. Using the nozzle and skimmer geometry, the centerline beam has solid angle of $\Omega = 1.2 \times 10^{-4}$ sr entering the detection chamber. Therefore, the beam brightness is $B = \frac{N_0}{\sigma\sqrt{2\pi}\Omega} = 7.4 \times 10^{22}$ particles s^{-1} sr^{-1}. The beam intensity at the crossing point with the laser d = 12 cm downstream of the nozzle is $I = \frac{B}{d^2 v} = \frac{7.4 \times 10^{22} particles \cdot s^{-1} \cdot sr^{-1}}{12^2 cm^2 sr^{-1} \cdot 1.85 \times 10^5 cm \cdot s^{-1}} = 2.8 \times 10^{15}$ particles cm^{-3}, which by this rough estimate is higher than the previously reported values. For argon carrier gas (pumping speed: 69 L s^{-1}), the same calculation method results in a beam intensity of about 1.2 $\times 10^{15}$ particles cm^{-3}.

Table 3.1: Results of the FIG measurements comparing the NPV with two other pulsed valves (standard operation, not specifically optimized for short pulse duration) in pure helium. The uncertainty in all values is 20% or higher.

Backing pressure	1 bar		3 bars	
Properties	Peak particle number	FWHM (μs)	Peak particle number	FWHM (μs)
NPV	9 $\times 10^{13}$	50	9 $\times 10^{13}$	40
PV1	2 $\times 10^{13}$	160	3 $\times 10^{13}$	150
PV2	1 $\times 10^{13}$	500	2 $\times 10^{13}$	450
Backing pressure	6 bars		10 bars	
Properties	Peak particle number	FWHM (μs)	Peak particle number	FWHM (μs)
NPV	5 $\times 10^{13}$	27	5 $\times 10^{13}$	24
PV1	2 $\times 10^{13}$	70	2 $\times 10^{13}$	50
PV2	2 $\times 10^{13}$	400	2 $\times 10^{13}$	330

The single chamber setup measured results for the NPV are shown in Table 3.1 along with those for two other pulsed valve designs in current use in our laboratory (PV1: Jordan valve; PV2: General valve). For all three pulsed valves, results were obtained using pure helium gas at several different backing pressures. The emission current applied on the filament of the FIG was kept constant at 0.8 mA and the grid voltage at 200 V. The resulting signal at the FIG collector was fed to an oscilloscope to view the temporal profile of the beam intensity. From these traces, the peak value and FWHM reflect the beam density and pulse length of the investigated pulsed valve. The total area under each trace corresponds to the number of particles per pulse (N_0), and the peak intensity (particle number) can be derived in a straightforward manner, which is similar to the calculation process in previous paragraph.

As the backing pressure increases the opening time/voltage setting of the NPV has to be adjusted to give more driving power to overcome the blocking force. The driving pulse was optimized to give the shortest pulse length under "normal" intensity conditions. The consequence of this necessity, also found for the other valves, is that for each valve the density information as a function of backing pressure in Table 3.1 is quite qualitative. From Table 3.1 , we conclude that all three pulsed valves have their best performance at higher backing pressure. In this simple comparison, the NPV beam density and pulse length were better than those of the other two pulsed valves currently used in our lab. Hence, the new NPV is able to generate a short pulse and high density molecular beam.

3.3.2 Beam pulse duration and temperature: Single laser scan

In order to study the pulse duration and rotational temperature of a skimmed molecular beam, we performed delay scans and wavelength scans using a single laser in the setup shown in Fig. 3.5 . The results can be compared to the FIG data from Sec. 3.3.1. Here, we show some representative results of the measured gas pulse duration: ion intensity as a function of the time delay between the drive pulsed voltage of NPV and the crossing time of the nanosecond laser pulse with the gas pulse of a seeded beam of 0.1% NO in helium or 0.5% NO in argon (the difference in concentration is due to a compromise between carrier gas cooling effect and signal intensity, which can decrease with increasing NO concentration especially in Ar carrier gas due to formation of clusters). The gas pulse was measured in two differentially pumped (VARIAN Turbo-V81-M) vacuum chambers consisting of the NPV and skimmer in the source chamber, and a VMI lens with microchannel-plate (MCP)/phosphor screen in the detection chamber. In this measurement, the valve nozzle diameter was 500 μm and a 1 mm skimmer was mounted 8 cm from the nozzle exit to allow for differential pumping of the two chambers. The backing pressure behind the nozzle was 6 bars. The pulsed gas beam was crossed 12 cm downstream from the nozzle exit by a tunable nanosecond dye laser frequency doubled to ~226 nm in order to state-selectively ionize NO ($^2\Pi_{1/2}$, J = 1/2). The NO^+ parent ions were accelerated by the ion lens assembly to the detector and the total ion yield was measured by detecting the light of the phosphor screen with a CCD camera. The pressure in this detection chamber was 1 $\times 10^{-7}$ mbar when the molecular beam was off and increased to about 2 $\times 10^{-6}$ mbar for 0.1% NO in helium or 3 $\times 10^{-7}$ mbar for 0.5% NO in argon when the valve was pulsed at 10 Hz. The difference in pressure increase still leads to comparable beam intensities, as the calculations showed in Sec. 3.3.1:2.8 $\times 10^{15}$ particles cm^{-3} and 1.2 $\times 10^{15}$ particles cm^{-3} for 0.1% NO/He and 0.5% NO/Ar, respectively.

In Fig. 3.6 , the time-of-flight profile is presented that is recorded when using the two different seeded beams. The bottom curve displays the intensity of NO^+

ions produced by REMPI of the 0.1% NO/He beam, and detected by gating the MCP gain voltage with a negative HV pulse at a time corresponding to the TOF of the mass of NO^+. The time delay was scanned in small steps of 3 μs. As can be seen in the lower curve of Fig. 3.6 , the NPV produces a short gas pulse with FWHM down to about 20 μs. In the top trace of Fig. 3.6 , we present a time delay trace measured for a beam of 0.5% NO/Ar with 5 μs scanning steps. A typical pulse of FWHM = 25 μs is measured. We note that the FIG data showed slightly larger values for the FWHM, although both measurements have been taken at 12 cm downstream. We attribute this difference to detecting only the lowest rotational state, and to secondary collisions, which added a small contribution to the falling edge of the FIG data on top of the direct beam signal.

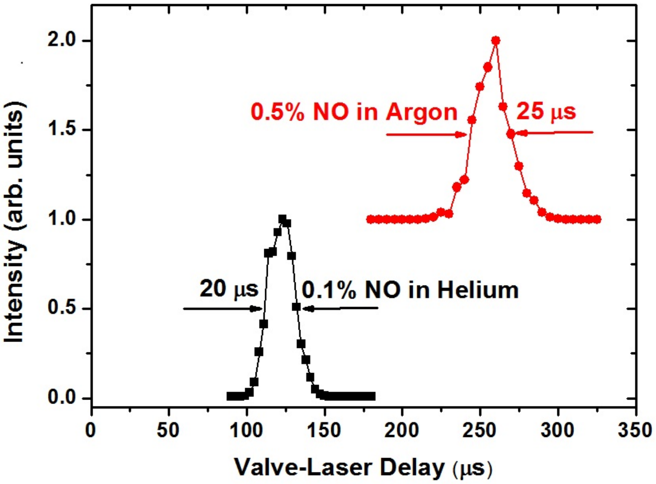

Figure 3.6: Total NO^+ ion yield, as measured by the CCD camera of the light from the phosphor screen behind the MCP detector, of two different skimmed beams of 0.1% NO in helium and 0.5% NO in argon at 6 bar backing pressure. The intensities of NO (J = 1/2) are presented. The distance between nozzle and laser ionization region was 12 cm. Pulsed beams with FWHM duration as short as 20 μs can be made with the NPV. Each curve was normalized individually and the top curve (0.5% NO in argon) was shifted vertically by one unit for clarity.

To investigate the internal rotational temperature of the NO molecule, a (1+1) REMPI spectrum was also taken around 226 nm. The acquired spectrum shows that rotationally cold seeded beams can be produced by NPV (see Fig. 3.7). Since the rotational constants of NO are well known in its ground and excited state, the simulation program (PGOPHER)[130] could be utilized to simulate the REMPI spectrum between 44180 cm^{-1} and 44230 cm^{-1}. Comparing the experimental result to the simulation, a molecular beam with 6 K rotational temperature could be produced for 0.1% NO/He, while a lower rotational temperature (1.5 K) could be produced for 0.5% NO/Ar. The rotational temperature was almost constant across the beam profile, thus, the same in the leading edge and falling edge as at the central part. While Ar is known to be most efficient in rotational cooling, He, presumably due to less heating by cluster formation, yields a higher speed ratio than Ar.

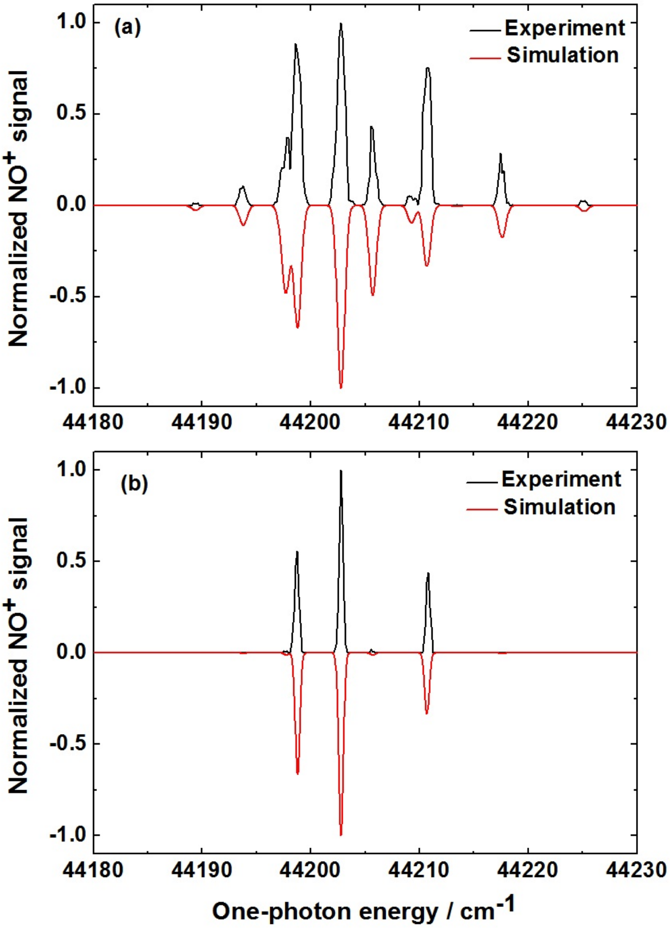

Figure 3.7: REMPI spectrum acquired for NPV molecular beam using (a) 0.1% NO/He, (b) 0.5% NO/Ar, and comparison with simulation.

3.3.3 Speed ratio: Double delay scans

Pulsed valve gas pulses can be inhomogeneously broadened because the nozzle pressure and density are changing during the short duration of the gas pulse, resulting in a variation in the speed ratio over the length of the gas pulse. The speed ratio of the Amsterdam cantilever valve, for example, was reported[123] to reduce by about 41% of the maximum value at temporal positions halfway in the rising edge or falling edge of the short duration pulse. Therefore, direct measurement of speed distributions at different temporal positions of the beam pulse packet is needed for a full kinematic characterization.

In this work, we designed a pump-probe scheme (labeled *double delay scan*) to accomplish this time dependent velocity distribution measurement using pre-excitation of the beam near the nozzle exit by a focused nanosecond laser pulse. In this way, a very small (20 μm diameter) package of tagged molecules was created for later detection. The NPV was operated at 10 Hz and 3 bars backing pressure of two gas mixtures: 0.1% NO in He and 0.5% NO in Ar. Around 2 mm after the nozzle exit (position "A"), a pump laser beam state selectively excited the seeded molecule NO from its ground state $X^2\Pi_{1/2}(\text{v} = 0, \text{J} = 1.5)$ to the $A^2\Sigma^+(\text{v} = 0, \text{J} = 1.5)$ excited state. The excited $A^2\Sigma^+(\text{v} = 0)$ state has a fluorescence lifetime of around 100 ns and a proportion of the excited NO will decay to $X^2\Pi_{1/2}(\text{v} = 1, \text{J} = 1.5)$. In fact, because of poor Franck-Condon overlap a whole series of vibrational states will become populated via non-diagonal transitions to the ground state. At d =110 mm downstream from the interaction position between pump laser pulse and molecular beam, a probe laser beam crosses with the molecular beam (position "B") and state selectively ionizes the $X^2\Pi_{1/2}(\text{v} = 1, \text{J} = 1.5)$ state of NO. The ionized NO^+ is extracted by the VMI lens and detected by a MCP/phosphor-screen detector. By scanning the time delay between the drive pulse of NPV and pump laser (t_A), different positions of the molecular beam pulse packet are selected for the speed ratio distribution measurement. By subsequently scanning the time delay between pump laser pulse and probe laser pulse (Δt), the speed distribution for a particular initial position on the molecular beam pulse packet is acquired. These measurements thus require scanning two delays for the full kinematic characterization of the molecular beam, hence, the denotation "double delay scan". In practice, the pump laser timing was fixed and the drive pulse of the NPV was scanned (for scanning t_A) to select different temporal positions within the molecular beam. For each position, the timing of the probe laser was changed for the Δt scan to obtain the speed distribution (derived from $v = d/\Delta t$).

The measured result and derived speed distribution are shown in Fig. 3.8 for 0.1% NO/He. The DDS is shown in Fig. 3.8(a) where each pixel in the image contains a set of 3D data: ion intensity (in false color representation), time delay t_A) on the vertical axis, and pump-probe delay Δt on the horizontal axis. Note that the DDS of a "perfect" pulse should be as small as possible in both horizontal and vertical directions, whereas in reality an "s" form is found where early in the pulse the beam is faster than average and late in the pulse slower than

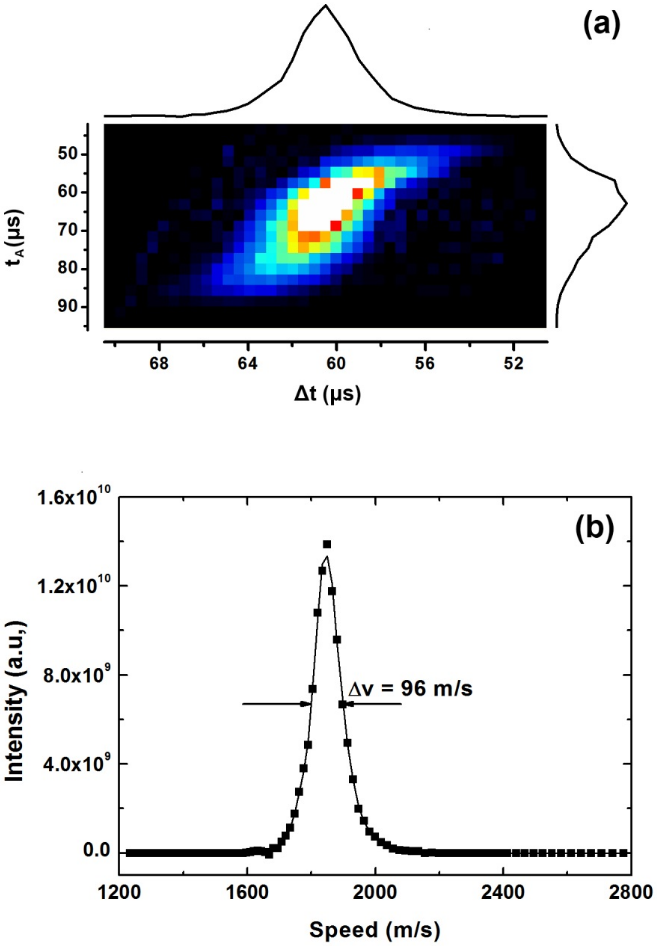

Figure 3.8: Results from 0.1% NO in He. (a) 3D image taken using a pump-probe scheme: pump-probe delay at the horizontal axis, and NPV-pump delay at the vertical axis. Measured ion intensities are represented in false color representation. The curve above the image (derived from integration of ion intensities along vertical axis) presents the travelling time distribution of the whole pulse packet between pump and probe position. The curve on the right side of the image (from integration of ion intensities along the horizontal axis) displays the molecular pulse profile at the pump position. (b) Overall speed distribution at the pump position: the mean speed is about 1850 m/s and the speed spread in the form of Δv_{FWHM} = 96 m/s, the speed ratio is 32 ($S = 1.66 \cdot v/\Delta v_{FWHM}$). The curves drawn through the dat points are only meant to guide the eye.

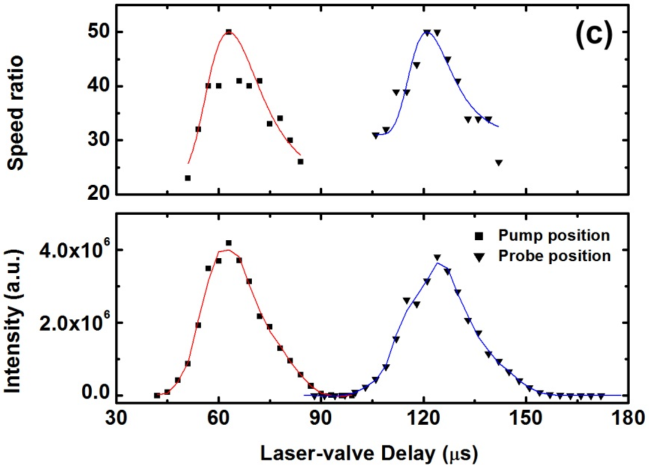

Figure 3.8: (c) Molecular beam pulse profile at the pump position (left curve of bottom figure) and probe position (right curve of bottom figure). Corresponding distributions of the speed ration S are shown in the upper figure.

average. The horizontal dimension of the DDS reflects the speed distribution (every line in a speed distribution is a certain point in the pulse) whereas the vertical dimension shows the temporal profile of the pulse (every column in a temporal profile is a certain velocity group of the pulse). When summing the vertical profiles together, the overall temporal profile of the pulse is obtained (shown as the vertical distribution next to the image). Similarly, when summing the horizontal profiles together one gets the overall speed distribution of the pulse (shown below the DDS) after conversion from time to speed (see Fig. 3.8(b)).

From this figure, it is found that the overall speed distribution curve for He as carrier gas peaks at 1850 m/s and has a FWHM of ~96 m/s. Therefore, the overall speed ratio $S = 1.66{\cdot}v/\Delta v_{FWHM} = 32$.

The t_A, Δt DDS data thus yield information on the temporal profile at position A and the speed distribution. This is enough information to also extract the temporal profile at position B, for each pixel t_A, Δt can be translated to the delay between valve and probe laser t_B through the relation $t_B = t_A + \Delta t$. The t_A, Δt DDS can thus be converted into a t_B, Δt DDS to extract the information for position B. For He, we only presented the first DDS, because it was very similar to the second DDS due to the high speed ratio.

Speed distributions and temporal profiles across the molecular beam pulse are shown in Fig. 3.8(c) . The left curve of the bottom figure displays the temporal profile at the pump position A (the same as the curve on the right hand side of Fig. 3.8(a)). The right curve is the temporal profile at the probe position B, extracted from the t_B, Δt DDS (not shown). At the peak position of the curve, the speed ratio reaches its maximum value, which is equal to about 50. However, the speed ratio decreases when the investigated position moves far away from the peak. This is because the gas density at the leading and falling edges is not as high as in the peak of the pulse resulting in fewer collisions and a decreased speed ratio. Comparing the parameters between pump and probe position, there is no obvious difference between speed ratio values, but the pulse duration at the probe position is somewhat broadened compared to the pumping position. This is reasonable considering the transmission of the molecular beam pulse packet with the translational speed distribution.

We performed the same measurement for a molecular beam of 0.5% NO/Ar, The main results can be seen in Figs. 3.9 and 3.10. The mean speed for this beam is about 620 m/s and the speed distribution has a spread of $\Delta v_{FWHM} = 94$ m/s. Therefore, the overall speed ratio is calculated to be about 11, much lower than the value of $S = 32$ for the molecular beam of 0.1% NO/He. At the peak of the pulse, the speed ratio exceeds 30, as shown in Fig. 3.10(b) .

The t_A, Δt DDS is shown in Fig. 3.9(a) , and the t_B, Δt DDS in Fig. 3.9(b). From these, it can be clearly seen that pulse duration is much broader at the probe position than that at the pump position. This is due to the lower speed ratio: the pulse packet broadens more during its transmission. It is also seen that later in the pulse the average speed slows down when using Ar as the carrier gas. When taking horizontal profiles in the DDS images, the speed distributions at particular points within the molecular beam are obtained. From these it follows that the speed distributions are narrower at the probe position compared to the pump position. This is why the speed ratios at the probe position are higher than at the pump position (see Fig. 3.10(b)). In a simple picture, it is quite clear why the speed ratio becomes higher when detected further downstream the nozzle: the further downstream from the nozzle, the beam has spread out spatially so much that the molecules in a small temporal window move with approximately the same velocity. Also, the valve opening time becomes short compared to the total flight time of the molecules, which results in a sharper definition of the speed. In summary, this double delay scan approach using tagged NO offers detailed insight into the actual speed distributions of the gas pulse.

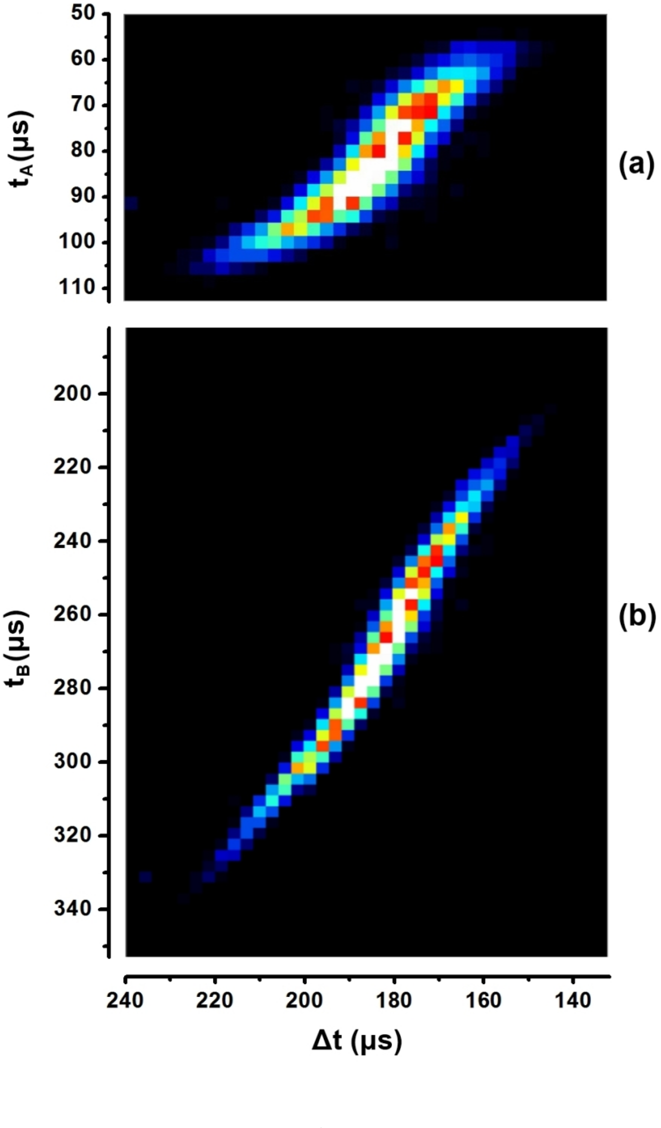

Figure 3.9: Speed ratio measurement for NPV produced molecular beam of 0.5% NO/Ar: (a) original 3D image for pump position and (b) derived one for probe position.

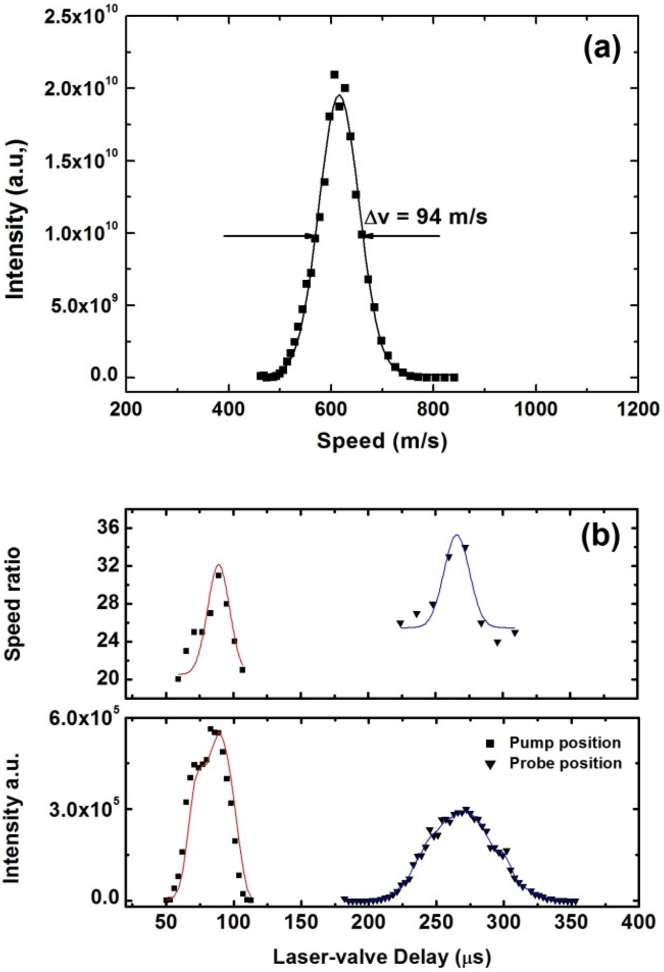

Figure 3.10: Speed ratio measurement for NPV produced molecular beam of 0.5% NO/Ar: (see also caption of Fig. 3.8) (a) Overall speed distribution, (b) molecular beam pulse profile at the pump position (left curve of bottom figure) and probe position (right curve of bottom figure). Corresponding distributions of the speed ration *S* are shown in the upper figure.

3.3.4 Other parameters

During the NPV performance characterization, some general parameters were also examined. First of all, we investigated the dependence of the pulse duration and speed distributions as a function of the backing pressure between 1 and 10 bars. As shown in the FIG data, the pulse duration becomes shorter with increasing backing pressure, but the speed ratio did not change much in this pressure range. This is in accordance with the findings of Even and co-workers,[121] who found the speed ratio to increase dramatically only at pressures well above the range we investigated. The rotational temperature also did not change very much with backing pressure.

Second, we investigated the pulse performance at different nozzle-skimmer distances. Increasing the distance from 8 to 13 cm did not change the speed ratios and rotational temperatures, only the measured pulse duration was a little longer. This is reasonable because of a broadening of the molecular beam during its transmission from the nozzle to the ionization region.

Third, when using higher beam intensities the pulses in the detection region became longer, especially at the tail. This effect was presumably due to clogging (or choking) effects by the 1 mm diameter skimmer. To reduce this effect, we replaced the skimmer with a 2 mm diameter one, which lead to similar results on the NPV performance. The actual skimmer interference effects remain an issue to be kept in consideration when designing experiments.

Fourth, we experimented also with a 200 μm diameter nozzle mounted on the same valve. Unfortunately, the design with the larger diameter O-ring was not optimized, leaving a dead volume behind the nozzle. As a result, the beam pulses from this nozzle were considerably longer. In a future design, this dead volume issue will be resolved. The results in this chapter are all for a small strip length and magnet sizes (5 mm). In our first design, we used 10 mm magnets and longer strips, which showed similar characteristics. Although we expected a better performance due to the smaller strip mass, the smaller magnetic field resulting in less driving power via the Lorentz force apparently limited the expected improvement.

3.4 Conclusions

In this chapter, we report on the design and operation of a novel homebuilt Nijmegen Pulsed Valve for the production of short and rotationally cold pulsed molecular beams. Short pulses with a FWHM = 20 μs (for 0.1% NO in 6 bars He) are measured at a distance of 12 cm downstream from the nozzle using a 1 mm diameter skimmer that is located 8 cm downstream from the nozzle. The resulting molecular beam has a higher density and shorter pulse length than other pulsed valves currently used in our lab using the same 0.5 mm nozzle diameter. The short gas pulses make it possible to operate the pulsed valve in setups with very modest pumping. Operation was demonstrated in a small differentially pumped system of two vacuum chambers containing the pulsed valve and a particle MCP detector. Both chambers were pumped by only 65 L/s pumps, with the beam "on," the detection chamber maintained a pressure around 1 $\times 10^{-6}$ mbar. The low gas load of the valve makes it possible to design very compact molecular beam machines with high quality cold and intense supersonic beams. These characteristics were obtained with a valve that is conceptually simple, easy to build and robust in operation. In addition, the low construction cost of the NPV and its electronics offers an interesting alternative for current commercially available valves.

The pulse width of the NPV should continue to decrease with increasingly higher backing pressures. Investigations by Even and co-workers[125] showed also that the speed ratio should become much higher by increasing the backing pressure to ~50 bars. In this study, when increasing the beam density by lengthening the valve opening time, the skimmed beam showed a long tail, indicative of a clogging effect. The leading edge still was very steep, its steepness increasing with backing pressure. Further investigations are ongoing towards the higher backing pressures to obtain colder, shorter, and high speed ratio molecular pulses. This involves a higher driving power to overcome the blocking force and using smaller diameter nozzles without dead volumes.

NPVs described here have been operating in our laboratory for at least 10^8 shots thus far without failure. Since the current strip also actively closes the nozzle, vacuum interlocks are necessary to protect against an eventual breakage. The measurements presented here use dilute gases. The thin Al strip should be gold coated for use with higher concentrations of aggressive gases. The Curie point of the Nd magnets used here is also rather low (~80 Ci) which means the NPV cannot be used at high temperatures. Work is underway to modify the valve for operation at lower temperatures, higher repetition rates and with corrosive gases.

3.5 Outlook

Since its commissioning, the NPV has demonstrated its capabilities in several experiments on small molecules.[131–133] For the experiments on large and complex biomolecules, as described in chapters 4 and 5, a molecular beam source is needed to cool the laser desorbed sample molecues to low temperature. Considering the efficient cooling effect of NPV produced molecular beam, it is expected that the NPV would improve the cooling of the laser desorbed biomolecules. This would allow us to employ high-resolution IR-UV spectroscopy to a wide variety of molecules.

4 Conformation-selective IR-UV study of the dipeptides Ac-Phe-Ser-NH_2 and Ac-Phe-Cys-NH_2:probing the SH$\cdots$O and OH$\cdots$O hydrogen bond interactions

Abstract

The conformational preferences of peptides are mainly controlled by the stabilizing effect of intramolecular interactions. In peptides with polar side chains, not only the backbone but also the side chain interactions determine the resulting conformations. In this paper, the conformational preferences of the capped dipeptides Ac-Phe-Ser-NH_2 (FS) and Ac-Phe-Cys-NH_2 (FC) are resolved under laser-desorbed jet cooling conditions using IR-UV ion dip spectroscopy and density functional theory (DFT) quantum chemistry calculations. As Serine (Ser) and Cysteine (Cys) only differ in an OH (Ser) or SH (Cys) moiety, this subtle alteration allows us to study the effect of the difference in hydrogen bonding for an OH and SH group in detail, and its effect on the secondary structure. IR absorption spectra are recorded in two different regions: 3200 cm^{-1} - 3600 cm^{-1} (NH stretch region) and 1400 cm^{-1} - 1800 cm^{-1} (NH bend and C=O stretch region). In combination with quantum chemical calculations the spectra provide a direct view on intramolecular interactions. Here, we show that both FS as FC share a singly γ-folded backbone conformation as the most stable conformer. The hydrogen bond strength of OH$\cdots$O (FS) is stronger than that of SH$\cdots$O (FC), resulting in a more compact gamma turn structure. A second conformer is found for FC, showing a β turn interaction.

4.1 Introduction

Proteins are important biomolecules in living cells, for example, they catalyze biochemical reactions, replicate DNA, act as biomolecular motors, and transport oxygen. The function of these biomolecules is made possible by dedicated three-dimensional structures. These structures depend on the sequence of amino acid residues, but also on their non-covalent intramolecular interactions (e.g. hydrogen bonds and dispersion interactions) and interactions with the molecular environment of the protein.[134;135] The molecular complexity of the biological and protein environments conceals many intrinsic structural properties. In order to obtain detailed conformational information, small peptides must be studied under isolated conditions with only intramolecular interactions present. Gas phase infrared (IR) spectroscopy is frequently used to determine molecular structure, and has proven to be a powerful tool in determining the intrinsic conformational properties of amino acids[136–138] and small peptides[139;140]. Using IR-UV ion dip spectroscopy[93], the conformational information of many neutral biological molecules has been retrieved.[55;141–148] The IR absorption frequencies of the amide (NH stretch, C=O stretch, NH bend) vibrations change dramatically under the influence of intramolecular interactions. A comparison of the peak positions with quantum chemical calculations, results in the secondary structure of peptides, revealing structural motifs, such as helices,[149] β-turns,[42;150] and γ-turns.[151;152]

In the present experiments, peptides are chemically protected on their termini to mimic the behavior of the peptide bonds, so that the molecules can be considered as model segments of a protein chain. The peptides studied in this paper are capped with an N-acetyl group (Ac-) on the N terminus and an amino group (-NH_2) on the C terminus.[42;59;149;150;152] Di-amides are the shortest species capable of forming γ-turns. Indeed, both protected alanine (Ala)[153] and Z-capped proline (Pro)[154] show a γ-turn as the most stable structure. In aromatic residues such as tryptophane (Trp)[155], phenylalanine (Phe)[150] and tyrosine (Tyr)[156], the extended β-strand-like conformation (referred to as β_L) dominates. When lengthening the sequence of amino acids, secondary structure β-turn conformations were found for protected dipeptides (specifically tri-amides), which probably competes with the locally preferred γ-turn conformation. Previous work on the isolated protected peptides Ac-Phe-Xxx-NH_2 (Xxx = Gly, Ala. Val, Pro)[42;59;151;152] demonstrated that a gamma-turn structure (β_L-γ_L) is the intrinsic prevalent conformation while β-turn structures are only found in minor population. However, for the protected peptide Ac-Phe-Phe-NH_2[55;157], the β-turn conformer is the most populated one, followed by a δ_L-γ_L structure, which was observed for the first time in a dipeptide in the gas phase, with a very minor contribution of the β_L-γ_L type. Biswal and his coworkers show that the β-turn structure is the only conformer found for the sulphur containing peptide Ac-Phe-Met-NH_2.[158]

In order to address the biologically important OH···O and SH···O interactions, we have studied the conformation preference of the capped peptides Ac-Phe-Ser-NH_2 (abbreviated as FS) and Ac-Phe-Cys-NH_2 (FC) by IR-UV ion dip spectroscopy in combination with high-level density functional theory (DFT) calculations. The chemical structures of the studied dipeptides (Fig. 4.1) are very similar, the only difference is an -OH in the Ser residue vs. an -SH in the Cys residue. The OH group, a strong hydrogen bond (H-bond) donor, is expected to form an intense H-bond with a nearby acceptor (e.g. C=O group from Ser residue in FS), which would stabilize the structure significantly. The SH group is a weaker H-bond donor. The initial research question was, whether the weaker SH$\cdots$O interaction would lead to different and/or more conformers for the sulphur containing dipeptide.

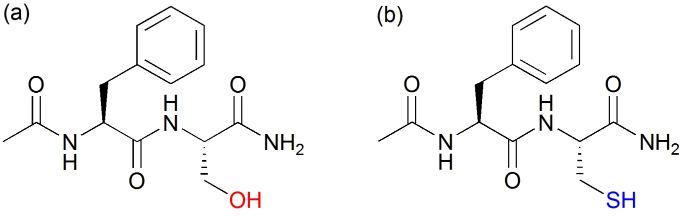

Figure 4.1: Chemical structures for (a) Ac-Phe-Ser-NH_2 (FS) and (b) Ac-Phe-Cys-NH_2 (FC), the structures differ by the substitution of a single atom

4.2 Experimental and computational methods

4.2.1 Experimental Methods

All experiments were performed using a pulsed molecular beam setup equipped with a laser desorption source and a time-of-flight mass spectrometer, which has been described in more detail in ref[159] and chapter 2. The capped dipeptides FS and FC were purchased from Genecust and were used without further purification. Before being applied on a solid graphite sample bar (50×15×1 mm), the samples were mixed with carbon black powder. This solid graphite sample bar was placed on a translation stage to provide a fresh sample every laser shot. A pulsed Nd:YAG laser (Polaris II, New Wave research) with a pulse energy of about 1 mJ at wavelength of 1064 nm was used to desorb the sample molecules from the graphite matrix. The neutral gas-phase molecules are directly cooled in a supersonic molecular beam of argon with a backing pressure of 3 bar, produced by a pulsed valve (R.M. Jordan Co.). About 10 cm downstream, the molecular beam is skimmed and enters the differentially pumped reflector time-of-flight (TOF) mass spectrometer. Here, the isolated molecules interact with a UV beam produced by frequency-doubled (BBO) output of a Nd:YAG (Innolas GmbH, Spitlight 1200) pumped dye laser (Radiant Dye, Narrowscan) using Coumarin 153. Ions were created by an one color (1+1) REMPI scheme[160]. The ions are accelerated into the reflector TOF tube and are detected with a dual microchannel plate detector (Jordan Co.). The UV laser is operated at 10 Hz with typical pulse energies of about 1.5 mJ.

IR absorption spectra are recorded using IR-UV ion dip spectroscopy.[48;161] In this approach, ions of a selected conformer are produced constantly from ground state molecules with a UV laser via a (1+1) REMPI scheme. About 300 ns prior to the UV laser beam, an IR beam in 3200 cm^{-1} - 3600 cm^{-1} region produced by YAG-pumped optical parametric oscillator (OPO) or in 1400 cm^{-1} - 1800 cm^{-1} region produced by the free electron laser FELIX (Free Electron Laser for Infrared eXperiments)[162], which is spatially overlapped with the UV beam interacts with the molecular beam. Whenever the IR laser is resonant with a vibrational transition of the selected conformer, population is transferred from the ground state to a vibrational level and a dip in the ion signal is observed. By measuring the ion yield of the mass of interest as a function of the IR wavelength, a mass-selected IR ion dip spectrum is obtained. To minimize signal fluctuation due to long-term UV power drifts and changing source conditions, alternating IR-off and IR-on signals are measured by operating the IR laser at 5 Hz and the UV laser at 10 Hz. To identify the number of conformers for each studied dipeptide, IR-UV hole burning spectroscopy has been used. Here, the IR laser is fixed on a frequency where only one selected conformer absorbs. By scanning the UV laser, depletion occurs for peaks in the REMPI spectrum originating from the same conformation.

4.2.2 Theoretical Methods

To assign structures for conformers of studied peptides, quantum-chemical calculations were performed. The computational method has already been described in more detail previously.[61;163] First of all, the simulated annealing (SA) approach using the GROMACS4 package[164] and the amber99sb force field[96] is applied for the conformational search. Secondly, about 30 low-energy conformations generated in the SA approach are optimized at the B3LYP[99]/6-31G(d,p) level of theory using the Gaussian09 program package.[165] Finally, the 15 lowest energy structures are optimized again using the B3LYP functional with the 6-311+G(d,p) basis set, and meanwhile their harmonic vibrational frequencies are calculated. To correct for anharmonicity, a scaling factor of 0.96[42;151;166] and 0.9845[61;163] was used in 3200 cm^{-1} - 3600 cm^{-1} region and 1400 cm^{-1} - 1800 cm^{-1} region respectively.

Although B3LYP is frequently used for frequency calculations of biomolecules, dispersion interactions are not taken into account.[167] In order to estimate the effect of this deficiency, the dispersion energy corrected functional B97-D[100] is also used here to optimize structure and calculate frequencies. Here, in 3200 cm^{-1} - 3600 cm^{-1} region, a scaling factor of 0.976 was used for anharmonicity correction. Moreover, for backbone NH and NH_2 stretches, the theoretical frequencies can also be corrected using mode-dependent scaling method determined by comparing theoretical and experimental results from a library of previously assigned peptides.[52] Theoretical scaled frequencies f^{th} were obtained using the empirically derived equation $f^{th} = a \times {f_0}^{th} + b$ (with ${f_0}^{th}$, original theoretical frequency), where the set of (a, b) parameters were (0.92135, 188 cm^{-1}) for NH stretch, (0.63115, 1210 cm^{-1}) for NH_2 symmetric stretch and (0.60872, 1324 cm^{-1}) for NH_2 asymmetric stretch. The relative energies of the most stable conformations presented in structure assignment are obtained from the B97-D/6-311+G(d,p) level of theory.

4.3 Results

4.3.1 REMPI Spectra

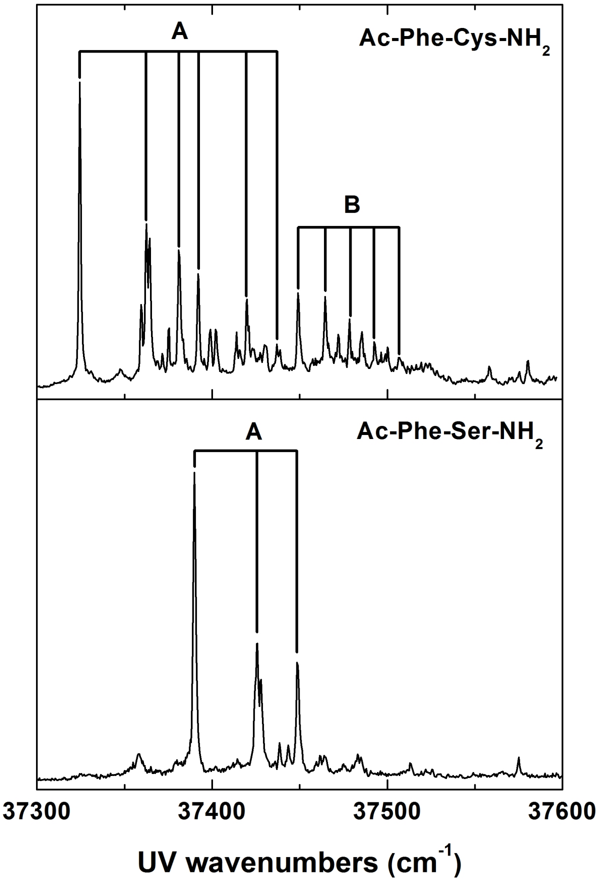

Figure 4.2: Mass-selected one color REMPI spectra of protected dipeptides Ac-Phe-Ser-NH_2 (low panel) and Ac-Phe-Cys-NH_2 (top panel) in the origin region of the $S_1 \leftarrow S_0$ transition. According to the results of the IR-UV hole burning experiments, conformers are identified and labeled.

Figure 4.2 presents the UV REMPI spectra of the studied dipeptides in the origin $S_1 \leftarrow S_0$ spectral region (from 37300 to 37600 cm^{-1}). The mass spectra of both FS and FC are dominated by a parent mass peak with very minor fragment peaks, indicating that both dipeptides are brought intact into the gas phase. The narrow features of the REMPI spectra reflects an efficient rovibrational cooling process during the expansion. The REMPI spectrum of FS shows a sharp main peak at 37390 cm^{-1}, two additional peaks 37426 cm^{-1} and 37449 cm^{-1} and some smaller bands. IR-UV ion dip spectra were recorded in amide A region for these three UV wavelengths. The IR spectra at these UV wavelengths were identical, indicating that they originate from the same conformation.

The presence of only one conformer was confirmed by IR-UV hole burning measurements, where the IR laser was fixed on one of the IR transitions while the UV laser was scanned. We found that all peaks in the REMPI spectrum were depleted at any one of the five IR positions (see Figure 4.3A). On the red side of

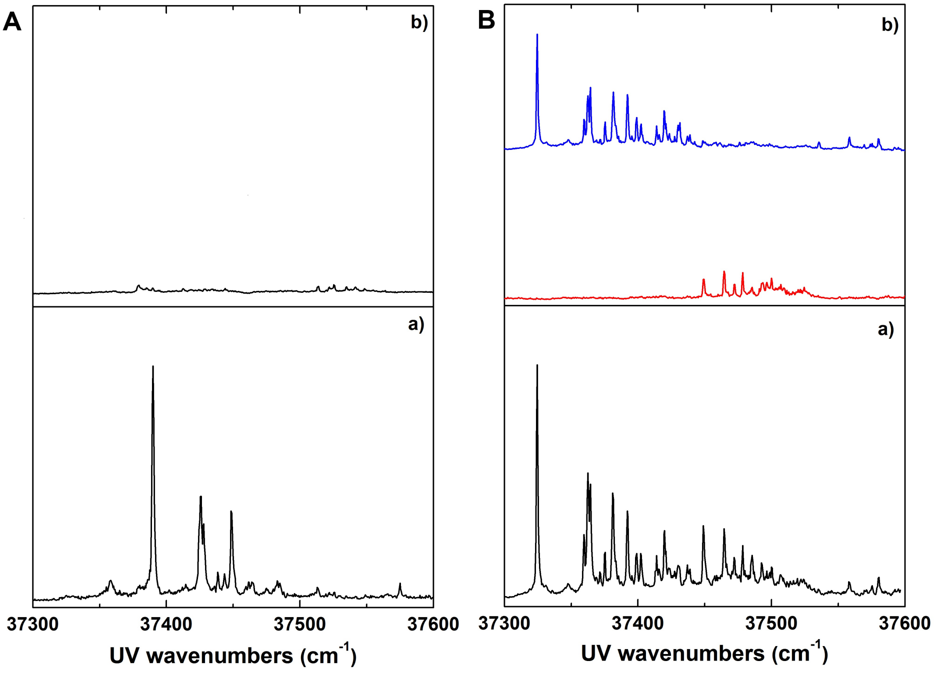

Figure 4.3: REMPI spectrum (panel a) and IR-UV hole burning spectra (panel b) of Ac-Phe-Ser-NH_2 (FS, A) and Ac-Phe-Cys-NH_2 (FC, B). For FS, IR burning laser is fixed at any vibrational frequency of the 5 modes showed in Fig. 4.4A. All REMPI signal is depleted, indicating that they originate from the same conformer; For FC, IR burning laser is fixed at 3362 cm^{-1} (red color) and 3395 cm^{-1} (blue color) respectively. Combination of the two hole burning spectra forms REMPI spectrum, indicating that two conformers of FC exist.

the origin, a hot band was observed, from which a vibrational temperature of 15 Kelvin was estimated for the jet cooled molecular beam.

The REMPI spectrum of FC (the sulphur containing peptide) is clearly different. The number of transitions is large compared to that of FS, indicating a more complex Phe environment and as we will see the presence of two conformers. The combined results of IR-UV ion dip and IR-UV hole burning measurements (see Figure 4.3B) show that apart from the most intense conformer (labeled A), a second conformer (labeled B) is present. Conformer A is characterized by an intense origin band at 37325 cm^{-1} with a vibrational progression expanding over more than 100 cm^{-1}, while the origin of conformer B lies 37450 cm^{-1} and has a smaller vibrational progression (50 cm^{-1}). The similar REMPI spectral features, both relative intensity as well as the distance between the peaks, for FS and conformer A of FC suggest that the Phe environments in these two species are comparable.

4.3.2 Infrared Spectra

The serine-peptide (FS). The IR spectrum of FS (Fig. 4.4, panel A) has been recorded in the amide A region with the UV laser parked on the peak at 37390 cm^{-1}. In this region, five modes are expected, namely the O-H stretching vibration, two N-H stretching modes, and the symmetric and asymmetric NH$_2$ stretching vibrations. The frequency of a free NH stretching vibration lies in the 3450-3500 cm^{-1} range and may shift when involved in a weak interaction such as C$_5$ or NH-π interaction, to the range 3420-3460 cm^{-1}. A red-shift to below 3400 cm^{-1} is observed upon strong H-bonding as in C$_7$ or C$_{10}$ interactions.[150] The asymmetric (higher frequency) and symmetric N-H stretching modes of the C-terminal amino group are typically separated by 117 cm^{-1} when the amino group is not involved in H-bond interactions.[150] However, if one of the NH oscillators is involved in an intramolecular H-bond, this doublet split increases together with the shift of symmetric N-H stretching frequency toward 3250 cm^{-1}.[59] The stretching mode of a free hydroxyl group lies in the 3620 to 3670 cm^{-1} region, and red shift upon H-bonding. Therefore, we assign the peak at 3556 cm^{-1} to the OH vibration red shifted due to a strong H-bond interaction, and the bands at 3517 cm^{-1} and 3357 cm^{-1} to the H-bonded NH$_2$ asymmetric and symmetric vibration. The two peaks 3403 and 3454 cm^{-1} in the measured IR spectrum of FS are associated with the stretch vibration of two NH groups.

The magnitudes of the red-shifts in the IR spectra indicates strong intramolecular H-bond interactions, such as C$_7$ or C$_{10}$. By comparing the experimental spectrum to DFT predictions, it was found that the lowest energy structure shows a C$_5$ interaction (β_L) for the Phe residue and a C$_7$ interaction (γ_L) for the Ser residue. Fig. 4.4 (panels B-F) shows the calculated spectra of five lowest energy structures using the B97-D functional. The absorption lines of the calculated frequencies were convoluted with a Gaussian line shape function with a full width at half-maximum (FWHM) of 5 cm^{-1} to match the observed experimental line width. The black bars present the peak positions of the vibrational modes so

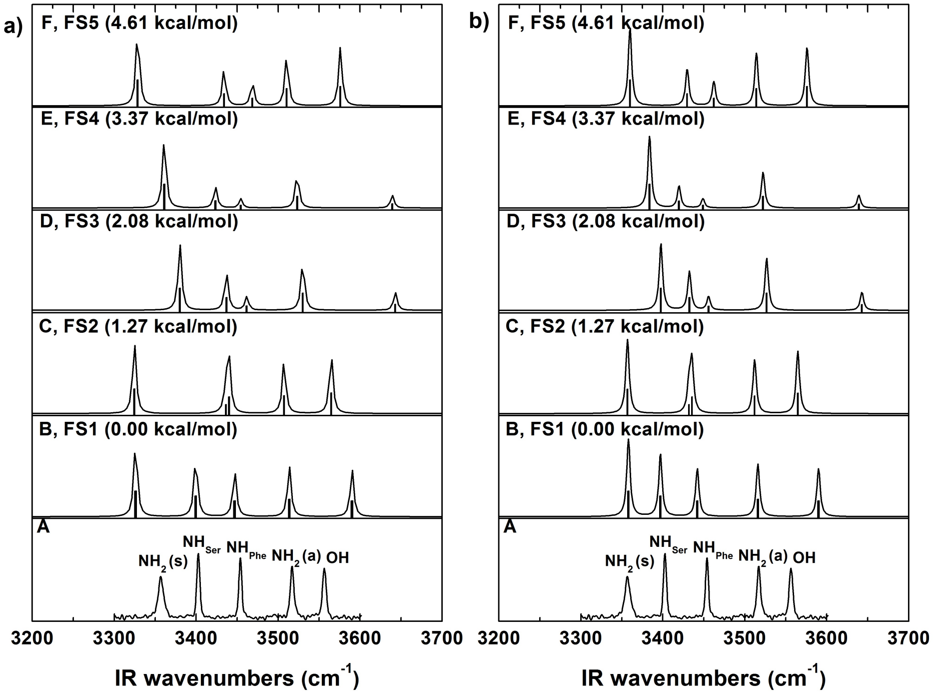

Figure 4.4: IR-UV ion dip spectra of FS (panel A, UV wavelength used is 37390 cm^{-1}), and the theoretical spectra of the five lowest energy structures (panels B-F), calculated at the B97-D/6-311+G(d,p) level of theory. The frequencies of the theoretical spectra are scaled (a) by a factor of 0.976 (b) using mode-dependent factor (0.976 for OH vibration band) to account for anharmonicity. The experimental spectrum is assigned to structure FS1 in the form of β_L-γ_L.

that the overlapping bands can be identified. The calculated spectrum of the lowest energy structure FS1 (β_L-γ_L, Fig. 4.4B) reproduces the experimental spectrum very well. Furthermore, the comparison of zero-point corrected energy and Gibbs free energy at 300 K (see Table 4.1) confirms that FS1 is the most stable conformer. To increase the predictive power of DFT, we also applied a frequency correction by a mode-dependent scaling method (see Fig. 4.4b),[52] the result of which also indicates that FS1 can be assigned to the observed conformer. Among other lowest energy structures, FS2 and FS5 are very similar to FS1. Nevertheless, the C_5 H-bond is absent in FS2 while dispersion interactions are not observed in FS5, which makes these structures less stable. Additionally, FS3 and FS4 are β-turn type structure and their calculated spectra do not match to experimental spectrum.

Table 4.1: Relative Electronic Energies (Eelec), Zero-point corrected Energies (ZPE) and Gibbs Free Energies at 300 K (ΔG) in kcal/mol for the Lowest-Energy Structures of Ac-Phe-Cys-NH_2 and Ac-Phe-Ser-NH_2.

	B97D			B3LYP		
	E_{elec}	ZPE	ΔG	E_{elec}	ZPE	ΔG
FC1	0.00	0.00	0.00	0.27	0.32	0.43
FC2	0.60	0.57	1.18	0.66	0.60	0.59
FC3	0.78	0.88	1.88	2.09	2.00	2.06
FC4	1.64	1.64	1.20	0.00	0.00	0.00
FC5	1.82	1.86	2.23	1.69	1.80	2.12
FS1	0.00	0.00	0.00	0.00	0.00	0.00
FS2	1.27	1.41	0.93	0.06	0.29	0.38
FS3	2.08	1.98	1.45	2.17	2.08	2.01
FS4	3.37	3.18	2.17	1.66	1.58	1.62
FS5	4.61	4.28	2.55	1.81	1.72	0.85

The cysteine peptide (FC). The experimental IR spectra of FC are presented in Fig. 4.5. The bottom trace shows the prominent conformer A, while the top trace of Fig. 4.5 shows the minor conformer B. Four modes are expected to appear in the studied infrared region, since the weak SH vibration is expected to lie around 2550-2600 cm^{-1}. This band is too weak to observe with the used IR laser system. For conformer A, only three peaks are observed, which indicates that two modes are overlapping. This is supported by the comparison of the FWHM of the three peaks. The FWHM of the modes are 8, 5 and 5 cm^{-1} for the peak at 3362, 3454 and 3522 cm^{-1} respectively, suggesting that the peak at 3362 cm^{-1} in fact contains two different near degenerate modes. The peak position suggests that this band combines the NH_2 symmetric vibration and one of the backbone NH stretch vibrations. The peaks at 3454 and 3522 cm^{-1} can be assigned to the stretch vibration of the other NH group and NH_2 asymmetric vibration, respectively. The split in frequency of 160 cm^{-1} between the symmetric and asymmetric vibration of the NH_2 group of FC differs only by 5 cm^{-1} compared to the splitting in FS (3357 and 3517 cm^{-1}), suggesting a similar local environment and intramolecular interactions for the NH_2 moiety. The frequencies of the backbone NH peaks at 3362 cm^{-1}, with strong intramolecular interaction, and at 3454 cm^{-1}, with much weaker intramolecular interaction, are due to NH groups involved in intramolecular interactions.

For conformer B of FC, the peaks at 3395 and 3529 cm^{-1} are assigned to the NH_2 symmetric and asymmetric modes while the remaining two peaks at 3440 and 3454 cm^{-1} correspond to the stretching vibrations of the two backbone NH groups, both only weakly interacting with other groups. The small peak at 3362 cm^{-1} is attributed to the more abundant conformer A, which is weakly ionized at the UV wavelengths selected for conformer B. The frequency splitting for the NH_2 stretching modes is 134 cm^{-1}, which is less than the 160 cm^{-1} splitting when

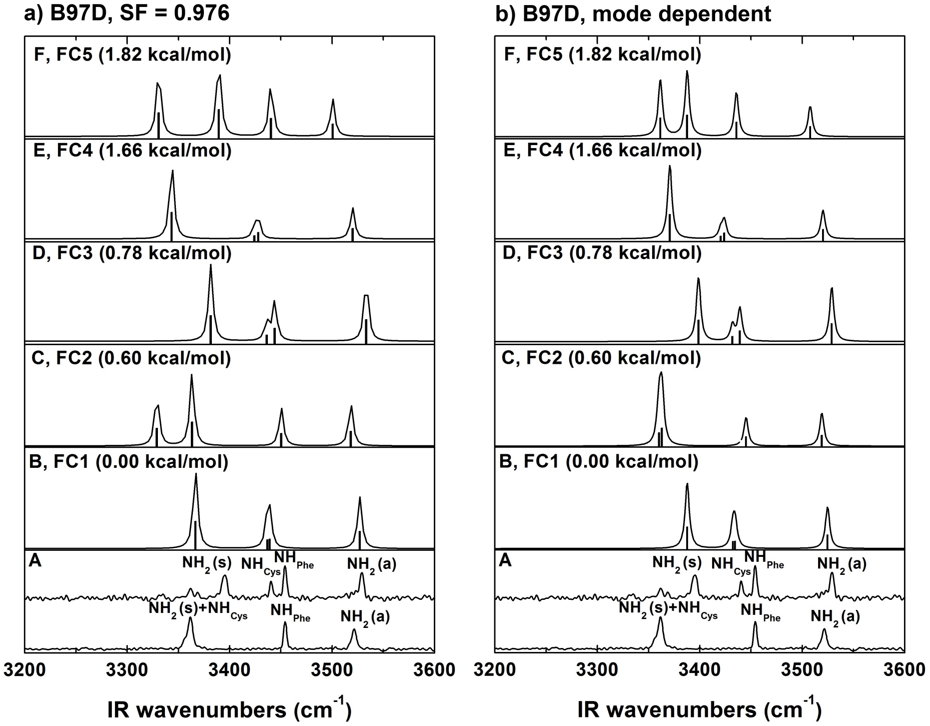

Figure 4.5: IR-UV ion dip spectra of FC (panel A, main conformer: bottom trace with UV wavelength of 37325 cm^{-1}; minor conformer: top trace with UV wavelength of 37450 cm^{-1}) and the theoretical spectra of the five lowest energy structures (panels B-F), calculated at the B97-D/6-311+G(d,p) level of theory. The frequencies of theoretical spectra are scaled (a) by a factor of 0.976 (b) using mode-dependent factor. The main conformer is assigned to the structure FC2 in the form of β_L-γ_L, while the β-turn structure FC3 is assigned to the minor conformer.

the NH$_2$ group is involved in a C$_7$ interaction. However, this is still more than the 117 cm^{-1} splitting for unperturbed NH$_2$ vibrations,[59] indicating the presence of a weak interaction such as a C$_{10}$ interaction.

Conformer A of FC can be assigned to the structure FC2, since all the other low energy conformations found predict that the frequencies of the backbone NH stretching modes are close, while they are separated by 92 cm^{-1} in the experiment. The FC2 corresponds to a β_L-γ_L structure (a C$_5$ interaction for the Phe residue and C$_7$ interaction for the Cys residue). For conformer B, the spectrum of structure FC3 obviously reproduces the measured spectrum the best compared to those of the other calculated structures. As speculated earlier, the structure is a β-turn type, exhibiting a C_{10} interaction. The lowest energy structure FC1 (presented in Fig. 4.5B), is not observed experimentally. The accuracy of the energies in DFT calculation is estimated to be about 1 kcal/mol[168]. Hence, the energy differences between structures FC1 and FC2, FC3 are only 0.60 and 0.78 kcal/mol are too small to be significant. Although FC1 becomes even more stable when considering the Gibbs free energy at 300 K (as shown in Table 4.1), the comparison between the measured frequencies and corrected theoretical frequencies using a mode-dependent scaling factor, see Fig. 4.6 clearly indicates that the spectrum of FC1 matches neither with conformer A nor with conformer B. Another explanation for not finding the calculated lowest energy conformer in our experiment can be the great structural similarity between FC1 and FC3 (see Fig. 4.6); FC1 could be

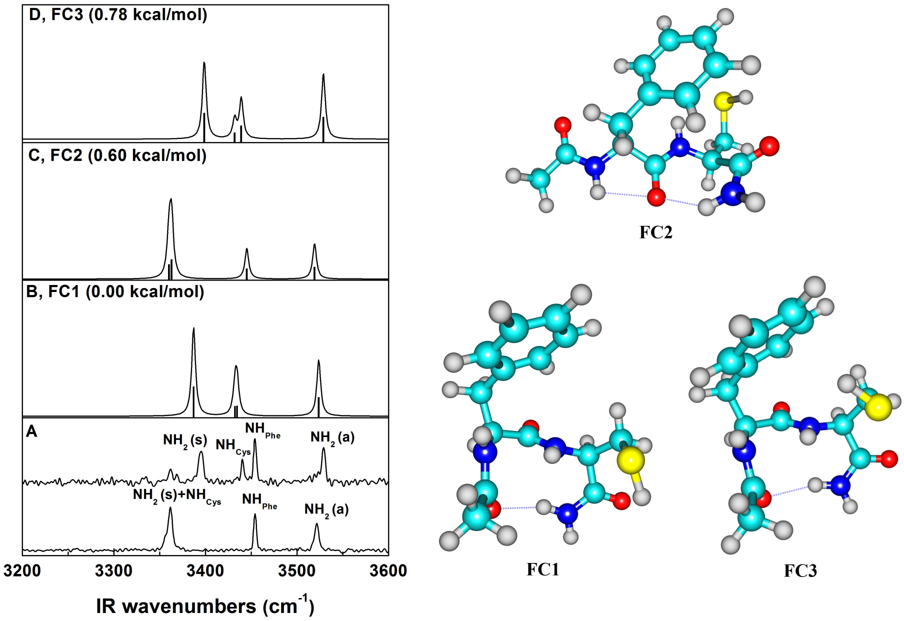

Figure 4.6: IR-UV ion dip spectra of FC(panel A) and the theoretical spectra of three lowest energy structures (panel B-D), calculated at the B97-D/6-311+G(d,p) level of theory. The frequencies of theoretical spectra are corrected by mode-dependent scaling factors. FC2 in β_L-γ_L type is assigned to the prominent conformer (bottom trace in panel A) while FC3 in β-turn type is assigned to the minor conformer (top trace in panel A) according to the spectra matching. Lowest energy structure FC1 is not observed probably because it is converted to the similar one FC3 during supersonic expansion since they only differs with each other in the direction of SH group.

converted to FC3 during supersonic expansion by only changing the pointing direction of the S-H bond. Additionally, it might be possible that the stabilizing effects by dispersion interactions involving the S-H group is underestimated in B97-D. In the β-turn structure FC3, the SH group is so close to the phenyl ring that dispersive interactions can lower the total energy. As in the case of the FS molecule, we have applied the mode-dependent scaling method to FC as well (see Fig. 4.5b), and the results shows that FC2 and FC3 can be assigned to the observed main conformer and minor conformer respectively.

4.4 Discussion

4.4.1 Conformational assignment

The conformational assignment of the experimental spectra of FS and FC is supported by DFT calculations using different functionals. Since in previous studies on capped Phe-Xxx (Xxx = Gly, Pro, Ala, Val, Phe),[42;55;59;151;152;157] the B3LYP functional was employed, we include this functional as well for the structural optimization and frequency calculations.

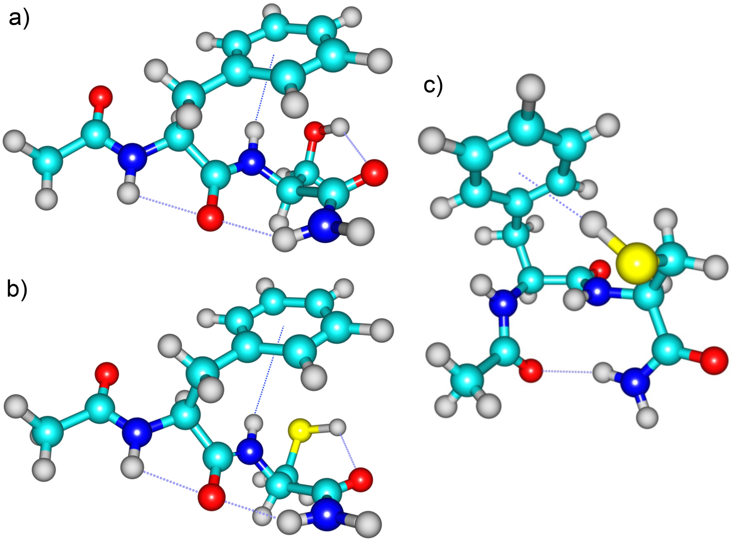

Figure 4.7: DFT optimized (B97-D functional with 6-311+G(d,p) basis set) (a) structure FS1 for the single conformer of FS in β_L-γ_L type, (b) structure FC2 for the main conformer of FC in β_L-γ_L type, (c) structure FC3 for the minor conformer of FC in β-turn type. Intramolecular interactions C_5 H-bond, C_7 H-bond, C_{10} H-bond, NH-π dispersion interaction, SH-π dispersion interaction, O-H···O and S-H···O H-bond are marked by dotted lines.

By comparing the experimental spectra in the amide A region with those resulting from calculations, the conformational preferences have been determined for FS (see Fig. 4.7a). The experimental spectrum is assigned to a β_L-γ_L conformer, with a C_5 interaction for Phe residue and C_7 interaction for Ser residue. The side-chain interacts with the backbone by a dispersion interaction between the NH group from the Ser residue and the phenyl ring from the side-chain of the Phe residue and by an H-bond between the OH group of the Ser side-chain with the C=O group of the Ser residue. As the B3LYP functional ignores dispersion

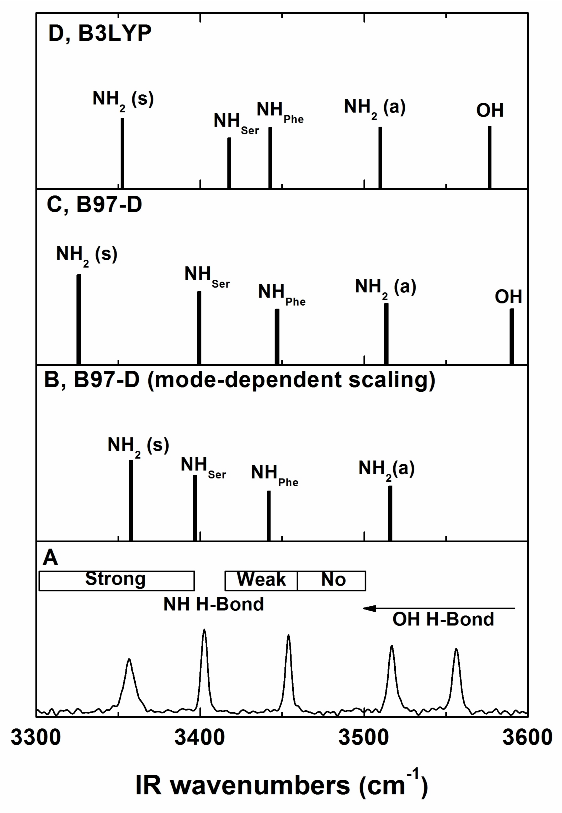

Figure 4.8: IR-UV ion dip spectra of FS (panel A) and the calculated frequencies of DFT optimized structure FS1 using B97-D/6-311+G(d,p) with mode-dependent scaling factors (panel B), B97-D/6-311+G(d,p) with scaling factor 0.976 (panel C), and B3LYP/6-311+G(d,p) with scaling factor 0.96 (panel D). In panels B-D, the corresponding modes were labeled. The OH frequency is missing in panel B, since there is no mode-dependent scaling factor for OH.

interactions, the calculated NH stretch vibration of the Ser residue is notably blue-shifted (see Fig. 4.8, panel D). For the same reason the OH stretch frequency is also blue-shifted using the B3LYP functional.

Since the studied peptides are expected to exhibit dispersion interactions, the more suitable functional for structure optimization and frequency calculation is the B97-D functional. Fig. 4.8C shows the calculated frequencies of the assigned conformational structure of FS using this B97D functional with a scaling factor of 0.976. The inclusion of an empirical correction for the dispersion interaction in the B97-D decreases the frequency mismatch between theory and experiment, observed in the B3LYP calculations to a large extent. Moreover, employing a mode-dependent scaling method for the NH frequencies in combination with the B97-D functional as introduced by Mons et al.,[52] results in an excellent match between the theoretical and experimental vibrational frequencies, as presented in Fig. 4.8B. Unfortunately, a mode dependent scaling factor for the OH vibration is not available, and the band is therefore not shown.

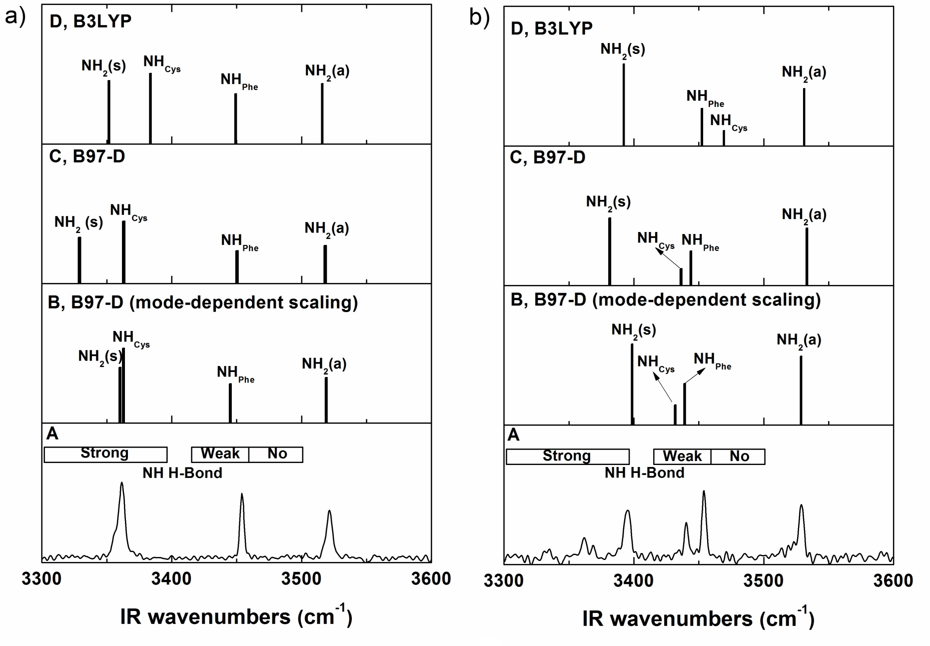

Figure 4.9: IR-UV ion dip spectra of FC (panel A) and calculated frequencies of FC2 (a) and FC3 (b) using B97-D using the mode-dependent scaling factors (panel B), B97-D/6-311+G(d,p) with SF 0.976 (panel C), and B3LYP/6-311+G(d,p) with scaling factor 0.96 (panel D). The corresponding modes were labeled above the bars indicating the vibrational frequencies.

In Fig. 4.9, the IR-UV ion dip spectra of FC are compared with DFT optimized vibrational frequencies. The experimental results of the main conformer shown in Fig. 4.9a, panel (A) is compared to DFT calculations using the B3LYP (Fig. 4.9a, panel D) and B97-D functionals (Fig. 4.9a, panel C) and to the B97-D functional with mode dependent scaling (Fig. 4.9a, panel B). With the mode-dependent scaling factor employed, the agreement between calculated and experimental frequencies for the β_L-γ_L conformer (FC2) is excellent (panel B). Therefore, the spectrum of the main conformer of FC is assigned to the structure FC2 displayed in Fig. 4.7b. The intramolecular interactions and the structure are highly similar to those for FS, with a backbone C_5 and C_7 interaction, an interaction between the SH group and C=O group of Cys and a dispersion interaction. The calculated energy of the structure FC2 is only 0.60 kcal/mol higher than the lowest energy structure found, indicating that the β_L-γ_L type is indeed a stable structure of FC. The similarity between the structure of FS and the main conformer of FC allows us to study the difference in the hydrogen bond strength for an OH and SH group in detail, as will be shown later.

For conformer B, the frequency splitting between the asymmetric and symmetric vibrations of the NH_2 group is 135 cm^{-1}, which is smaller than that for the strong gamma turn C_7 interaction (splitting of 160 cm^{-1}) for both FS as for conformer A of FC, but still more than the 117 cm^{-1} splitting in an unperturbed NH_2 group. Therefore, we speculate that the NH_2 group for conformer B is involved in either a weak C_{10} or a C_5 interaction. Considering the structure of FC, a C_5 interaction involving the NH_2 group can be excluded, hence the NH_2 is thus expected to be involved in a C_{10} interaction. Quantum chemical calculations confirm this assignment. Fig. 4.9b shows the comparison of the experimental IR spectrum of conformer B with the same set of calculations as in Fig. 4.9a with the assigned structure (shown in Fig. 4.7c), exhibiting a C_{10} β-turn interaction. Capped dipeptides Phe-Xxx, do not often display β-turn structures, nor are present as minor populations.[42;59;151;152] The SH group interacts with phenyl group, while the two NH groups are both not involved in any intramolecular interactions.

In addition, the structural assignment conclusions drew above could be further verified by the satisfied match between the measured spectra and those of assigned structures in Amide I and Amide II region (see Fig. 4.10). For FS, five revolved peaks were experimentally measured, which is also the case in the calculated spectrum of assigned structure FS1 in β_L-γ_L type. It was found that the peak at 1708 cm^{-1} in fact contains two different near degenerate modes: C=O stretch vibration from Ser residue and end cap Ac residue respectively. Due to involving in both C_5 H-bond and C_7 H-bond, a noticeable red shift is expected for the frequency of C=O stretch vibration from Phe residue, which is indeed observed as shown by the peak at 1663 cm^{-1}. Besides, the peaks at 1584, 1522 and 1484 cm^{-1} could be assigned to NH_2 scissor vibration, NH bend vibration from Ser residue and Phe residue respectively.

For FC, the measured spectrum of main conformer (FC_A) is very similar to that of FS, except for the region around 1700 cm^{-1} in which two resolved peaks

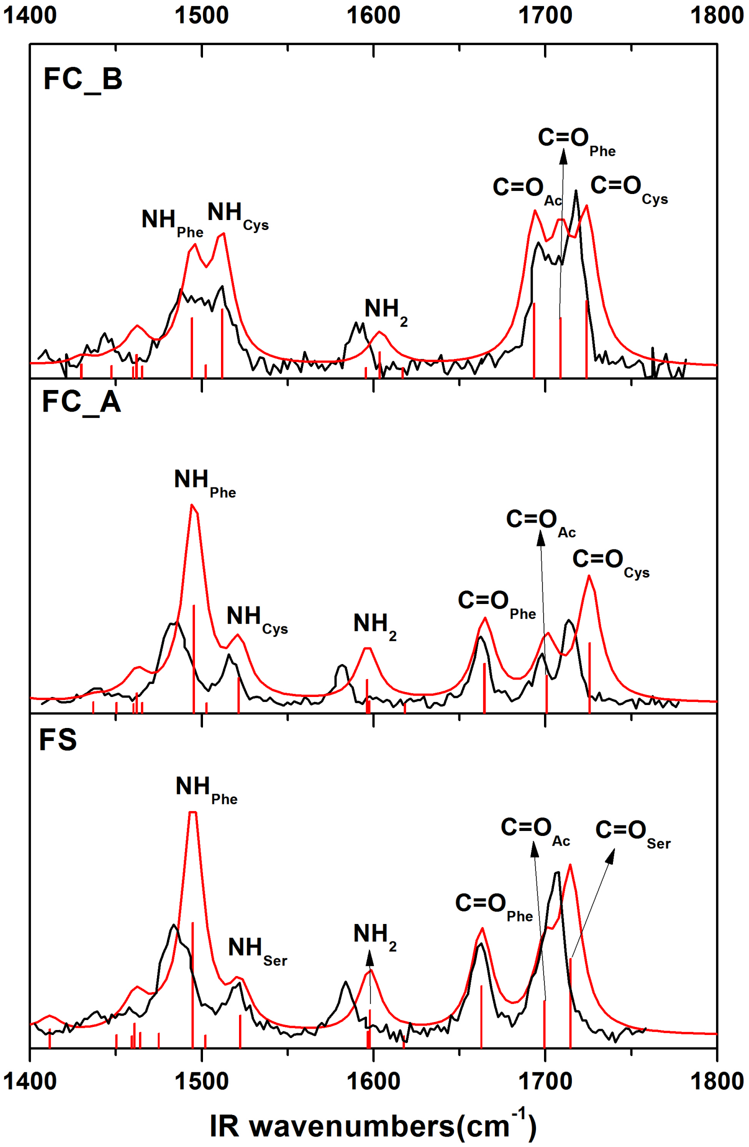

Figure 4.10: IR-UV ion-dip spectra (black, FS: bottom panel; FC_A: middle panel; FC_B: top panel) and the theoretical spectra of the assigned structures (red) using B3LYP/6-311+G(d,p) with scaling factor 0.9845. The corresponding modes were labeled above the red bars indicating the vibrational frequencies.

were observed in FC_A while in FS they are overlapped. This was expected since the assigned 3 dimensional structure of FC_A is almost the same as that of FS (also in β_L-γ_L type) and differs with FS only by one moiety substitution (CH_2SH and CH_2OH in side chain of Cys and Ser respectively). This subtle difference results in a small red shift of C=O stretch vibration from Cys residue in FC_A compared with that from Ser residue in FS, indicating that the H-bond strength of $SH\cdots O{=}C$ should be weaker than that of $OH\cdots O{=}C$ (further discussion shown in subsection 4.4.3). For the minor conformer of FC(FC_B), the measured spectrum is less resolved due to overlapping bands resulting from C=O stretch vibrations around 1700 cm^{-1} and two NH bend vibrations around 1500 cm^{-1}.

4.4.2 Serine versus cysteine in the Ac-Phe-Xxx-NH_2 dipeptide

Hydrogen bonds are essential in stabilizing the conformational structure. In peptides containing serine residues, such as Trp-Ser, cyclo Phe-Ser and the pentapeptide FDASV,[45;139;169]it was deduced that the hydroxyl group of the serine side-chain prefers to form a strong H-bond with the C=O group of the same residue. This intramolecular interaction is also observed here for the gamma turn structures (see Fig. 4.7a and b) for both FS and FC. The presence of polar functional groups in the side chains, such as the -CH_2OH in serine and the -CH_2SH in cysteine, is expected to increase the number of low energy conformers. De Vries et al. distinguished 5 different conformers for both uncapped cyclo (PheSer) as well as for uncapped linear PheSer.[169] The UV excitation spectrum of capped Ac-PheSer-NH_2 shows a number of peaks, indicating either multiple conformers or a conformer with a long vibrational progression. In our IR-UV hole-burning studies, only one dominant conformation is observed in our molecular beam environment (see Fig. 4.3A). For the cysteine containing peptide FC, which has a more dense UV spectrum, two conformations were revealed both with a significant vibrational progression (see Fig. 4.3B). Besides the corresponding gamma-turn, which is almost identical to FS, we found a structure containing a beta turn (see Fig. 4.7c).

Although conformational studies of peptides containing cysteine residue are not ample, studies on the cysteine amino acid itself have been performed.[170;171] Six conformers were observed for neutral, isolated cysteine using microwave spectroscopy. All these conformations have the SH group involved in an intramolecular hydrogen bond.[171] Moreover, in 4 out of the 6 conformers, the thiol group interacts with the carbonyl group forming a gamma turn, similarly to that we have found for the dominant conformer A of FC. Conformer B of FC adopts the beta turn structure type, see Fig. 4.7c. Apart from the basic characteristics of the beta turn C_{10} intense H-bond, there is also a strong dispersion interaction between the SH group of the Cys residue and the phenyl group of the Phe residue, which contributes significantly to the stabilization of the structure. Instead of forming a H-bond with the C=O moiety, the SH group interacts with phenyl ring here, indicating that the London force is comparable with the H-bond involving the SH group. However, this beta turn structure is not found for FS.

There are several possible reasons. First, the energy of beta turn structure of FS is higher (2.08 kcal/mol), while both conformers of FC lie within 0.18 kcal/mol of each other. Besides the possible lower abundance in the molecular beam, the UV absorption cross-section might be lower for the beta turn type of FS, causing a low sensitivity for probing this structure using IR/UV spectroscopy methods.

4.4.3 H-bond comparison between O-H$\cdots$O and S-H$\cdots$O in gamma turn peptides

Do our spectra reveal the difference in the H-bond interaction between an OH and SH group in detail (O-H$\cdots$O vs. S-H$\cdots$O)? In the measured spectra of FS and main conformer of FC (in type of β_L-γ_L structure), the stretch vibrational frequency is 1707 cm^{-1} and 1714 cm^{-1} for C=O$_{Ser}$ and C=O$_{Cys}$ respectively. The subtle shift is probably due to the difference between H-bond strength of OH$\cdots$O=C and that of SH$\cdots$O=C, as the stronger OH$\cdots$O=C H-bond should lead more red shift in the frequency of C=O stretch. This relationship between frequency shift and H-bond strength could be observed in the case of C=O$_{Phe}$ stretch as well. As involved in both C$_5$ and C$_7$ H-bonds, the stretch vibrational frequency of C=O$_{Phe}$ is found at noticeable red shift position 1663 cm^{-1} for both FS and main conformer of FC. For minor conformer of FC (β-turn structure), the vibrational frequencies of C=O stretch are found around 1700 - 1720 cm^{-1}. This is reasonable since only C=O$_{Ac}$ (frequency at 1696 cm^{-1}) is involved in weak H-bond C$_{10}$ interaction, while C=O$_{Phe}$ and C=O$_{Cys}$ (frequency at 1710 cm^{-1} and 1718 cm^{-1} repectively) are H-bonds free.

Apart from experimental evidence, theoretical calculations using B97-D functional yield distances between the carboxyl and the hydroxyl groups in the serine residue for FS of about 2.1 Å, which is typical for strong H-bonding and is comparable with the value 2.0 Å reported in the study of cyclo Phe-Ser.[170]This is significantly shorter than the distance between the SH group and the carboxyl group in the gamma turn conformer of FC of 2.4 Å. This difference reflects the difference in electronegativity of oxygen (3.5) and sulfur (2.5). The H atom in the SH group is less positively charged (0.11 according to the calculation) compared to the H atom in an OH group (0.33). This results in a weaker attraction between the H-bond donor SH and acceptor O=C, and in a H-bond strength in S-H$\cdots$O=C of conformer A of FC which is weaker than that in O-H$\cdots$O=C of FS. Although, the IR and UV spectra of both gamma turn structures are very different, the overall structure of both peptides is almost identical. They only differ in the hydrogen bond involving S-H$\cdots$O=C (FC) or O-H$\cdots$O=C (FS), effecting only the local structural compactness. The resulting 6-membered ring involving either the S-H$\cdots$O=C (FC) or the O-H$\cdots$O=C (FS) hydrogen bond shows minor differences in the planar or dihedral angle; however, as expected the bond length changes significantly, e.g. 1.4 Å for C-O while 1.8 Å for C-S and 1.0 Å for O-H while 1.4 Å for S-H reflecting the weaker hydrogen bond in FC (2.4 Å) with respect to FS (2.1 Å). Therefore, it is not hard to see that peptide containing Ser residue here is more compact than the one with Cys.

4.5 Conclusions

A conformational analysis for the isolated protected dipeptides Ac-Phe-Ser-NH_2 (FS) and Ac-Phe-Cys-NH_2 (FC) has been performed. Experimentally, only one conformer was found for FS, whereas two conformers were found for FC. The most stable structure of FS exhibits a dispersion interaction and two backbone H-bonds and forms a β_L-γ_L type backbone structure. For FC, two conformations were found. The main conformer also is in the form of β_L-γ_L type with a dispersion interaction and H-bond in the side chain of the Phe residue and the Cys residue respectively. The higher energy conformer consists of a backbone C_{10} interaction (β-turn), which is not often found in protected dipeptides or only as minor contributions. DFT calculations, employing the B97-D functional which introduces dispersion forces, allowed us to structurally assign our experimental spectra. Our results clearly show that mode-dependent scaling factors correct for the limitations of DFT calculations and are an important step forward in molecular structure identification. In all cases, the mode-dependent scaling factors made the structure identification possible beyond doubt. We thus recommend this method for structural assignment in the amide A region.

The existence of both S-H$\cdots$O=C hydrogen bond interactions as well as SH-π interactions suggest the important role of cysteine residues as a hydrogen bond donor in proteins and should definitely be considered. The slightly weaker S-H$\cdots$O=C hydrogen bond allows the competition with other type of interactions such as SH-π interactions resulting in the presence of both gamma turn as beta turn conformations. Not only the measured C=O strech frequencies, but also the distance between the OH group (FS) or the SH group (FC) and the backbone C=O group for the assigned β_L-γ_L type structures of the two dipeptides, obtained using the B97-D functional shows that the H-bond in the serine containing dipeptide is stronger than that of the cysteine containing residue, which was also expected due to the lower electronegativity of the sulfur atom compared to that of an oxygen atom. As a consequence, the β_L-γ_L type structure of FS is more compact than that of FC, which is also verified by the bond distances difference in DFT optimized structures.

5 Zwitterionic interactions in gas phase neutral peptides: The effect of the backbone rigidity on the salt bridge formation

Abstract

The formation of zwitterions has aroused great interest in protein folding studies due to their prominent role in stabilizing specific folds. This type of structure is hardly ever observed for neutral molecules in gas phase, except for the isolated peptides consisting of residues with acidic side chain Glu and basic side chain Arg. In this paper, the conformational preferences of the capped tripeptides Z-Glu-Xxx-Arg-NH_2 (Xxx = Gly, Ala or Pro respectively) are investigated. The selected peptides allow us to study the effect of flexibility of peptide backbones on possible zwitterion formation, ranging from small and compact (Gly, Ala) to the rigid Pro residue. Moreover, the Proline residue allows cis/trans orientation of the resulting peptide bond. Employing IR-UV ion dip spectroscopy under laser-desorbed jet cooling, IR spectra of each peptide in the NH stretching region (3150-3700 cm^{-1}) are acquired and compared with density functional theory (DFT) calculated spectra to perform structural assignment. Here, we show that for each peptide only one dominate conformer was observed; the experimental IR spectrum was found to be identical for all selected UV wavelengths from the REMPI spectrum. All peptides adopt zwitterionic structures, although zwitterion formation is less stable for the rigid Z-Glu-Pro-Arg-NH_2 than for the other two peptides. Apart from the salt bridge interactions in each peptide investigated, hydrogen bonds formed within backbones, between backbones and side chains, and dispersion interactions between NH/NH_2 and phenyl are found to play an important role in structural stabilization as well.

5.1 Introduction

During the past decades, the study on intramolecular interactions in peptides and proteins has attracted much attention because of their great structural and functional significance. Interactions such as hydrogen bonds (H-bonds) and dispersion interactions are ubiquitously present and play an important role in the formation of the backbone structure and the 3-dimentional shape of these molecules. However, there is another type of interaction, which greatly contributes to the stability of entropically unfavorable folding structures of peptides - the so-called salt bridge, a non-covalent interaction between oppositely charged residues.

The tendency of formation of a salt bridge in small peptides varies from case to case. For peptides with sufficient flexibility, the stability of a salt bridge can be supported by intramolecular interactions between two charged groups without much steric hindrance. In addition, intramolecular solvation, in which the charged group interacts with the polar group such as carbonyl oxygen of the peptide backbone, could also help stabilize this salt bridge interaction.[172] Even though, the formation of zwitterionic structures in peptides often lose the competition against the formation of canonical structures. For instance experiments on oligomers consisting of up to 8 glycine residues revealed that neither the protonated nor the sodiated molecules do fold into a zwitterionic form[173;174]. Infrared multiple photon dissociation (IRMPD) studies of AlaPhe·K^+, PheAla·K^+ and the larger Tyr-Gly-Gly-Phe-Leu yield canonical charge solvated structures where primarily the amide carbonyl oxygen solvates the metal ion[175;176]. However, residues with acidic side chains (Glu, Asp) or basic side chains (Lys, Arg) favour formation of salt bridges. The first experimental evidence for a gas phase protonated peptide adopting a salt bridge structure was reported by Prell and coworkers on ArgArg·H^+. The zwitterionic interaction occurs between the deprotonated C-terminus and two protonated guanidines[177]. In the case of the Lys-Glu dipeptide, the conversion from neutral state to the zwitterionic salt bridge state is triggered by addition of a water molecule[178]. Collision induced dissociation measurements of the singly protonated peptide Arg-Gly-Asp acid demonstrated that a salt bridge stabilized intermediate structure is generated in the fragmentation of the molecule.[179]

Not only the ionic peptide can fold to infer salt bridge interactions, but zwitterions can also be formed in neutral, isolated peptides[61;141;180;181]. All the peptides found in the zwitterionic form under molecular beam conditions contain the acidic residue glutamic acid and the basic residue arginine, which interact with each other through their side chains. Because of significant importance in the structural stability and functions of peptides and proteins, lots of research has been performed concerning the role of side chain interaction between these two residues. For instance, it was shown that the salt bridge interaction between Glu and Arg in eukaryotic protein kinases plays a role of center hub. Replacement of either residue by Ala causes not only the disruption of connectivity between structural segments, but also in a huge decrease in the catalytic efficiency of this enzyme.[182] In the chemotaxis protein CheW, this salt bridge interaction is believed to stabilize the local backbone structure and the relative position of the binding sites for the chemoreceptor and kinase[183]. Furthermore, in some cases

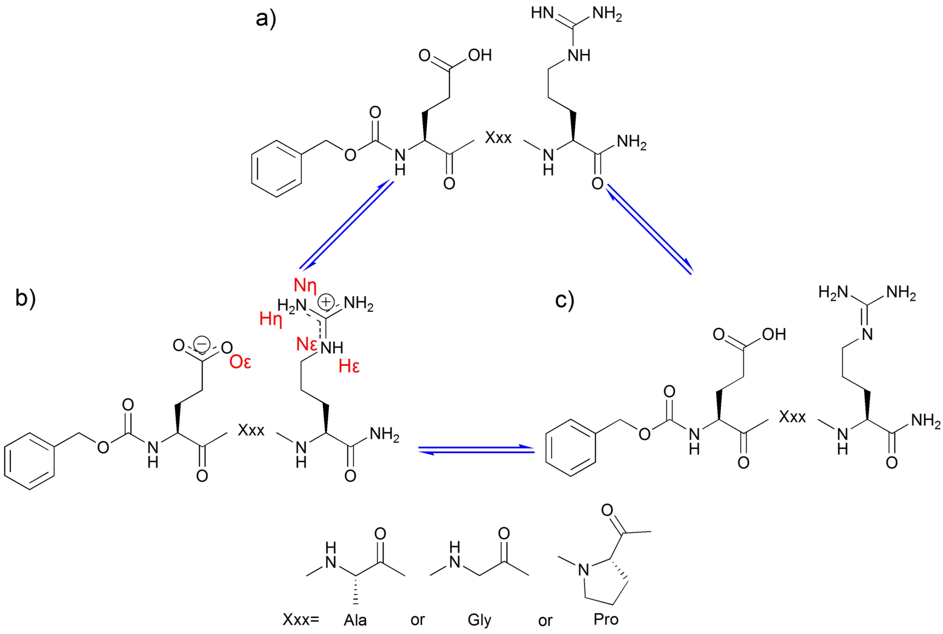

Figure 5.1: Chemical structures of Z-Glu-Xxx-Arg-NH_2 (with Xxx = Ala, Gly and Pro, respectively) in their (a) canonical, (b) zwitterionic and (c) tautomeric form. The labels describe the intramolecular interactions; the C=O group of Z-cap is labeled as O0, the NH and C=O group of the ith residue is labeled as Ni and Oi, respectively. Oε represents the oxygen of the carboxylic group in the Glu side chain, Nη and Nε in the guanidine group of Arg describe the terminal and non-terminal nitrogen, respectively.

there is even a specific requirement for the exact type of salt bridge interaction so that the peptide could perform its function. For example, the salt bridge interaction found in human chloride intracellular channel is characterized by two hydrogen bonds of which one is formed between one glutamate Oε (as shown in Fig. 5.1 for the detail of atom labeling system) atom and Hε atom of Arg while the other involves another glutamate Oε atom and Hη atom of Arg (defined as A type salt bridge interaction in our previous study[61]). This type of salt bridge also appears in the theoretical predictions[181] and our previous studies[61;141]. However, in the quantum and molecular mechanical simulations of the motor-enzyme F_0F_1-adenosine triphosphates ATPase, it was found that another type of salt bridge was formed between the side chains of Glu and Arg. Here, a bifurcated interaction is predicted between one of the Glu Oε atoms and the Arg Hε and Hη atoms[184] (C* type). Unfortunately, there is still lack of experimental evidence at the atomic level for the existence of this bifurcated type.

In this context, more experimental exploration on these interaction under controlled conditions would contribute greatly to our understanding to zwitterion formation. Questions such as what kinds of factors (e.g. number and/or flexibility of residues spacing between Glu and Arg) would influence the type and strength of this interaction are still waiting for unambiguous answers. Hence, in this paper, the gas phase structures of several neutral peptides containing Glu and Arg residues will be discussed. Instead of gradually lengthening the residue spacing between Glu and Arg[61], here we alter the center residue. The studied peptides are all in the form of Z-Glu-Xxx-Arg-NH_2, the chemical structures of which are shown in Figure 5.1. Residues with decreasing flexibility, namely Glycine (Gly), Alanine (Ala) and Proline (Pro), are selected as spacing residue to investigate the influence of the rigidity of the peptide backbone on the tendency of zwitterion formation and type of salt bridge interaction. By comparing experimental IR-UV ion dip spectra in the amide A region (3150 - 3700 cm^{-1}) with high-level density functional theory (DFT) calculations, detailed information on the 3-dimentional structure of the peptide could be obtained and different types of salt bridge interactions could be distinguished.

5.2 Experimental and computational methods

5.2.1 Experimental Methods

The experiments were performed on a home-built molecular beam setup consisting of a laser desorbed jet cooling source and a time-of-flight mass spectrometer, which has been described in more detail elsewhere.[159] Peptide samples Z-Glu-Gly-Arg-NH_2 (EGR), Z-Glu-Ala-Arg-NH_2 (EAR) and Z-Glu-Pro-Arg-NH_2 (EPR) were synthesized using Fmoc solid phase peptide synthesis from 1 *g* of Fmoc-Arg(Pbf)-Wang resin (0.7 mmol/g). The resin was swollen in DMF prior to use. Couplings were carried out with 3.0 equivalents of the required amino acid (Z-Glu(OtBu)-OH, Fmoc-Gly-OH, Fmoc-Ala-OH or Fmoc-Pro-OH), 3.3 equivalents of DIPCDI and 3.6 equivalents of 1-hydroxybenzotriazole hydrate (HOBt) in dimethylformamide (DMF), and all deprotections where performed with 20% piperidine in DMF (3 times 6 minutes). After each coupling and deprotection a Kaiser test was used to ensure the reaction had gone to completion.[185] The peptides were cleaved from the resin by treatment of the resin with a mixture of trifluoroacetic acid/water (95:5) for 2 hours, followed by precipitation in ether. The peptides were used as such after drying in air. The purity was higher than 95% according to LC-MS analysis. The samples were first carefully ground in an agate mortar and mixed homogeneously with carbon black powder. The prepared sample mixture was applied on a solid graphite sample bar. A pulsed Nd:YAG laser (Polaris II, New Wave research) with a pulse energy of about 1 mJ at a wavelength of 1064 nm was used to desorb the sample molecules from the solid bar which was placed on a translational stage to provide a fresh sample for every laser shot. The generated neutral gas-phase molecules are trapped and cooled in a supersonic molecular beam expansion of argon with a backing pressure of 3 bar. About 10 cm downstream, the molecular beam is skimmed and enters the differentially pumped reflector time-of-flight (TOF) mass spectrometer, where a UV beam produced by a Nd:YAG (Innolas GmbH, Spitlight 1200) pumped dye laser (Radiant Dye, Narrowscan) is utilized to carry out (1+1) REMPI of the isolated molecules. The UV laser is operated at 10 Hz with typical pulse energies of about 1.5 mJ.

To record IR spectra of the molecules of interest, IR-UV ion dip spectroscopy[141;161] is employed. In this technique, a constant ion signal is produced for a single conformer selected by the UV laser wavelength, which corresponds to an electronic transition of this conformer. About 300 ns prior to the UV laser beam, a YAG-pumped optical parametric oscillator (Laser Vision) produced IR beam, which is spatially overlapped with the UV interacts with the molecular beam as well. Whenever the IR laser is resonant with a vibrational transition originating from the same state of the selected conformer, a depopulation of this state occurs for the selected conformer and a dip in the ion signal is observed. By measuring the ion yield as a function of the IR wavelength, a conformation selective IR ion dip spectrum is obtained for the molecule of interest. In addition, to minimize signal fluctuation due to changing source conditions and long-term UV power drifts, alternating IR-on and IR-off signals are measured by operating the molecular desorption source and the UV laser at 10 Hz and the IR laser at 5 Hz.

5.2.2 Theoretical Methods

Quantum-chemical calculations were executed in order to assign the obtained IR spectra to specific structures of each studied peptide. The details of the applied computational method has already been described elsewhere.[61;163] In short, firstly, conformational searches were performed by the simulated annealing (SA) approach using the GROMACS4 package[164] and the amber99sb force field[96]. To allow structural rearrangements, the temperature in the simulation was raised to 1300K within 5 ps and cooled exponentially to 5 K in the next 15 ps. This process was repeated for about 1000 times and structures at 5 K in each repeat were saved. In the amber99sb force field, neutral Glu, Arg and the Z-cap had to be added manually.[61] Secondly, about 30 low-energy conformations generated in the SA approach are optimized structurally at the B97-D/6-31G(d,p) level of theory using the Gaussian09 program package.[100;165] Finally, using the B3LYP[99] and B97-D functional with the 6-311+G(d,p) basis set, the 15 lowest energy structures selected from the results of the second step are further optimized and their harmonic vibrational frequencies are calculated. To correct for anharmonicity of computed frequencies, (SF) is normally required. Although in some cases separate SFs for different vibrational modes were employed, it is not always applicable. For instance, at B3LYP/6-31+G(d) level of theory, individual SFs for NH/OH vibrational frequencies[186;187] resulted in a worse agreement for the capped dipeptide Ac-Phe-Ser-NH_2.[60] At B97-D/6-311+G(d,p) level of theory mode dependent SFs for different types of NH vibrations worked perfectly for capped Ac-Phe-Xxx-NH_2 dipeptides.[52] However, for the studied peptides where the guanidine tail of Arg is involved in proton transfer, this method may not necessarily be valid, since mode dependent SFs for protonated NH/NH_2 vibrations do not exist. Therefore, a fixed SF of 0.960 (for B3LYP/6-311+G(d,p)) or 0.977 (for B97-D/6-311+G(d,p)) was used in the IR region 3150 - 3700 cm^{-1} and the calculated frequencies were convoluted with a Gaussian line shape with a FWHM of 7 cm^{-1} in order to compare with the experimental spectra. Relative energies in terms of both zero point energy (ZPT) and Gibbs free energy at 300 K (ΔG, proven to be important in determining the conformational population at low temperature[188]) were calculated using both commonly used B3LYP functional as well as the dispersion-included B97-D functional. However, unless expressly stated, the energy described in the text is acquired by the B97-D functional since this method was found to predict the energies more accurately (even comparable with the higher correlation method MP2[163]) than the B3LYP functional which ignores intramolecular dispersion interactions[167].

5.3 Results

5.3.1 REMPI Spectra

The UV REMPI spectra of the three tripeptides EGR, EAR and EPR in the region from 37100 to 37900 cm^{-1} are presented in Figure 5.2. Although sufficient cooling of tripeptides could be achieved in the molecular beam,[150;189] all the spectra here contain broad features. This suggests that the studied molecules either have a short excited state lifetime the desorbed molecules are cooled insufficiently in the supersonic expansion. This has been observed before for similar families of molecules all containing the Arginine residue, showing the difficulties to cool Arg containing peptides, possibly due to their large and floppy side chain.[48;61;163] Moreover, these peptides fragment upon desorption (as can be seen from Fig. 5.3). Moreover, molecules with increasing size and degrees of freedom are harder to cool in a molecular beam environment.[46;190;191] Spectra with similar resolution have been observed in studies of various large and complex biomolecules.[61;69;192] Here, the REMPI spectrum of EGR shows several absorption peaks (37450 cm^{-1}, 37507 cm^{-1}, 37534 cm^{-1}, 37566 cm^{-1} and 37618 cm^{-1}) on top of a broad band from 37400 cm^{-1} to 37700 cm^{-1}. In the case of EAR, a broad absorption band is observed in the same UV range. However, the peaks on top of it are less resolved with the most intense absorption located at 37526 cm^{-1}. The REMPI spectrum of EPR shows very similar feature to that of EAR; a broad band consisting of several unresolved peaks.

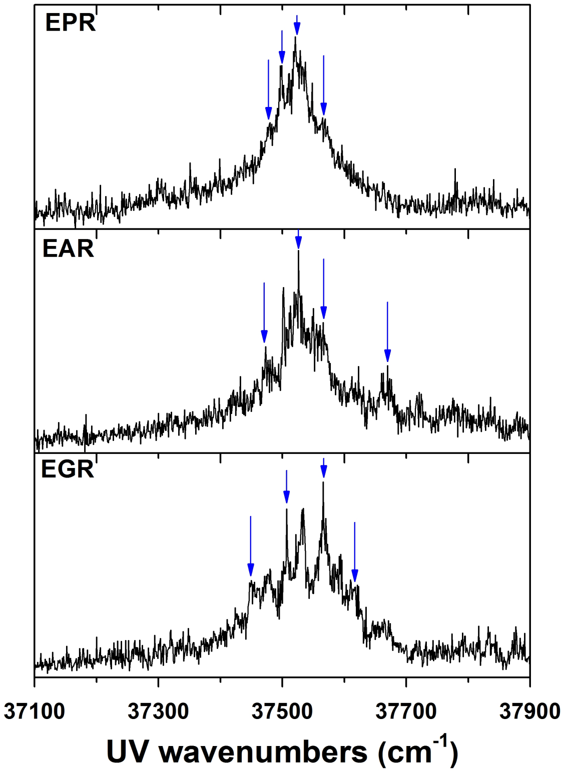

Figure 5.2: Mass-selected one color REMPI spectra of Z-Glu-Gly-Arg-NH_2 (EGR, bottom panel), Z-Glu-Ala-Arg-NH_2 (EAR, middle panel) and Z-Glu-Pro-Arg-NH_2 (EPR, top panel). The positions marked by blue arrows indicate the selected UV wavelengths at which IR-UV ion dip spectra were taken.

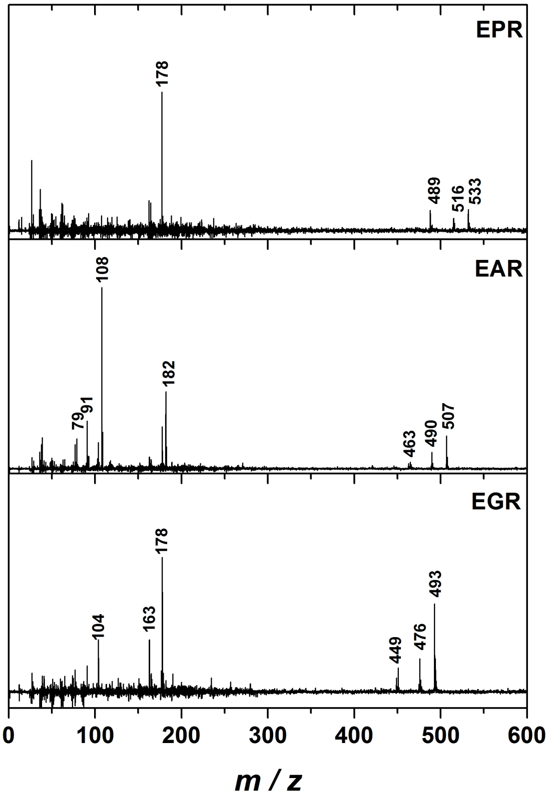

Figure 5.3: Time-of-flight mass spectra of Z-Glu-Gly-Arg-NH$_2$ (EGR, mass: 493.29), Z-Glu-Ala-Arg-NH$_2$ (EAR, mass:507.31) and Z-Glu-Pro-Arg-NH$_2$ (EPR, mass:533.33).

5.3.2 Infrared Spectra

Figure 5.4 presents the IR-UV double resonance spectra in the amide A region covering the O-H stretching vibration and the N-H stretching vibration (both symmetric and asymmetric stretching). The characteristic absorption frequencies of these vibrational modes are summarized in Figure 5.5. It can be seen that the vibrational frequencies depend strongly on the type of intramolecular interaction where the functional group is involved in. Starting from the free NH stretching to the backbone H-bond C_5(NH-π), C_{10}, C_7 interaction and H-bond in salt bridge, the frequency of the NH stretch vibration gradually red shifts. Additionally, the absorption peak broadens significantly when the vibrational group participates in intense interaction.

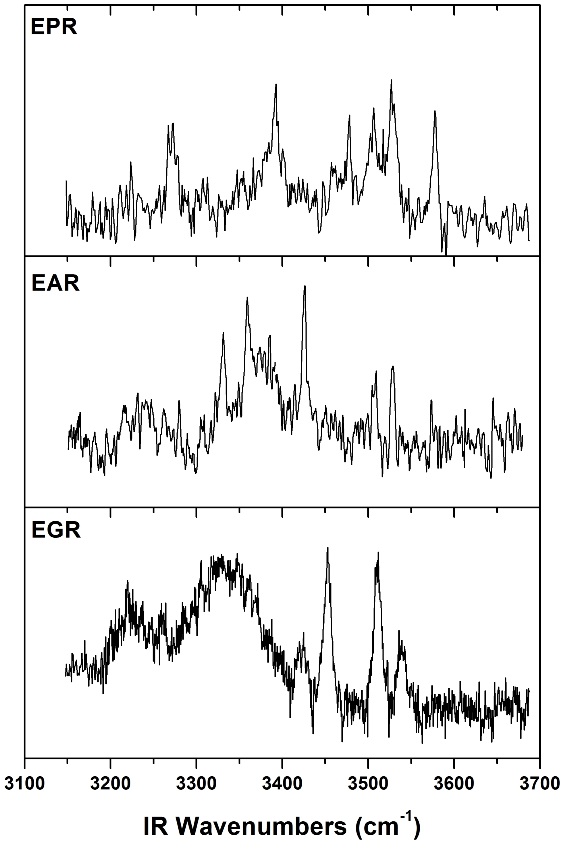

Figure 5.4: IR spectra of Z-Glu-Gly-Arg-NH_2 (EGR, bottom panel), Z-Glu-Ala-Arg-NH_2 (EAR, middle panel) and Z-Glu-Pro-Arg-NH_2 (EPR, top panel) measured by IR-UV ion dip spectroscopy.

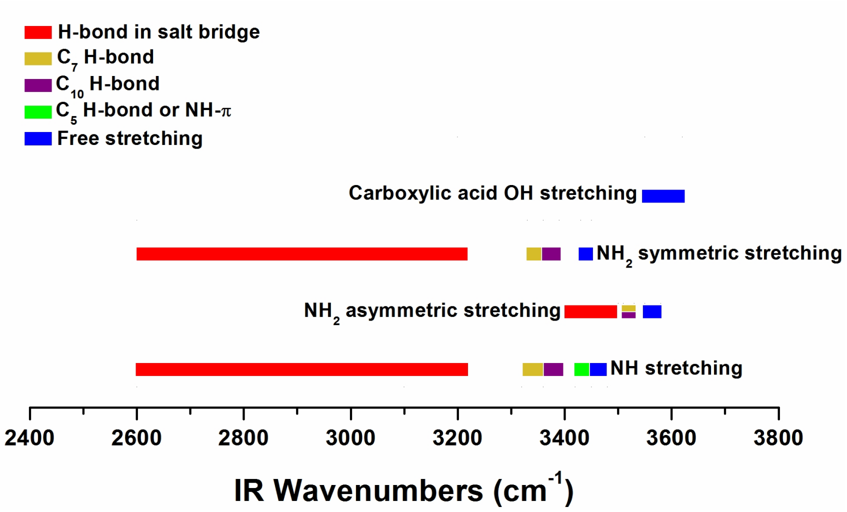

Figure 5.5: Overview of vibrational frequencies of NH, NH_2 and OH groups in free and H-bonded interactions, derived from gas phase measurements[59–61] and theoretical calculations using B3LYP/6-311+G(d,p) level of theory.

Z-Glu-Gly-Arg-NH_2 (EGR)

The IR spectrum of EGR was average of spectra recorded with the UV laser parked on the blue arrow marked peaks in the REMPI spectrum (UV wavelength at 37450 cm^{-1}, 37507 cm^{-1}, 37566 cm^{-1} and 37618 cm^{-1} respectively). An identical IR spectrum (see Fig. 5.6) was acquired when the UV wavelength is parked at the selected peaks, indicating that most likely only one conformer is present under our experimental conditions. We attribute the two intense bands in the 3500-3550 cm^{-1} region to the NH_2 asymmetric stretching vibration. The bands with peaks at 3420 cm^{-1} and 3450 cm^{-1} may originate from free or weak H-bond N-H stretching vibration. However, it is also possible that these two bands correspond to a strongly H-bonded NH_2 asymmetric vibration or a free NH_2 symmetric vibration according to the frequency shift upon H-bonding. The very broad absorption band around 3340 cm^{-1} (FWHM of 45 cm^{-1}) consists of several overlapping bands. Strong H-bonded N-H or NH_2 symmetric stretching vibration could be responsible for these bands, as vibrational modes involved in strong H-bonds can broaden the absorption bands ranging from several wavenumber up to over 100 cm^{-1}.[193] At 3220 cm^{-1} and 3260 cm^{-1}, two more bands associated with H-bonded N-H or NH_2 symmetric stretching vibration are observed. The free carboxylic acid O-H stretching vibration is not observed (expected at about 3600 cm^{-1}), indicating it is either involved in a zwitterionic structure or a hydrogen-bonded canonical structure. The former interaction would result in a significant red shift below 3200 cm^{-1}. To assign the 3-dimensional structure of EGR, the measured spectrum is compared with DFT calculated spectra and results are shown in the Structural Assignment Section.

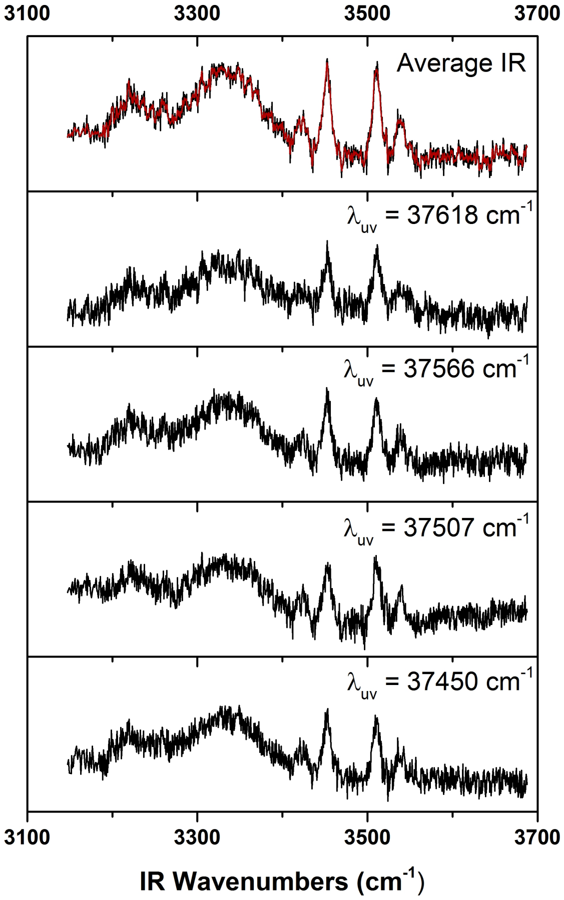

Figure 5.6: IR spectra of Z-Glu-Gly-Arg-NH_2 (EGR) acquired by IR-UV ion dip method with the UV wavelength at 37450 cm^{-1}, 37507 cm^{-1}, 37566 cm^{-1} and 37618 $^{-1}$, respectively. The top panel shows the original (black trace) and smoothed (red trace) average spectrum.

Z-Glu-Ala-Arg-NH_2 (EAR)

The average IR spectrum of EAR is shown in the middle panel of Figure 5.4. Identical IR spectra were obtained with the UV wavelengths fixed at the blue arrow labeled peaks in the REMPI spectrum (see Fig 5.7), demonstrating a single conformation present in the molecular beam. The IR spectra of EAR show several similar features to EGR. The bands above 3500 cm^{-1} originate from NH_2 asym-

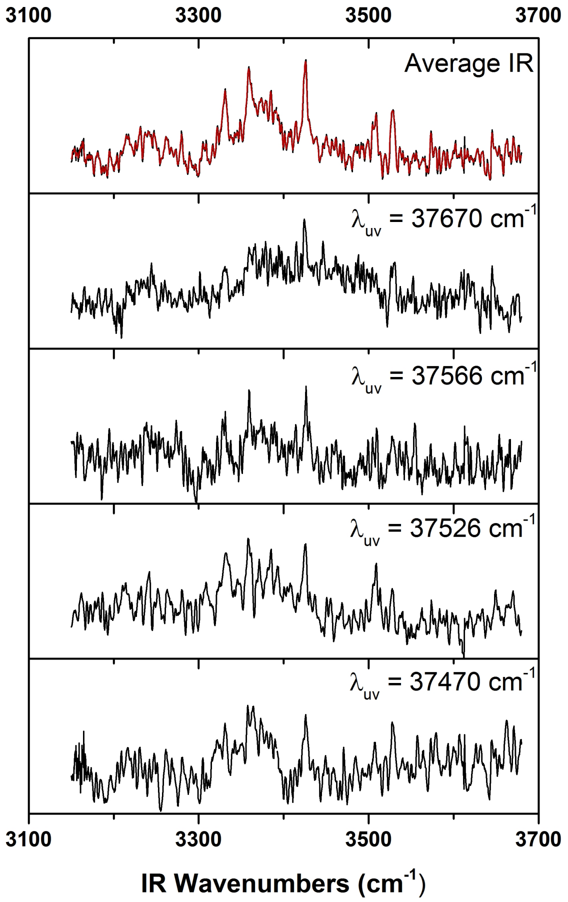

Figure 5.7: IR spectra of Z-Glu-Ala-Arg-NH_2 (EAR) acquired by IR-UV ion dip method with the UV wavelength at 37470 cm^{-1}, 37526 cm^{-1}, 37566 cm^{-1} and 37670 cm^{-1}, respectively. The top panel shows the original (black trace) and smoothed (red trace) average spectrum.

metric stretching vibration as was observed for EGR. In the region 3300-3450 cm^{-1}, there are also two intense bands with peaks at 3330 cm^{-1} and 3425 cm^{-1}, and a partially resolved broad band in between with peaks at 3360 cm^{-1}, 3373 cm^{-1} and 3392 cm^{-1}. These bands can be due to either N-H stretching vibration or NH_2 symmetric stretching vibration.

Z-Glu-Pro-Arg-NH_2 (EPR)

Also for EPR, we obtained identical IR spectra (see Fig. 5.8) for several different UV wavelengths in the REMPI spectrum. In the top panel of Fig. 5.4, the average

IR spectrum of EPR is presented. Where EGR and EAR show many similar bands, the IR spectrum of EPR is significantly different. Above 3500 cm^{-1}, there are three obvious bands, the peaks of which are 3506 cm^{-1}, 3527 cm^{-1} and 3577 cm^{-1}. Two (3506 cm^{-1} and 3527 cm^{-1}) of them can be assigned to NH_2 asymmetric stretching vibration while the peak at 3577 cm^{-1} may originate from either NH_2 asymmetric vibration or free carboxylic acid O-H vibration from Glu side chain. In the N-H free stretching region, an obvious band with peak 3476 cm^{-1} was observed and a weak absorption band with peak at 3458 cm^{-1} was also detected. Moreover,

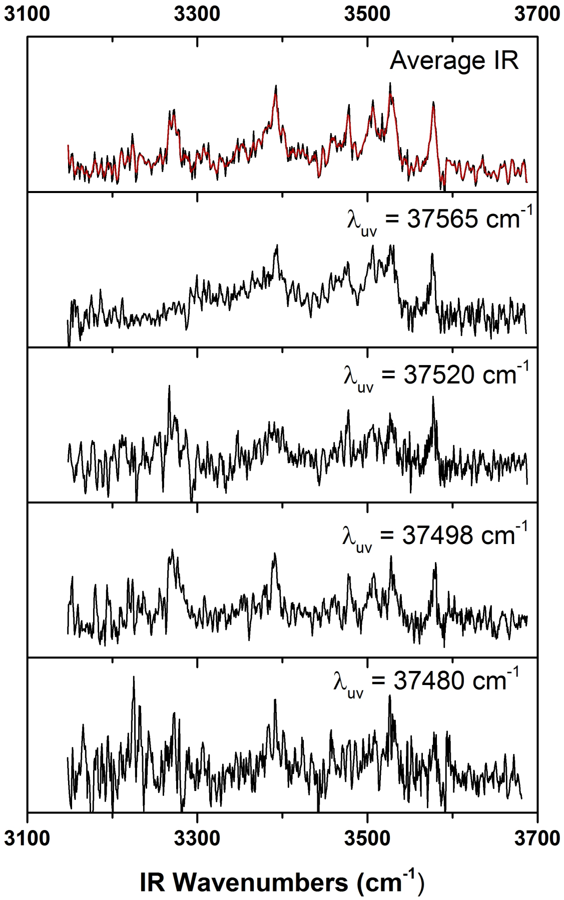

Figure 5.8: IR spectra of Z-Glu-Pro-Arg-NH_2 (EPR) acquired by IR-UV ion dip method with the UV wavelength at 37480 cm^{-1}, 37498 cm^{-1}, 37520 cm^{-1} and 37565 cm^{-1}, respectively. The top panel shows the original (black trace) and smoothed (red trace) average spectrum.

two broad bands with peaks at 3270 cm^{-1} and 3390 cm^{-1} can be associated with H-bonded N-H or NH_2 symmetric stretching vibration.

5.3.3 Structural assignment

Z-Glu-Ala-Arg-NH_2 (EAR)

In our previous study, structural assignment has already been done for the NHMe-capped EAR analogue (Z-Glu-Ala-Arg-NHMe) based on the comparison between measured IR spectra in the Amide I, II and fingerprint region (1000-1800 cm^{-1}) and DFT calculated spectra.[61] Therefore, the structural assignment for the peptides investigated here starts with EAR. Using the same approach as before, the input structures for the conformational search include three different families depending on the form of the Arg side chain: two non-zwitterionic types (see Fig. 5.1a and 5.1c) and one zwitterionic type with a deprotonated Glu and protonated Arg side chain (see Fig. 5.1b). 15 low-energy conformations from each type are optimized at the B97-D/6-31G(d,p) level of theory. Finally, based on the energy sequence of B97-D/6-31G(d,p) optimized structures and previous findings for Z-Glu-Ala-Arg-NHMe,[61] 10 low energy structures of the zwitterionic type and 6 low energy structures of the non-zwitterionic type (of which two converted to a zwitterionic structure in the structural optimization step) are further optimized and their vibrational frequencies are computed using B3LYP and B97-D functionals employed with the 6-311+G(d,p) basis set. From the obtained structures, 12 zwitterionic structures (abbreviated as Z), 2 canonical structures (abbreviated as C) and 1 tautomeric structure (abbreviated as T) are presented in Fig. 5.9. The relative energies and intramolecular interactions for structures optimized with B97D/6-311+G(d,p) level of theory are listed in Table 5.1.

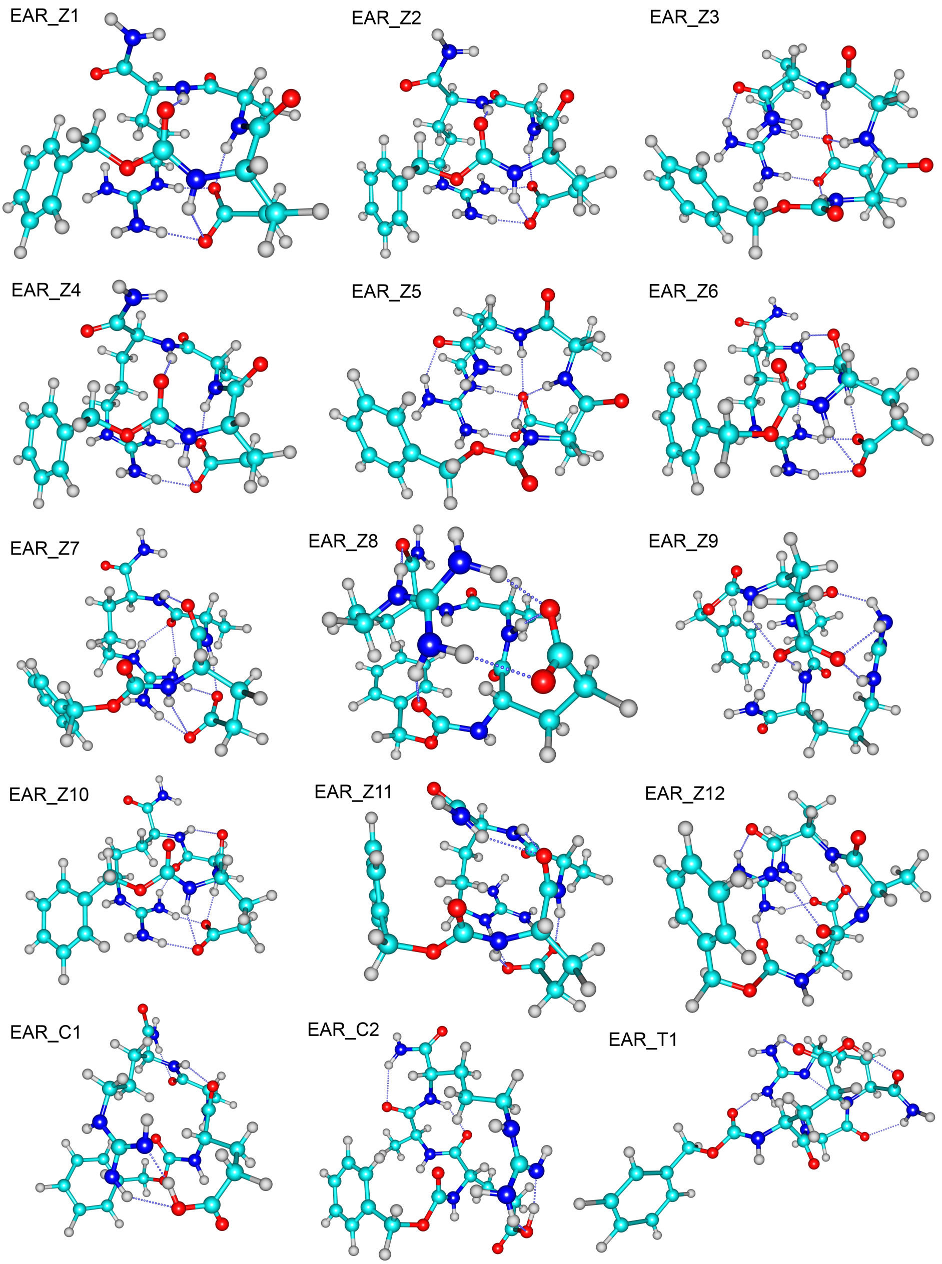

Figure 5.9: B97D/6-311+G(d,p) optimized conformational structures of Z-Glu-Ala-Arg-NH_2

Table 5.1: Relative energies and intramolecular interactions for the optimized structures of Z-Glu-Ala-Arg-NH_2 (Energies are given in kcal/mol, temperature equals to 0 Kelvin for ZPE and 300 Kelvin for Gibbs free energy).

	B97D		B3LYP		Interactions			
	ZPE	Gibbs	ZPE	Gibbs	SC - SC	Dis. Int.	BB - BB	BB - SC
EAR_Z1	0.00	0.00	0.00	0.00	A	$2N\eta H_2$	C_{10}(O0-N3)	N1-O^1 + N2-O^2
EAR_Z2	0.62	0.91	0.96	-0.24	B	$N\varepsilon H + N\eta H_2$	C_{10}(O0-N3)	N1-O^1 + N2-O^2
EAR_Z3	1.01	1.95	1.37	0.66	A	$2N\eta H_2 + NH_2$		N1-O^1 + N2-O^2 + N3-O^2 + O3-$H_2N\eta$
EAR_Z4	1.95	2.55	2.90	1.73	B	$N\varepsilon H + N\eta H_2$	C_{10}(O0-N3)	N1-O^1 + N2-O^2
EAR_Z5	2.68	2.71	1.67	0.90	A	$2N\eta H_2 + NH_2$	N1-O^1 + N2-O^1 + N3-O^1 + O3-$H_2N\eta$	
EAR_Z6	3.01	3.15	4.59	4.49	B	$N\varepsilon H + N\eta H_2$	C_7(O1-N3)	N1-O^1 + N2-O^2 + O2-$H_2N\eta$
EAR_Z7	5.01	4.68	3.33	2.26	B	$N\eta H_2$	C_7(O1-N3)	N1-O^1 + N2-O^2 + O2-$HN\varepsilon$ + O2-$H_2N\eta$
EAR_Z8	5.15	6.03	2.63	2.84	B			O0-$H_2N\eta$ + N2-O^1 + O3-$HN\varepsilon$
EAR_Z9	5.42	5.90	3.17	1.38	$C^\star$	N2		N1-O^1 + O1-$H_2N\eta$ + N3-O^1 + NH_2-O^1
EAR_Z10	5.66	4.87	4.41	3.69	B	$N\varepsilon H + N\eta H_2$	C_7(O1-N3)	N1-O^1 + N2-O^2 + O2-$H_2N\eta$
EAR_Z11	7.47	8.51	4.77	3.61	A		C_7(O1-N3) + C_{10}(O1-NH_2)	N1-O^1 + N2-O^2
EAR_Z12	7.79	8.70	5.69	6.30	$C^\star$	NH_2	C_{10}(O1-NH_2)	O0-$H_2N\eta 1$ + N2-O^1 + N3-O^1 + O3-$H_2N\eta 2$
EAR_C1	14.40	12.76	8.85	6.80	$N\eta H_2$-OH + OH-$N\eta H$	$N\varepsilon H + N\eta H_2$	C_7(O1-N3) + C_7(O2-NH_2)	
EAR_C2	15.24	13.79	9.76	7.28	$N\eta H_2$-OH + OH-$N\eta H$	N2	C_7(O1-N3) + C_7(O2-NH_2)	
EAR_T1	17.68	15.18	10.22	7.52	O-$H_2N\eta 1$		C7(O2-NH_2)	O0-$H_2N\eta 2$ + OH-O3 + N3H-$N\varepsilon$
EAR_T2	19.84	17.21	13.00	10.97			C7(O2-NH_2)	O0-$H_2N\eta 1$ + OH-O3 + N3H-$N\varepsilon$

Four types of salt bridge interactions (see Figure 5.10) are found for zwitterionic EAR. Two families (named type A and B, see Fig.5.10) show pairwise interactions, where both of the carboxylic oxygen atoms are involved in interactions with Arg side chain. The other two types are characterized by bifurcated interactions (C and C⋆ type). Here, only one carboxylic oxygen atom participates in interactions with the Arg side chain, while the other one is stabilized by the peptide backbone. For the optimized structures listed for EAR the pairwise interactions (type A and B) dominate the lowest energy structures, which was also found previously.[61] In addition to side chain involved salt bridge interactions, several backbone folds and backbone-side chain interactions are observed in the optimized structures (see Fig. 5.9).

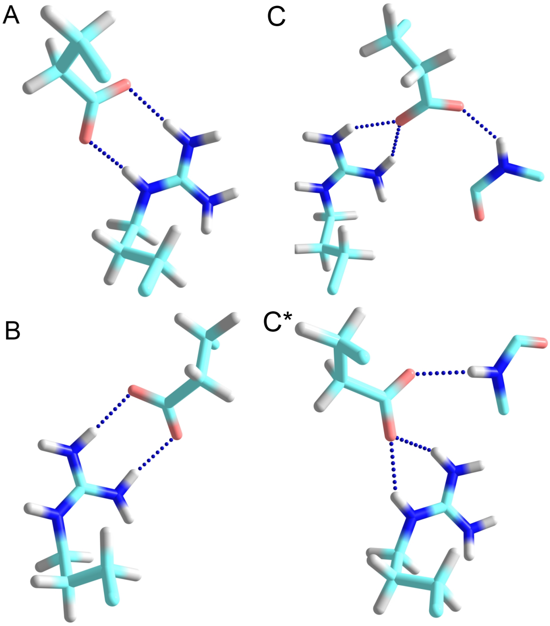

Figure 5.10: Four different types of salt bridge interactions found in the conformational search of zwitterionic EAR, EGR and EPR. Types A and B (left panel, top (A), and bottom (B)) are pairwise interactions, types C and C⋆ (right panel, top (C), and bottom (C⋆)) are bifurcated interactions.

Although many types of intramolecular interactions are present, due to the acidic Glu side chain and highly basic Arg side chain and the flexibility of the backbone, zwitterion formation dominates the folding interactions of EAR. As can be seen in Table 5.1, the structures showing proton transfer are indeed lower in relative energy, indicating that salt bridge interaction controls the structure of EAR. The first non-zwitterionic type (EAR_C1) appears 14.4 kcal/mol above the lowest energy zwitterionic structure. The canonical structures (see for example EAR_C1 and EAR_C2 of Figure 5.9) are governed by a hydrogen bond connecting the carboxylic acid OH group and the nitrogen lone pair of the NηH group of the Arg side chain, demonstrating the tendency to proton transfer. However, this H-bonding is not observed in the tautomeric structures, which is reflected directly in the higher relative energy (17.7 kcal/mol) of this family. Based on the relative energies it is not expected to observe non-zwitterionic structures in the experiment.

The experimentally observed conformer of the previously studied NHMe capped EAR (Z-Glu-Ala-Arg-NHMe) was assigned to the most stable zwitterionic structure with an A type salt bridge interaction.[61] However, the second lowest energy structure with a B type salt bridge interaction was suggested to coexist in the insufficient cooled molecular beam. Except for the orientation of the guanidine side chain of Arg, these two structures are almost identical, both in which a C_{10} backbone interaction, two dispersion interactions and two interactions between backbone NH groups and oxygen atoms of the Glu side chain are observed. As expected, the two most stable structures found in the conformational search for Z-Glu-Ala-Arg-NH_2 studied here shows exactly the same 3-dimentional shape as the structures assigned to Z-Glu-Ala-Arg-NHMe, in which EAR_Z1 includes A type salt bridge interaction while EAR_Z2 consists of B type interaction. Close examination of the other conformations with relative energies below 3 kcal/mol reveals that A type salt bridge interaction is also present in EAR_Z3 and EAR_Z5, which differ from EAR_Z1 only in the orientation of terminal Z-cap and NH_2 group. The B type interaction was found in EAR_Z4 and EAR_Z6, with very similar 3-dimentional structures as EAR_Z2. Although the non-zwitterionic structures are energetically much less stable compared with zwitterionic structures and therefore less likely to exist under our experimental conditions, we can not exclude them only based on energetics alone. Therefore, we have compared our experimental spectra against a wide set of zwitterionic, but also tautomeric and canocical structures of which the calculated IR spectra of the 6 lowest energy structures together with the two lowest energy canonical structure (EAR_C1, C2) and tautomeric structure (EAR_T1, T2) are shown in Fig. 5.11.

Non-zwitterionic structures are not expected to be observed experimentally based on their relative energies. Inspection of the calculated IR spectra of these structures (Fig. 5.11) verifies this assumption. The spectra of both EAR_C1 and EAR_C2 as well as those from other canonical structures either present much less bands than experimentally detected in the 3350-3400 cm^{-1} range, or show several absorptions between 3440 cm^{-1} and 3480 cm^{-1}, which are not observed in the experimental spectrum. For tautomeric isomers, the calculated spectra show a very intense absorption below 3200 cm^{-1} which is not observed experimentally. Other mismatches can be found as well for instance the measured absorption

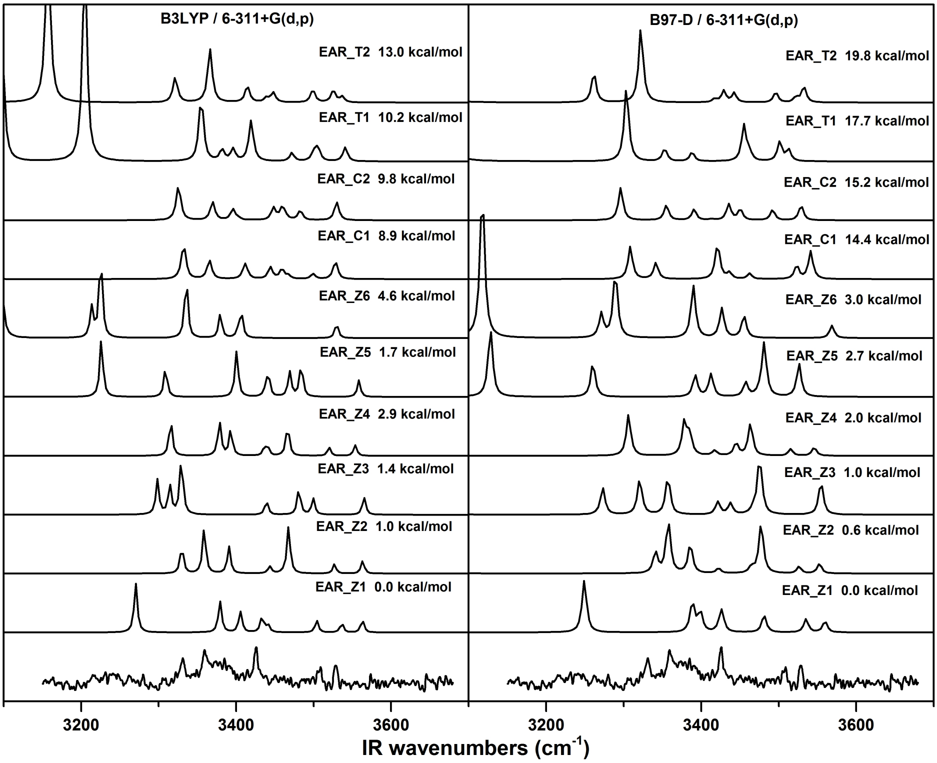

Figure 5.11: Experimental spectrum of Z-Glu-Ala-Arg-NH_2 (bottom trace) and theoretical spectra of six lowest energy zwitterionic structures EAR_Z1-Z6, two canonical structure EAR_C1,C2 and two tautomeric structure EAR_T1, T2. The theoretical spectra are calculated at the B3LYP/6-311+G(d,p)(left panel) and B97-D/6-311+G(d,p)(right panel) level of theory, of which the frequencies are scaled by a factor of 0.960 and 0.977, respectively to account for anharmonicity.

at 3330 cm^{-1} is absent in spectrum of EAR_T1 while the spectrum of EAR_T2 misses the broad absorption band covering 3350-3400 cm^{-1}. As a result, we can conclude that EAR indeed forms a zwitterionic interaction. The question remains what type of salt bridge is formed. Although B97-D functional might improve the accuracy of calculated frequency of a vibrational mode in dispersion interaction, previous work shows that B3LYP functional works better in spectra computation in mid-infrared region.[42;151;163] Therefore, the structural assignment in this paper is mainly based on calculations using B3LYP functional.

At first glance, none of the calculated spectra matches perfectly with the experimental IR spectrum. For example, the calculated spectrum of EAR_Z3 shows three intense absorption bands around 3300 cm^{-1}, but the experiment shows strong activity at higher energies namely between 3325-3425 cm^{-1}. Therefore, EAR_Z3 is excluded as the candidate for the assigned structure. The same holds for EAR_Z5, which is almost identical to EAR_Z3, since its calculated IR spectrum shows several obvious mismatches to the experimental spectrum. Conformers EAR_Z4 and EAR_Z6, which only differ in the orientation of the guanidine side chain of Arg with respect to the lower energy structure EAR_Z2 are expected to convert to EAR_Z2 in the supersonic cooling if the barrier is low.[163] Moreover, their calculated spectra do not match the experimental one as good as EAR_Z2.

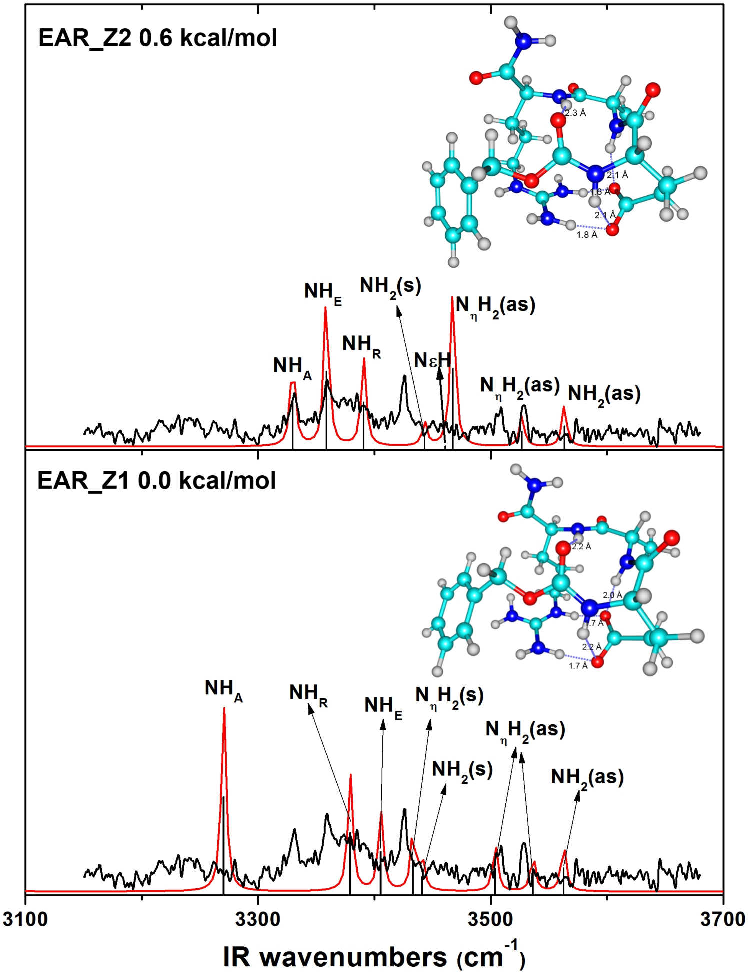

Figure 5.12: IR absorption spectra of EAR (black trace) and theoretical spectra of two lowest energy structures (red trace with black bars underneath presenting the peaks of labeled vibrational modes) in the amide A region (3150 - 3700 cm^{-1}).

The calculated spectrum of the two lowest energy structures, EAR_Z1 and EAR_Z2, are shown in Figure 5.12. Considering the minor difference in the 3-dimentional structures of EAR_Z1 and EAR_Z2, only in the character of the Glu-Arg salt bridge, their calculated spectra should show several similarities. Indeed, the asymmetric stretching vibration and symmetric stretching vibration of the NH_2 cap are found at 3560 cm^{-1} and 3440 cm^{-1} respectively for both EAR_Z1 and EAR_Z2. Although the backbone of EAR_Z1 and EAR_Z2 experiences the same interactions (see Figure 5.13), the small difference in structure due to the different salt bridge types results in significant shifts of the NH backbone vibrations. For example, the difference in H-bond length between the NH group of the Ala residue and the carboxyl oxygen atom which is 2.0 Å in EAR_Z1 and 2.1 Å in EAR_Z2, results in a red shift of the NH_A (Ala) stretching vibration from 3330 cm^{-1} in EAR_Z2 to 3270 cm^{-1} in EAR_Z1. The same holds for the frequency difference of the NH_E (Glu) and NH_R (Arg) vibration: 3400 cm^{-1} in EAR_Z1 (2.2 Å H-bond) vs 3360 cm^{-1} in EAR_Z2 (2.1 Å H-bond) for NH_E, and 3380 cm^{-1} in EAR_Z1 (2.2 Å H-bond) vs 3390 cm^{-1} in EAR_Z2 (2.3 Å H-bond) for NH_R.

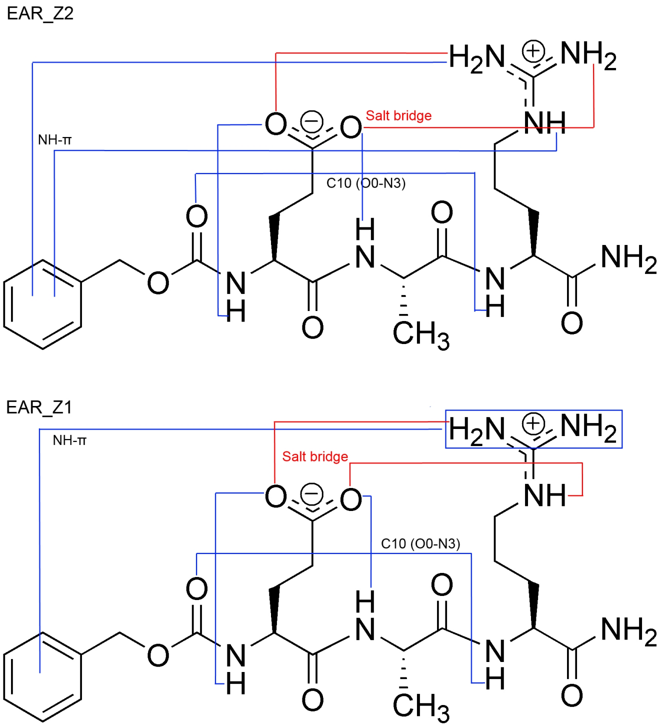

Figure 5.13: Intramolecular interactions in theoretical optimized structures EAR_Z1 and Z2

In the previous study on the NHMe-capped analogues, Jaeqx *et al.* suggested that these two structures coexist in the molecular beam.[61] The same conclusion applies for the NH_2-capped EAR studied in this paper. As the bottom panel of Figure 5.12 suggests, the experimental IR spectrum can be assigned to an A type zwitterionic structure (EAR_Z1) based on the NH/NH_2 vibrations resulting from the guanidine side chain of Arg observed above 3425 cm^{-1}. The backbone of EAR folds into a beta turn via a C_{10} interaction. Although this is observed in the same fashion for both EAR_Z1 and EAR_Z2, the exact orientation follows the folding pattern of EAR_Z2.

Z-Glu-Gly-Arg-NH_2 (EGR)

Similar as described in the previous section, an elaborate conformational search was also performed for EGR. The energies and intramolecular interactions of several lowest energy conformations are shown in Table 5.2. The structures and calculated IR spectra are presented in Fig. 5.14 and 5.15.

As was observed for EAR, the lowest non-zwitterionic structure for EGR also lies 15.4 kcal/mol higher in energy than the lowest energy structure with proton transfer, indicating that structures observed in the gas-phase measurements of EGR can be addressed as zwitterionic ones. Among the zwitterionic structures, we have found within relative energies of 6 kcal/mol, the previous observed pairwise salt bridge interactions (A and B type, see Figure 5.10), but also two families of bifurcated interactions (named C and $C^{\star}$ type). The C type bifurcated interaction appears only above 5.8 kcal/mol. The higher flexibility of the Gly residue than that of the Ala residue and the reduced steric hindrance results in more intramolecular interactions in the lowest energy structure found for EGR than EAR. All the calculated structures show multiple backbone folds and backbone-side chain interactions that together with the Glu-Arg salt bridge contribute to the overall conformational fold. Moreover, a large number of stable structures are found for EGR within 2 kcal/mol with respect to the lowest energy structure (see Table 5.2).

Based on the computed energies, observing non-zwitterionic structures for EGR is not expected experimentally. Inspection of the computed spectra of the canonical and tautomeric structures (see Fig. 5.15) reveals that none of these structures is responsible for the experimental IR spectrum as the experimentally found absorption bands at 3220 cm^{-1} and/or 3260 cm^{-1} are absent in the calculated spectra. Besides EGR_C1, C2 and EGR_T1, T2, also EGR_Z1, Z4, Z5, Z7 and Z8 do not show any vibrational activity in 3200-3300 cm^{-1}, where the strongly hydrogen bonded NH_2 (symmetric) and NH backbone vibrations are expected. Hence, it is unlikely that the observed IR spectrum of EGR results from any of them.

Table 5.2: Relative energies and intramolecular interactions for the optimized structures of Z-Glu-Gly-Arg-NH_2 (Energies are given in kcal/mol, temperature equals to 0 Kelvin for ZPE and 300 Kelvin for Gibbs free energy).

	B97D		B3LYP		Interactions			
	ZPE	Gibbs	ZPE	Gibbs	SC - SC	Dis. Int.	BB - BB	BB - SC
EGR_Z1	0.00	0.30	1.71	2.12	B	$N\varepsilon H$	C_5(N1-O1) + C_7(O1-N3) + C_7(O2-NH_2)	O0-$H_2N\eta$ + N2-O^1
EGR_Z2	0.07	0.25	1.72	0.41	$C^\star$	N2		N1-O^1 + O1-$H_2N\eta$ + N3-O^1 + NH_2-O^1
EGR_Z3	0.09	0.00	2.38	3.12	A	$2N\eta H_2$	C_{10}(O0-N3)	N1-O^1 + N2-O^2
EGR_Z4	0.26	0.20	3.23	3.09	B	$N\varepsilon H + N\eta H_2$	C_{10}(O0-N3)	N1-O^1 + N2-O^2
EGR_Z5	1.59	1.40	1.67	1.46	A	$2N\eta H_2$		N1-O^1 + N2-O^2 + N3-O^2 + O3-$H_2N\eta$
EGR_Z6	1.66	2.37	1.74	0.79	$C^\star$	N2		N1-O^1 + O1-$H_2N\eta$ + N3-O^1 + NH_2-O1
EGR_Z7	1.92	2.00	0.00	0.00	A	$2N\eta H_2$	C_7(O0-N2) + C_7(O2-NH_2)	N1-O^1
EGR_Z8	3.65	3.42	7.62	8.55	B	$N\varepsilon H + N\eta H_2$	C_7(O1-N3)	N1-O^1 + N2-O^2 + O2-H2Nη
EGR_Z9	5.14	5.99	4.83	5.30	B	$N\varepsilon H + N\eta H_2$	C_{10}(O0-N3) + C_{10}(O1-NH_2)	N2-O^1
EGR_Z10	5.78	4.56	4.76	4.21	C	$N\varepsilon H$	C_5(N1-O1) + C_7(O2-NH_2)	O0-$H_2N\eta$ + N2-O^1
EGR_Z11	5.95	4.97	1.93	0.73	$C^\star$			N1-O^1 + O1-$H_2N\eta$ + N3-O^1 + NH_2-O^1
EGR_Z12	7.70	6.59	6.28	5.33	B	$N\varepsilon H + N\eta H_2$	C_7(O1-N3) + C_7(O2-NH_2)	
EGR_Z13	7.77	5.49	4.07	3.58	C			O0-$H_2N\eta$ + N2-O^1 + N3-O^1 + NH_2-O^1 + O3-HNε
EGR_Z14	8.59	6.43	4.93	4.03	C		C_5(N1-O1)	O0-$H_2N\eta$ + O0-HNε + N2-O^1 + N3-O^1 + O1-$H_2N\eta$
EGR_C1	15.35	13.08	20.57	24.42	O-H_2N	NH_2	C_7(O0-N2) + C_7(O1-N3)	N1H-Nε + O3-HNη
EGR_C2	15.87	14.12	13.06	10.85	OH-NηH	$N\eta H_2$	C_7(O0-N2) + C_7(O1-N3)	O0-$H_2N\eta$
EGR_T1	18.10	16.13	16.36	20.03	O-$H_2N\eta$1	N2		N1H-OH + OH-O3 + O1-$H_2N\eta$2 + N3-Nε
EGR_T2	18.74	17.65	19.18	16.53		$N\eta H_2$	C7(O2-NH_2)	O0-HO + N1-Nε + N3-Nε

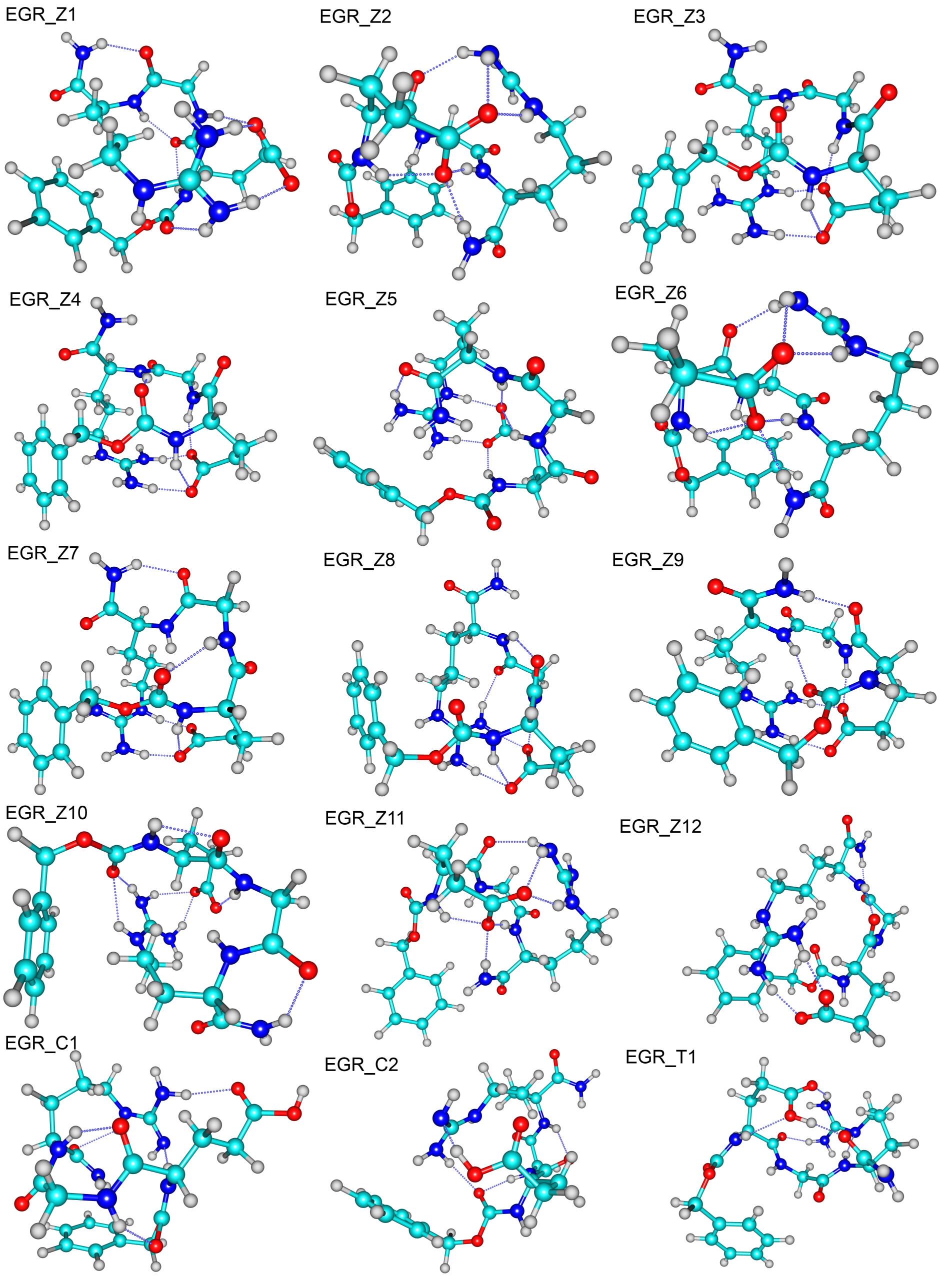

Figure 5.14: B97D/6-311+G(d,p) optimized conformational structures of Z-Glu-Gly-Arg-NH_2

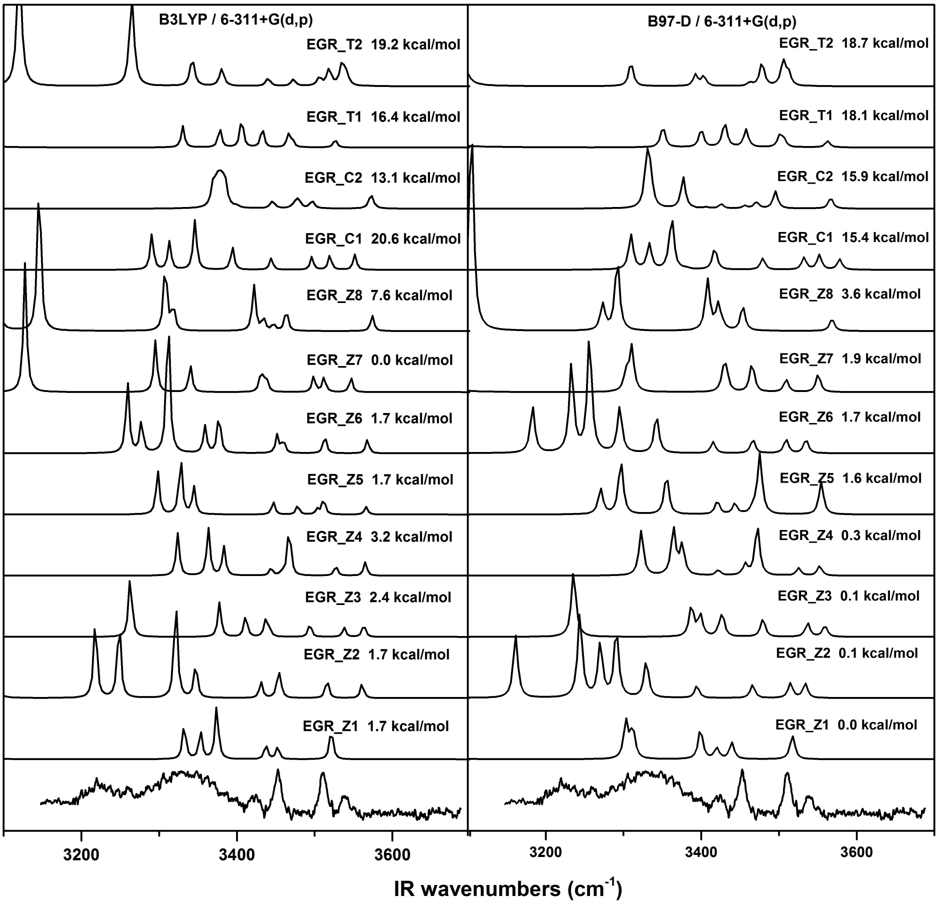

Figure 5.15: Experimental IR spectrum of Z-Glu-Gly-Arg-NH_2 (bottom trace) and theoretical spectra of eight lowest energy zwitterionic structures EGR_Z1-Z8, two canonical structures EGR_C1, C2 and two tautomeric structure EGR_T1, T2. The theoretical spectra are calculated at the B3LYP/6-311+G(d,p) (left panel) and B97-D/6-311+G(d,p) (right panel) level of theory, of which the frequencies are scaled by a factor of 0.960 and 0.977, respectively to account for anharmonicity.

The three remaining structures, EGR_Z2, EGR_Z3 and EGR_Z6 are presented in Figure 5.16. Since the relative energies of EGR_Z1, Z2, Z3 and Z4, ranging from 0 kcal/mol for EGR_Z1 to 0.3 kcal/mol for EGR_Z4, lie all within the accuracy of the energies in DFT calculation (about 1 kcal/mol), any of the four structures could be considered as the most stable one. The second lowest energy structure, EGR_Z2, shows a reasonably good match with the experimental spectrum. The absorption bands above 3500 cm^{-1} can be attributed to asymmetric stretching

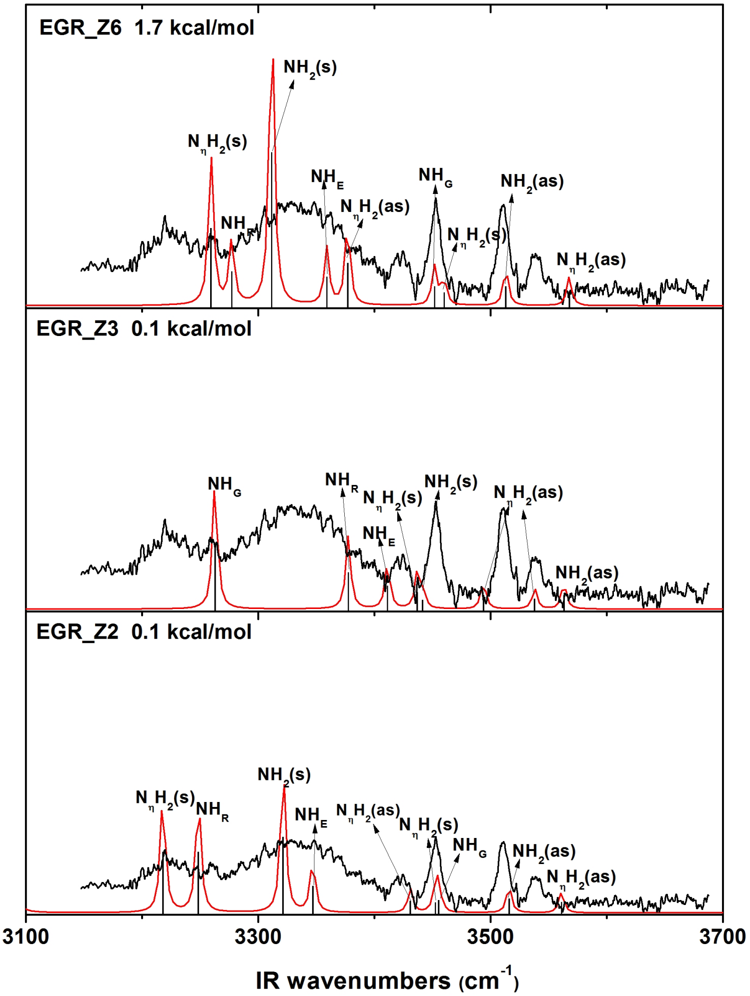

Figure 5.16: IR absorption spectra of EGR (black trace) and theoretical spectra of EGR_Z2, Z3 and Z6 (red trace with black bars underneath presenting the peaks of labeled vibrational modes) in the amide A region (3150 - 3700 cm^{-1})

vibrations of NH$_2$ groups, of which one is unperturbed from the Arg side chain (3560 cm^{-1}), while the other peak is the H-bonded C-terminal cap (3520 cm^{-1}). The vibrational modes of the free NH group of the Gly residue and the guanidine NH$_2$ symmetric stretching overlap with each other and account for the experimental detected band at 3450 cm^{-1}. Besides, the less intense band measured at 3420 cm^{-1} may originate from asymmetric stretching vibration of the guanidine NH$_2$ group which participates in the salt bridge interaction. Below 3400 cm^{-1}, the very broad band with two peaks at 3330 cm^{-1} and 3350 cm^{-1} is associated with symmetric stretching vibration of C-terminal NH_2 and H-bonded NH group vibration from Glu residue. Both of the two groups are H-bonded to the carbonyl oxygen of Glu side chain and form 7-membered rings, which may explain why the corresponding measured absorption band is so broad. In addition, the absorptions at 3220 cm^{-1} and 3260 cm^{-1} can be attributed to the vibrations of guanidine NH_2 group and Arg backbone NH group, which is involved in salt bridge and H-bond, respectively.

Although structure EGR_Z2 matches the experimental spectrum very well, the relative intensity of peaks do not coincide in the hydrogen bonded region below 3400 cm^{-1}. The intense hydrogen bond interactions do not only lead to a red shift of the observed frequencies, but also broaden the experimentally observed absorption bands. Considering both the computed energetics and peak positions in the IR spectrum, the experimental spectrum of Z-Glu-Gly-Arg-NH_2 is assigned to the zwitterionic EGR_Z2 with a bifurcated salt bridge interaction ($C^\star$ type).

Z-Glu-Pro-Arg-NH_2 (EPR)

The presence of the proline residue in the peptide chain allows both the trans orientation as well as the cis orientation of the peptide bond, which is normally energetically unfavorable due to steric repulsion.[194] Therefore, both isomers are considered in the conformational search for EPR. Table 5.3 presents the relative energies and intramolecular interactions of optimized structures together with the type of Glu-Arg interaction and the orientation of the proline peptide bond (trans or cis). Although the lowest energy structure adopts the trans type, 14 out of 20 selected structures here show a cis prolyl peptide bond. This indicates that structures with a cis peptide bond are as stable as trans isomers and should be included in the conformational search.

Examining the computed energies, it can be seen that proton transfer from the side chain of Glu to that of Arg is still the favorable conformation, although the first structure in non-zwitterionic structure appears at significant lower energies (6.5 kcal/mol) compared to EAG and EGR (where the canonical structure was found at 14.4 kcal/mol and 15.4 kcal/mol, respectively). These low energy canonical structures of EPR show intense H-bond interactions between the Glu side chain (carboxyl OH group) and Arg side chain ($N\eta H$).

Table 5.3: Relative energies and intramolecular interactions for the optimized structures of Z-Glu-Pro-Arg-NH$_2$ (Energies are given in kcal/mol, temperature equals to 0 Kelvin for ZPE and 300 Kelvin for Gibbs free energy).

	B97D		B3LYP		Interactions			
	ZPE	Gibbs	ZPE	Gibbs	SC - SC	Dis. Int.	BB - BB	BB - SC
EP$_{trans}$R_Z1	0.00	0.00	0.00	0.00	A	2NηH$_2$	C$_7$(O1-N3) + C$_7$(O2-NH$_2$)	N1-O^1
EP$_{cis}$R_Z2	0.29	0.81	3.07	4.67	A	2NηH$_2$		N1-O^1 + O3-H$_2$Nη
EP$_{cis}$R_Z3	1.82	0.65	2.29	1.52	C	NεH + NηH$_2$	C$_5$(O1-N1) + C$_7$(O2-NH$_2$)	N3-O^1 + O0-H$_2$Nη
EP$_{trans}$R_Z4	2.00	-1.00	0.88	-1.21	A		C$_{10}$(O1-NH$_2$)	N3-O^1 + O3-H$_2$Nη
EP$_{cis}$R_Z5	2.27	1.72	4.34	4.11	C*	2NηH$_2$	C$_5$(O1-N1) + C$_7$(O2-NH$_2$)	N3-O^1 + O3-H$_2$Nη
EP$_{cis}$R_Z6	3.65	3.27	4.29	4.27	C*	2NηH$_2$	C$_5$(O1-N1) + C$_7$(O2-NH$_2$)	O0-H$_2$Nη + N3-O^1
EP$_{trans}$R_Z7	4.11	3.48	2.59	1.49	A	2NηH$_2$	C$_7$(O1-N3) + C$_7$(O2-NH$_2$	N1-O^1
EP$_{cis}$R_Z8	4.36	3.98	6.36	6.34	O^1-H$_2$Nη_1		C$_5$(O1-N1)	O0-HNε + O^2-N3 + O^2-H$_2$N + O3-H$_2$Nη
EP$_{cis}$R_Z9	4.61	4.33	9.08	9.06	B	NεH + NηH$_2$		N1-O^1 + O^2-H$_2$N + O2-H$_2$Nη + O2-HNε
EP$_{cis}$R_Z10	4.69	4.36	7.95	8.34	A	2NηH$_2$	C$_5$(O1-N1) + C$_7$(O2-NH$_2$)	N3-O^1 + O3-H$_2$Nη
EP$_{trans}$R_11	4.92	4.43	7.19	6.62	B	NεH + NηH$_2$	C$_7$(O1-N3) + C$_7$(O2-NH$_2$	
EP$_{cis}$R_Z12	5.07	3.06	3.79	1.78	A	NH$_2$	C$_{10}$(O0-N3)	
EP$_{trans}$R_Z13	5.67	5.25	6.97	6.20	A	2NηH$_2$	C$_7$(O1-N3)	N1-O^1 + O3-H$_2$Nη
EP$_{cis}$R_C1	6.47	3.66	1.92	-0.42	OH-NÎů		C$_5$(O1-N1) + C$_7$(O2-NH$_2$)	N3-O$_1$ + O0-Nε
EP$_{cis}$R_Z14	7.28	4.53	2.71	2.81	C		C$_5$(O1-N1) + C$_7$(O2-NH$_2$)	O0-H$_2$Nη + N3-O$_2$
EP$_{cis}$R_Z15	7.32	5.37	1.52	0.48	C*		C$_5$(O1-N1) + C$_7$(O2-NH$_2$)	O0-H$_2$Nη + N3-O$_2$
EP$_{cis}$R_Z16	7.46	6.42	7.88	6.75	C		C$_5$(O1-N1) + C$_7$(O2-NH$_2$)	O0-H$_2$Nη + N3-O$_2$ + O3-Nε
EP$_{cis}$R_T1	7.75	5.49	11.77	9.98		2NηH$_2$	C$_5$(O1-N1) + C$_{13}$(O0-NH$_2$)	O1-H$_2$Nη_1 + N3-Nε + O3-H$_2$Nη_2
EP$_{trans}$R_C2	10.47	10.46	13.95	12.82	OH-Nη		C$_{10}$(O0-N3) + C$_7$(O2-NH$_2$)	O1-H$_2$Nη
EP$_{cis}$R_T2	11.23	8.58	12.93	10.10		2NηH$_2$	C$_5$(O1-N1) + C$_{13}$(O0-NH$_2$)	O1-H$_2$Nη_1 + N3-Nε + O3-H$_2$Nη_2

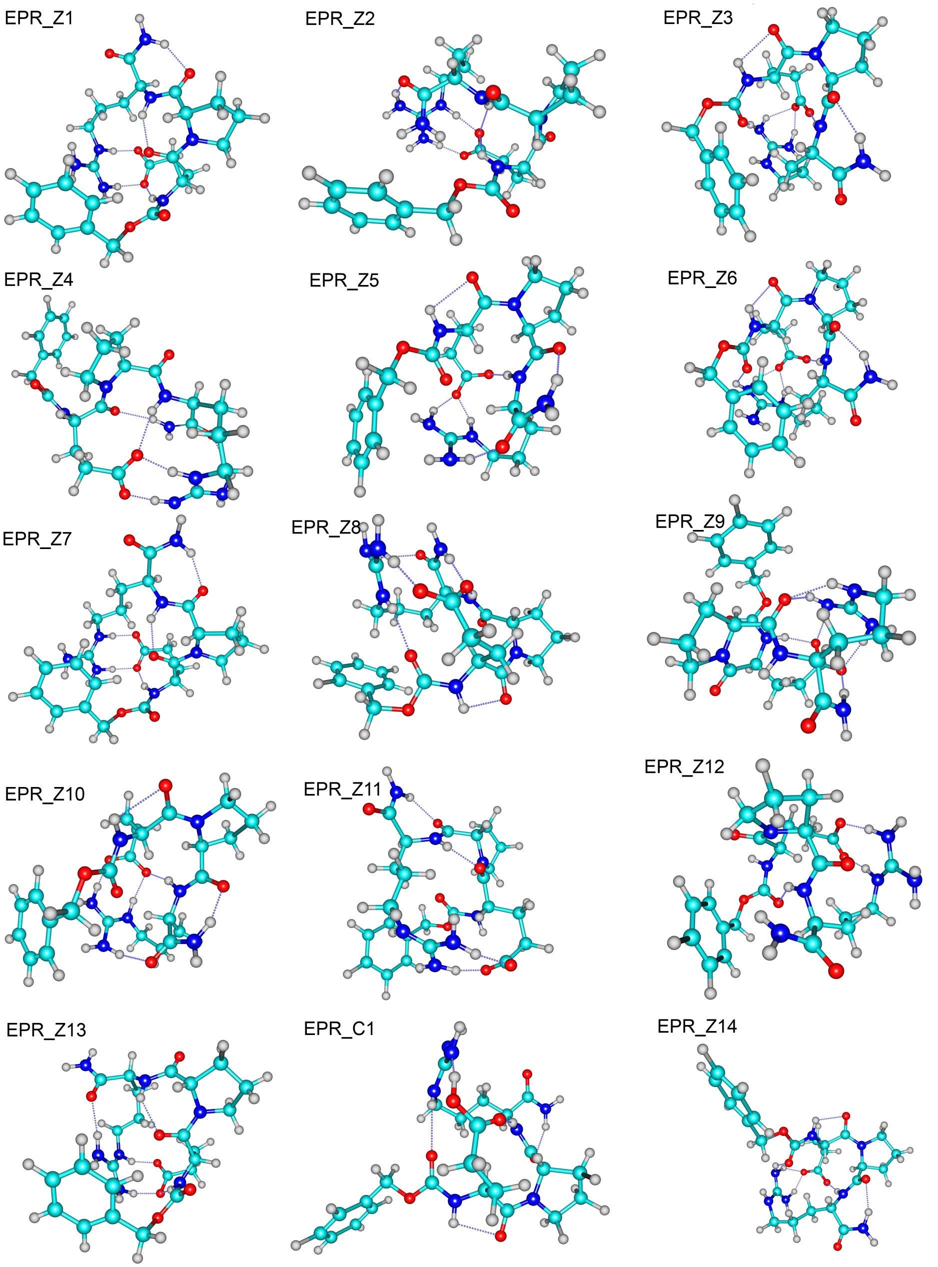

Figure 5.17: B97D/6-311+G(d,p) optimized conformational structures of Z-Glu-Pro-Arg-NH_2 (part 1)

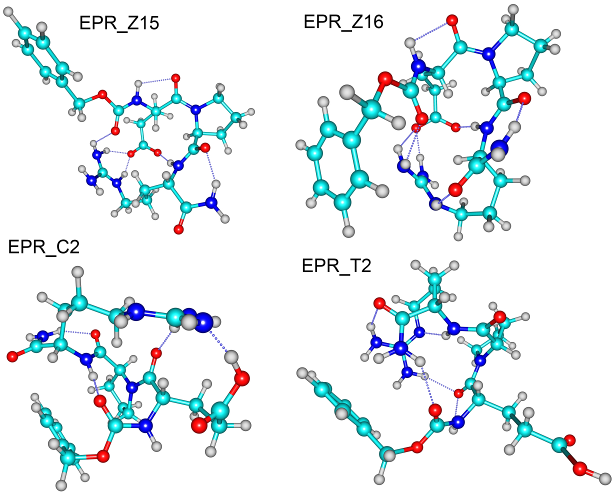

Figure 5.17: B97D/6-311+G(d,p) optimized conformational structures of Z-Glu-Pro-Arg-NH_2 (part 2)

In the 16 optimized zwitterionic structures (see Fig. 5.17 (part1)), the paired A type salt bridge interaction was observed seven times, including the two most stable structures EPR_Z1 and EPR_Z2. Two structures with B-type interaction are found, but at relatively high energies (4.6 kcal/mol and 4.9 kcal/mol). The bifurcated C type interaction and $C^\star$-type interaction are observed in three structures. Interestingly, it is worthy to mention that the C_7 H-bond, formed between peptide C=O group of Pro residue and C-terminal NH_2 group, was observed in 10 zwitterionic structures, while the C_5 H-bond between backbone NH group and C=O group of Glu residue appeared 8 times, indicating the importance of these two backbone H-bonds in the structural stability of EPR.

The calculated spectra of the optimized structures are shown in Fig. 5.18. Surprisingly, none of the theoretical spectra gives a very good match to the experimental spectrum, although we have evaluated a large number of possible structures. For instance, the band around 3580 cm^{-1} is missing in most of the calculated spectra, except for cases of EPR_Z12 and EPR_Z15, resulting from the free NH_2 group of the C terminus cap. The non-zwitterionic structures EPR_T1 and EPR_T2 show a peak at even higher wavenumbers (above 3600 cm^{-1}) as a result of - the indicative free carboxyl group for the tautomeric structure. The structures with a $C^\star$ type salt bridge interaction (EPR_Z5 and EPR_Z6) can be excluded as they show intense absorptions around 3200 cm^{-1}, which is not observed experimentally. The same holds for structures EPR_Z7, Z8, Z9, Z10, Z14 and Z16. To complete the assignment the IR-UV ion dip spectrum of EPR is measured in the 1000-1800 cm^{-1} region using the free electron laser FELIX, see the left panel of Figure 5.19.

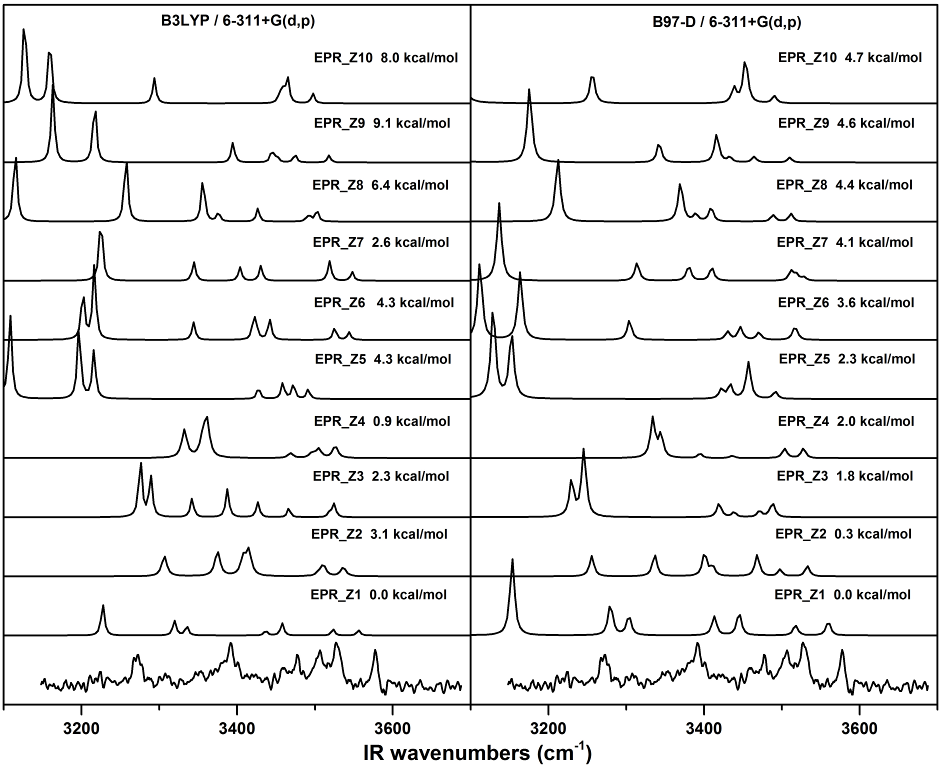

Figure 5.18: Experimental IR spectrum of Z-Glu-Pro-Arg-NH$_2$ (bottom trace) and theoretical spectra of ten lowest energy zwitterionic structures EPR_Z1-Z10. The theoretical spectra are calculated at the B3LYP/6-311+G(d,p) (left panel) and B97-D/6-311+G(d,p) (right panel) level of theory, of which the frequencies are scaled by a factor of 0.960 and 0.977, respectively to account for anharmonicity(Part 1).

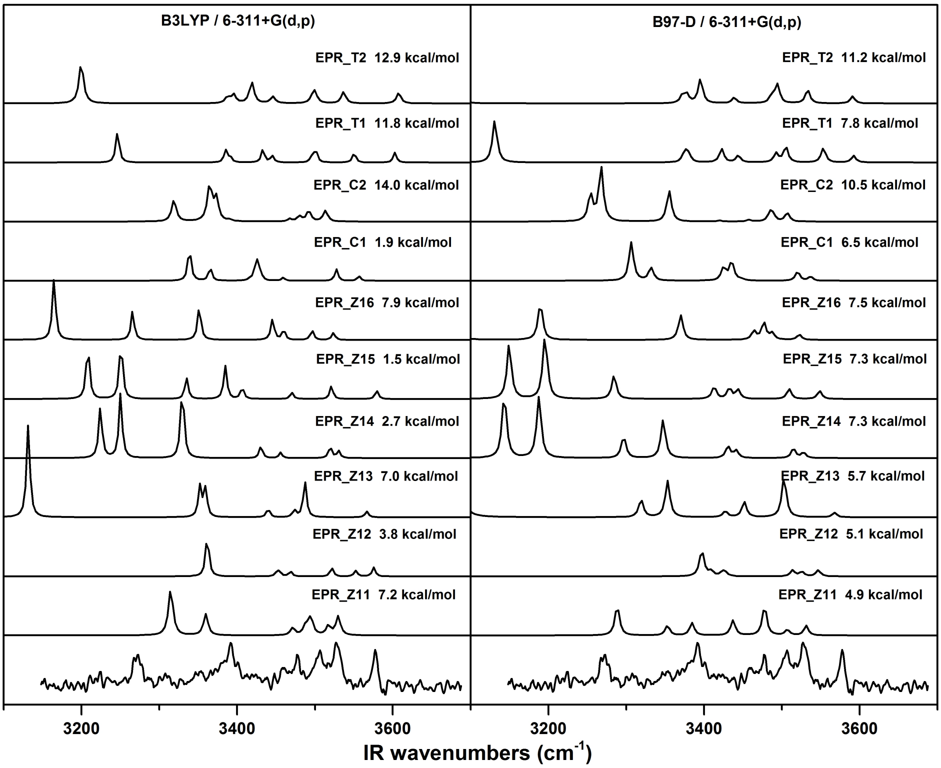

Figure 5.18: Experimental IR spectrum of Z-Glu-Pro-Arg-NH$_2$ (bottom trace) and theoretical spectra of zwitterionic structures EPR_Z11-Z16, two canonical structures EPR_C1, C2 and two tautomeric structure EPR_T1, T2. The theoretical spectra are calculated at the B3LYP/6-311+G(d,p) (left panel) and B97-D/6-311+G(d,p) (right panel) level of theory, of which the frequencies are scaled by a factor of 0.960 and 0.977, respectively to account for anharmonicity (Part 2).

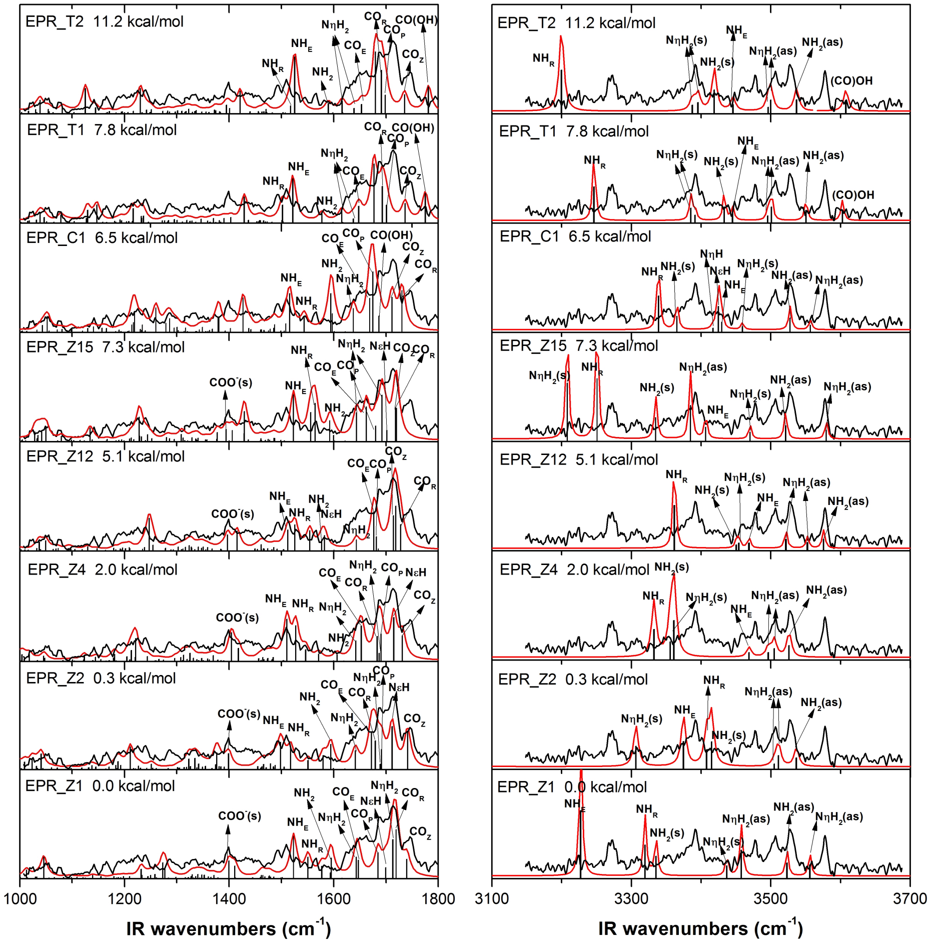

Figure 5.19: IR absorption spectra of EPR (black trace) and theoretical spectra of EPR_Z1, Z2, Z4, Z12, Z15, C1, T1 and T2 (red trace with black bars underneath presenting the peaks of labeled vibrational modes) in both the amide I, II and fingerprint region (1000 - 1800 cm^{-1}) as well as in the amide A region (3150 - 3700 cm^{-1})

The IR spectrum in this mid-infrared region provides information on the C=O stretch (Amide I, around 1700 cm^{-1}), NH bend (Amide II, around 1500 cm^{-1}) and fingerprint vibrations (1000-1400 cm^{-1}). Spectral congestion in combination with the limited resolution of the free electron laser in this wavelength region (typically 1%) results in unresolved bands in the IR spectrum in the Amide I and II region. The calculated spectra of not-excluded zwitterionic structures (EPR_Z1, Z2, Z4, Z12 and Z15) together with the non-zwitterionic structures (EPR_T1 and T2) are presented as red curves in Fig. 5.19. The tautomeric conformers, which exhibit a free carboxyl group, show a band around 1780 cm^{-1}, which is not experimentally observed. The absence of both the free OH as well as the free C=O in combination with the relatively high energies (above 7.8 kcal/mol) indicates that the structures EPR_T1 and EPR_T2 can be excluded from the structural assignment.

The IR spectra of the zwitterionic structures EPR_Z1, EPR_Z2, and EPR_Z4 structures all reproduce the main bands in the measured spectrum very well. The spectra show multiple diagnostic bands for the presence of the zwitterionic structure, for example, the band observed at around 1400 cm^{-1} can be assigned to the symmetric COO^- stretch vibration resulting from proton transfer from the carboxylic acid group of the Glu side chain to the Arg side chain guanidine group. EPR_Z1, EPR_Z2, and EPR_Z4 all have the A type paired Glu-Arg interaction, but they differ in the backbone fold. The backbone of EPR_Z1 folds into two successive gamma turns (C_7 interaction), EPR_Z4 into a beta turn (C_{10} interaction) and EPR_Z2 does not exhibit a specific backbone fold and its structure is governed by side chain - backbone and side chain-side chain interactions (see Figure 5.20). These different folding patterns result into small differences in the IR spectrum; the free carboxylic C=O of the Z-cap (CO_Z) which can be found at 1740 cm^{-1} for EPR_Z1 and EPR_Z2 is slightly red shifted for EPR_Z4. On the other hand, EPR_Z1 and EPR_Z2 show a strong band at 1595 cm^{-1} that is not observed experimentally.

The small differences in both the 1000-1800 cm^{-1} spectrum as well as the better agreement in the Amide A region, especially for the bands above 3400 cm^{-1} originating from the guanidine group, results in the assignment of Z-Glu-Pro-Arg-NH_2 to the EPR_Z4 conformer, exhibiting an A type salt bridge interaction, a C_{10} backbone H-bond and a H-bond between backbone C=O and Arg side chain. The zero-point energy of EPR_Z4 is 2.0 kcal/mol higher than the most stable structure, but its Gibbs free energy is -1.0 kcal/mol lower, indicating that it is the most stable one at room temperature. Considering the limited cooling of EPR in the supersonic expansion, it is fairly reasonable that population of EPR_Z4 dominates in our measurement.

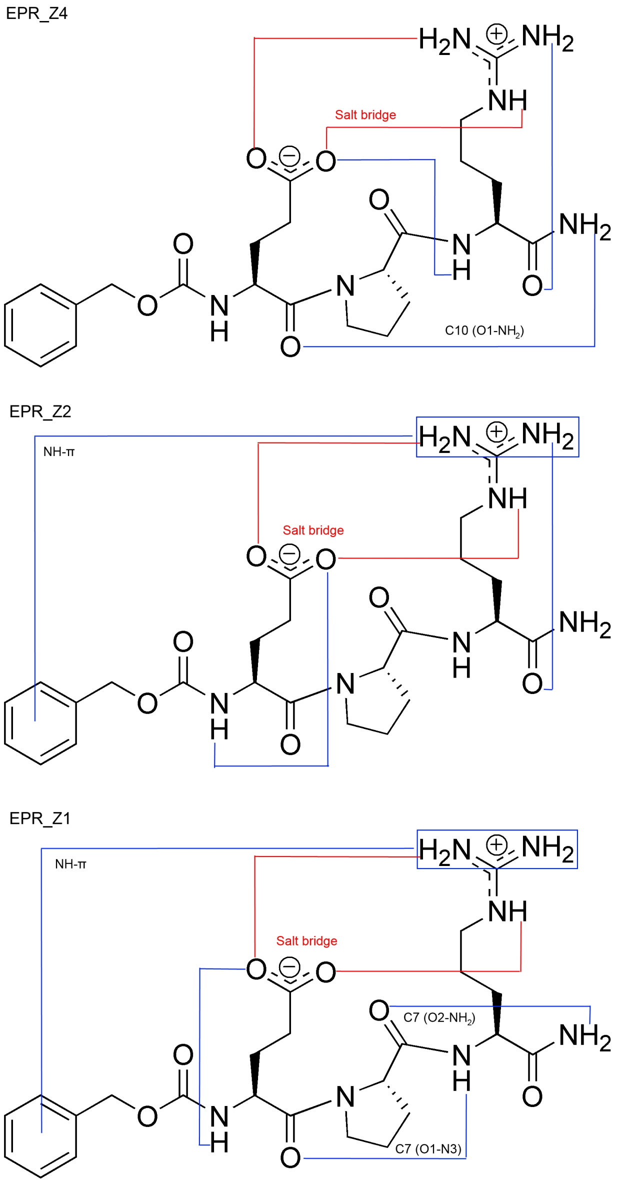
EPR_Z4

EPR_Z2

EPR_Z1

Figure 5.20: Intramolecular interactions in theoretical optimized structures EPR_Z1, Z2 and Z4

5.4 Discussion

The assigned structures for Z-Glu-Ala-Arg-NH_2, Z-Glu-Gly-Arg-NH_2 and Z-Glu-Pro-Arg-NH_2 are shown in Figure 5.21. The occurrence of proton transfer from the acidic side chain of Glu to the basic side chain of Arg is observed for all the assigned structures, leading to generation of zwitterions in overall neutral peptides. The alteration of the character of the center residue results in a different backbone folding, side chain - backbone interactions, but also in different salt bridge interactions.

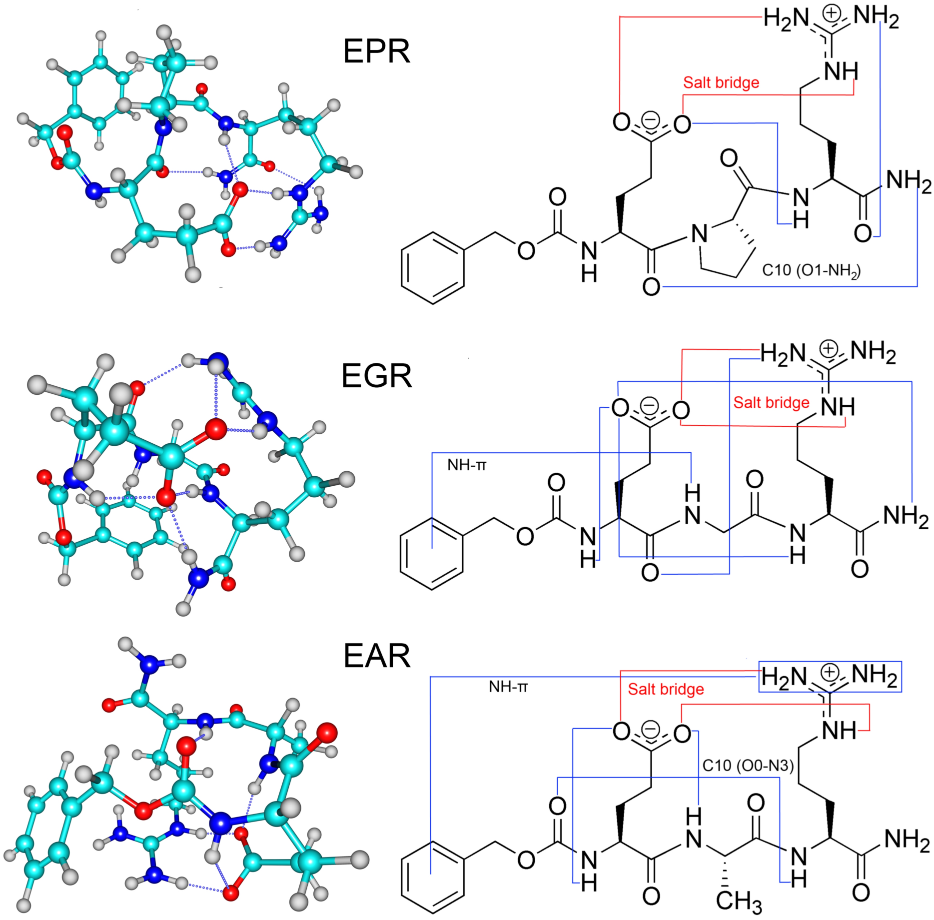

Figure 5.21: Assigned structures and intramolecular interactions for Z-Glu-Ala-Arg-NH_2 (EAR, bottom panel), Z-Glu-Gly-Arg-NH_2 (EGR, middle panel) and Z-Glu-Pro-Arg-NH_2 (EPR, top panel).

The obtained results distinguish themselves from earlier results on the analogues Z-Glu-(Ala)n-Arg-NHMe with n=0, 1 or 3.[61] There we found that independent of the spacer length (of Alanine residues) all conformers exhibit proton transfer and an A type interaction and a C_{10} interaction of the peptide backbone, although the increased flexibility makes the presence of a paired B type interaction more likely. By changing the center spacer from Gly to Ala to Pro, we reduce the flexibility, the folding possibilities and increase the steric hindrance resulting from the increase of the size of amino acid side chain.

Glycine, the smallest and most compact amino acid, allows numerous possible interactions. Indeed, we have found five side chain-backbone interactions, more than we have found for the other two peptides, resulting in a very compact structure (see Figure 5.21). The lack of a distinct backbone fold for the glycine containing peptide is not surprising, since its high conformational flexibility makes it entropically unfavorable to adopt a relatively constrained folded structure. The Glu-Arg side chains in EGR form a bifurcated salt bridge, where one Glu $O\varepsilon$ atom is hydrogen-bonded to the Arg $H\varepsilon$ and $H\eta$ atoms and the other $O\varepsilon$ atom is hydrogen bonded to the peptide backbone NH groups. This type of interaction is for example also found in ATPase[184], indicating its importance in the stabilization of proteins.

For the structure of EAR, a paired A-type salt bridge interaction is observed, in which one Glu $O\varepsilon$ atom is hydrogen-bonded to an Arg $H\eta$ atom and the other Glu $O\varepsilon$ atom is hydrogen-bonded to the Arg $H\varepsilon$ atom. This interaction was also observed in the assigned structures of Z-Glu-Ala_n-Arg-NHMe (n=0, 1, 3) and Ac-Glu-Ala-Phe-Ala-Arg-NHMe.[48;61] The backbone of EAR exhibits a C_{10} interaction resulting in a beta turn, in accordance with studies on Alanine containing peptides, which show these peptides have the propensity to form 3_{10} helices.[48;149]

Proline has the ability to disrupt peptide structure when incorporated into a peptide such as in Z-Glu-Pro-Arg-NH_2, since it can only act as a hydrogen bond acceptor and therefore reduce the possible backbone interactions. Moreover, the distinctive cyclic structure of its side chain gives Proline an exceptional conformational rigidity compared to other amino acids. By using proline as the center residue we expected to clear sets of calculated structures originating from the combination of the Proline rigidity with either the cis or trans orientation of the prolyl peptide bond. As can be seen from Table 5.3, we obtained a varied collection of salt bridge interactions with a 50/50 ratio of cis/trans isomers. The assigned structure of EPR has a paired A type salt bridge interaction, a cis oriented prolyl peptide bond and the backbone forms a C_{10} fold. The latter coincides with the nature of Proline, which aids the formation of beta turns.

Due to the different center residue, there are not too many similarities between the assigned structures of the studied peptides. Examining the energetics of the calculated structures reveals that the energy difference between zwitterionic and non-zwitterionic type in EPR (6.5 kcal/mol) is much smaller than that in EGR(15.4 kcal/mol) and EAR (14.4 kcal/mol) (as can be seen in Table 5.4). Hence,

Table 5.4: Lowest energy (kcal/mol) structures found for each conformational type for Z-Glu-Ala-Arg-NH_2, Z-Glu-Gly-Arg-NH_2 and Z-Glu-Pro-Arg-NH_2.

	Conformational type		
	Zwitterionic	Canonical	Tautomeric
Z-Glu-Ala-Arg-NH_2	0.00	14.40	17.68
Z-Glu-Gly-Arg-NH_2	0.00	15.35	18.10
Z-Glu-Pro-Arg-NH_2	0.00	6.47	7.75

the structures with proton transfer for EPR seem to be less favored energetically. This is probably due to the higher rigidness of EPR peptide backbone, leading to more strain and stress on the global structure during proton transfer. Even so, the Coulomb attraction between the protonated Arg side chain and the deprotonated Glu side chain is still strong enough to overcome the extra forces generated on the backbone. Therefore, it is reasonable that structures with proton transfer are observed for all the Z-Glu-Xxx-Arg-NH_2 peptides studied here. The high basicity of the Arginine side chain is of particular importance since replacing Arg by a residue with a less basic side chain such as Lysine, does not result in proton transfer.[178]

5.5 Conclusions

A conformational analysis has been performed for the overall neutral biomolecules Z-Glu-Xxx-Arg-NH_2 (Xxx= Gly, Ala or Pro) under isolated conditions. By comparing IR-UV ion dip measured spectra of investigated peptides to DFT calculated spectra, zwitterionic structures with high stability were assigned to all the studied peptides independent of their center residue. For Z-Glu-Gly-Arg-NH_2, the assigned structure exhibits a bifurcated type ($C^\star$ type) of salt bridge interaction where one carboxylic oxygen atom of the Glu side chain H-bonds to the guanidine of Arg while the other H-bonds to backbone NH groups. In the assigned structure of Z-Glu-Ala-Arg-NH_2, a paired type (A type) of interaction between glutamic acid and arginine is found. Besides, a backbone H-bond C_{10} interaction between the C=O group of the Z-cap and the NH group of the Arg residue, a dispersion interaction between the Arg side chain and the Z-cap, and two H-bonds between backbone NH groups and side chain oxygen atoms were also presented in the assigned structure. The conformer of Z-Glu-Pro-Arg-NH_2 in the experiments can be assigned to the structure, which adopts the same type of salt bridge interaction as that in Z-Glu-Ala-Arg-NH_2. In addition, backbone H-bonds C_{10} interactions and backbone-side chain interaction could also be observed in assigned structures of Z-Glu-Pro-Arg-NH_2 as well.

The three-dimensional structure of the peptides, resulting from the salt bridge interaction, the backbone folds and side chain-backbone interactions, directly reflects the propensity of the integrated center residue. However, the nature of the center residue does not control whether proton transfer occurs, it only influences the type of salt bridge interaction. Generally, in the studied Glu-Xxx-Arg peptides proton transfer occurs readily, leading to the formation of zwitterions in overall neutral peptides under the controlled and isolated conditions of the molecular beam environment.

6 Exploring the catalytic mechanism of ATP conversion at the molecular level: Binding site recognition and docking of ATP probed by Mass Spectrometry

Abstract

Adenosine-5′-triphosphate (ATP) is a ubiquitous coenzyme appointed by nature to store and transport energy through the cell and to transfer its energy to subsequent processes such as mechanical motion or formation of high-energy chemical compounds. The required energy for these processes is obtained from the hydrolysis of ATP, which is catalyzed by the protein ATP hydrolases (ATPases). Although, the crystal structure and the working principle of numerous ATP driven proteins are generally known and has been described at a global level, this apparently simple ATP conversion reaction is yet poorly understood at the level of local interactions. Questions such as "Can we explain why ATP is selectively bound to the active sites of ATPases?" and "Why is the conversion of ATP to ADP (cleavage of the β-γ phosphate bond) preferred over other reactions at active site?" await detailed answers at the atomistic level. Here, mass spectrometry (MS) based techniques are applied to answer these questions. Under these controlled conditions, we have been able to activate the ATP conversion reaction within the peptide environment. Moreover, the MS based bottom-up approach provides us with the desired level of detail providing information on the specificity and strength of the nucleotide-peptide recognition. This paper shows that ATP forms more stable hydrogen bonds with binding site peptide mimics than other phosphorylated biomolecules do, indicating its preferred binding. Furthermore, when the ATP into ADP conversion is induced by activating the ATP-peptide complex, we observe that the stable ADP-peptide complex is formed, directly illustrating the nature's hydrolysis pathways.

6.1 Introduction

The nano-scale biomolecular motors, selected by nature to transfer chemical energy into mechanical motion have an unprecedentedly high efficiency[195–197], and are regarded as fascinating systems. Structural characterization methods such as nuclear magnetic resonance (NMR)[198;199], X-ray diffraction (XRD)[200–202], fluorescent spectroscopy[203–206], atomic force microscopy (AFM)[207–209], etc., have provided important insights on the molecular structure and functional mechanism of biomolecular motors. The investigation on the membrane enzyme F_oF_1-ATP synthase (F_oF_1-ATPase)[200;205;209–214] has not only disentangled the global motions and structures of this protein, but also the underlying mechanism of fuel of energy in living organisms[215–218]. In addition, it brought inspiration for designing artificial molecular motors[219–221]. Even though, several fundamental principles are still unclear. Due to the complex environment required for ATPases to properly perform their intrinsic functions, it turns out to be a great challenge to fully characterize the interaction between this kind of enzyme and their substrates on an atomistic level.

The X-ray crystallographic[200;222;223], mutation[224;225] and theoretical[226] studies suggest that only a few amino acid residues in most ATPases, as for example F_oF_1-ATPase, are actually involved in binding ATP: glutamic acid (Glu), arginine (Arg) and lysine (Lys), i.e., the so-called arginine finger[226]. A similar arginine finger is also observed in GTP (guanosine triphosphate) driven proteins such as TBC domain GAPs,[227] RasGAPs,[228] etc. For our studies, the binding site will be mimicked by those residues that actively bind ATP. To obtain detailed insight in the binding selectivity of ATP to the binding site, the stability of the complexes formed by ATP and the binding site Arginine finger peptides is investigated.[229–231] In this paper, a mass spectrometry based approach is employed, i.e., the complex of interest is brought into gas phase in ionized form and trapped for further experimental interrogation. Through collision induced dissociation (CID) measurements, relative binding affinities of various phosphorylated biomolecules to a specific arginine finger peptide can be derived. Interestingly, under these water-free conditions, the conversion of ATP-peptide complex to ADP-peptide complex and an inorganic phosphate group still occurs (see Figure 6.1), suggesting that the selected method provides an platform to study biologically relevant process.

The collision-induced dissociation technique, coupled with electrospray ionization, has already proven to be a powerful tool to investigate biomolecular complexes[232–235]. Here, employing this method, the underlying mechanism of binding selectivity of ATP can be illustrated by exploring the relative binding strength of relevant complexes. Moreover, the activation energy of conversion of ATP-peptide to ADP-peptide is found to be lower than that of any other uni-complex dissociation pathway, indicating that the suggested energetically favourable β-γ phosphate bond dissociation process in biological environment is also preferred by gas phase thermodynamics.

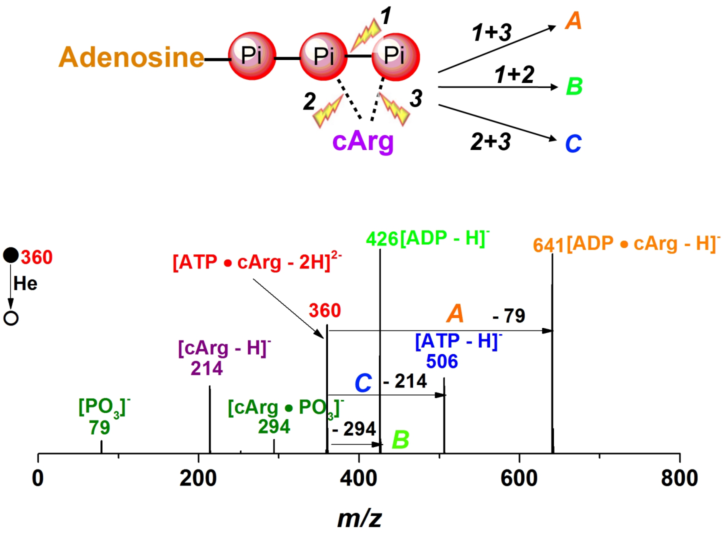

Figure 6.1: CID mass spectrum of [ATP·cArg-2H]$^{2-}$ (m/z = 360, highlighted by red), resulting in [ADP·cArg-H]$^{-}$ (orange, channel A), [ADP-H]$^{-}$ (green, channel B) and [ATP-H]$^{-}$ (blue, channel C) by loss of [PO$_3$]$^{-}$, [cArg·PO$_3$]$^{-}$ (dark blue) and [cArg-H]$^{-}$ (purple), respectively. Above the MS the hypothetical pattern of bond cleavage for each channel is shown.

6.2 Experimental methods

The arginine finger, present in many ATP and GTP driven proteins, is mimicked by the amino acid Arginine (abbreviated 'Arg'): the peptide Ac-Arg-NH$_2$ ('cArg'), and Ac-Glu-Gly-Arg-NH$_2$ ('cEGR'). Since arginine is the key residue in the arginine finger, we start with the smallest possible mimic Arg, by capping the end termini in cArg, the protein environment will be better simulated as now both amino and carboxyl groups participate in peptide bonds. cEGR allows us to include a second dominant residue, namely Glutamic Acid (Glu) inducing possible zwitterion forming of the peptide mimic.[61;141] The chemical structures of these peptides together with phosphorylated biomolecules ATP, Adenosine-5′-diphosphate (ADP), Adenosine-5′-monophosphate (AMP), Guanosine-5′-diphosphate (GTP) and Glucose-6-phosphate (G6P) are presented in in their neutral state Scheme 6.1.

The experiments were performed using the Lyon quadrupole ion trap mass spectrometer (LCQ Classic, Thermo Finnigan) with electrospray ionization (ESI) source. The samples arginine (> 98% purity), ATP magnesium salt, ADP, AMP monohydrate, GTP sodium salt hydrate and G6P sodium salt (> 95% purity) were purchased from Sigma-Aldrich and were used without further purification.

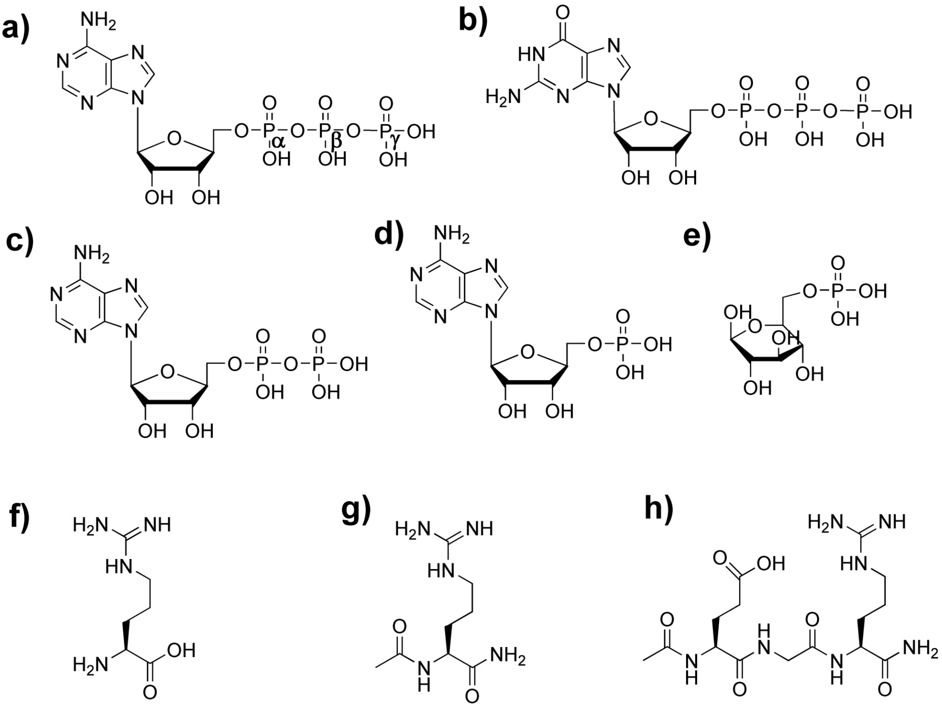

Scheme 6.1: Chemical structures of neutral phosphorylated biomolecules a) Adenosine-5′-triphosphate (ATP), b) Guanosine-5′-diphosphate (GTP), c) Adenosine-5′-diphosphate (ADP), d) Adenosine-5′-monophosphate (AMP), e) Glucose-6-phosphate (G6P) and arginine finger mimics, f) Arginine (Arg), g) Ac-Arg-NH_2 (cArg), h) Ac-Glu-Gly-Arg-NH_2 (cEGR).

The sample cArg was purchased from Bachem and cEGR was lab synthesized. The complexes of interest were formed by dissolving the composing molecules in a 1:1 (v:v) mixture of water and methanol at a concentration of approximately 100 μmol/L for each component.

The sample solution was injected into the ESI source using a syringe pump at a flow rate of 4 μL/min with nitrogen as the sheath gas. The ionized gas-phase complexes were transferred via a heated capillary, a set of ion lenses and two focusing octapole ion guides to the quadrupole ion trap. Here the ions of a specific m/z can be trapped by applying an AC voltage to the ring electrodes and resonantly accelerated to collide with the helium buffer gas (10^{-2} Torr) by adding an auxiliary AC voltage to the end electrodes. CID was performed on the trapped ions of interest by applying an excitation AC voltage to the trap end caps to induce collisions of the isolated ions with the helium buffer gas (10^{-2} Torr). The Mathieu parameter (q_z) of 0.25 was used by LCQ for resonance excitation and the voltage amplitude was varied between 0 and 2.5 V (zero-to-peak). The detection efficiency is poor for lower *m/z* features. Mass spectra were recorded from *m/z* 50-1000.

The primary data from the CID experiments are fractional abundances of the parent and fragment ions as a function of the relative collision energy. Because of the complexity of processes in ion traps[105;106], such as the mass effect on collision energy to internal energy conversion efficiency, it is not straightforward to convert the experimental data (collision energy) into absolute bond energies. However, in the software of Finnigan ion traps, the parameter normalized collision energy (NCE)[107], which is given as a percentage of a standard excitation amplitude, is used. Within this value the mass of the parent ion is taken into account to compensate for the mass effect on the internal energy of the resonantly excited ion. Therefore, the relative stability of the selected ions can be compared by the NCE required to start fragmentation.

6.3 Results and Discussion

6.3.1 ATP to ADP conversion mimic

All of the studied peptides Arg, cArg and cEGR are found to be able to bond to ATP forming singly and doubly deprotonated complexes in the negative mode ESI spectra. The intensities of these ions are high enough to conduct CID experiments, the results of which are presented in Figure 6.2.

The main product for the dissociation of singly deprotonated complexes (see Fig. 6.2a, 6.2c and 6.2e) is $[\mathrm{ATP\text{-}H}]^-$ while a minor fraction of $[\mathrm{ADP\text{-}H}]^-$ is detected. This indicates that the hydrogen bond interactions (H-bonds) between ATP and the peptide are broken in the collisions and this is the lowest energy pathway. For the doubly deprotonated complexes (see Fig. 6.2b, 6.2d and 6.2f), a common dissociation scheme is shared upon collisional activation, as shown below:

$$[\mathrm{ATP} \cdot \mathrm{Peptide} - 2\mathrm{H}]^{2-} \xrightarrow{\mathrm{diss.}} [\mathrm{ATP} - \mathrm{H}]^{-} + [\mathrm{Peptide} - \mathrm{H}]^{-}\,. \tag{6.1}$$

where peptide represents the arginine finger binding site mimics. This pathway 6.1 is the only observed fragmentation channel for the CID of both $[\mathrm{ATP{\cdot}Arg\text{-}2H}]^{2-}$ and $[\mathrm{ATP{\cdot}cEGR\text{-}2H}]^{2-}$. This suggests that in these doubly deprotonated complexes the hydrogen bond interaction between ATP and the peptide mimic is the weakest bond, resulting in the dissociation into the two individual molecular species forming the complex. However, two complementary pathways are observed for the CID of $[\mathrm{ATP{\cdot}cArg\text{-}2H}]^{2-}$, given by:

$$[\mathrm{ATP} \cdot \mathrm{cArg} - 2\mathrm{H}]^{2-} \xrightarrow{\mathrm{diss.}} [\mathrm{ADP} \cdot \mathrm{cArg} - \mathrm{H}]^{-} + [\mathrm{PO_3}]^{-}\,. \tag{6.2}$$

$$[\mathrm{ATP} \cdot \mathrm{cArg} - 2\mathrm{H}]^{2-} \xrightarrow{\mathrm{diss.}} [\mathrm{ADP} - \mathrm{H}]^{-} + [\mathrm{cArg} \cdot \mathrm{PO_3}]^{-}\,. \tag{6.3}$$

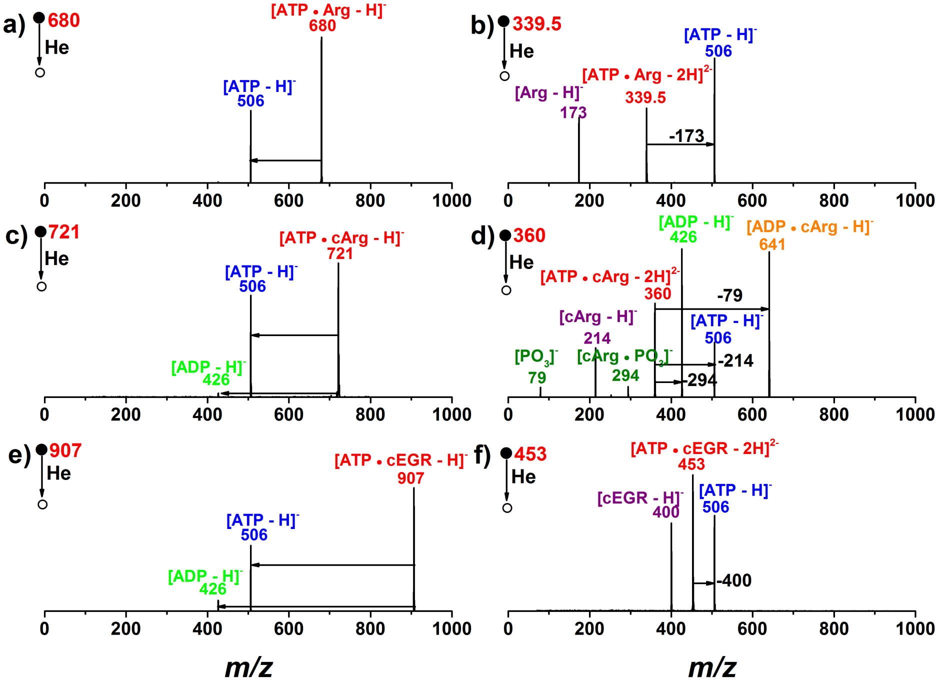

Figure 6.2: Collision induced dissociation mass spectra of a) $[ATP{\cdot}Arg\text{-}H]^-$ (m/z = 680), b) $[ATP{\cdot}Arg\text{-}2H]^{2-}$ (m/z = 339.5), c) $[ATP{\cdot}cArg\text{-}H]^-$ (m/z = 721), d) $[ATP{\cdot}cArg\text{-}2H]^{2-}$ (m/z = 360), e) $[ATP{\cdot}cEGR\text{-}H]^-$ (m/z = 907) and f) $[ATP{\cdot}cEGR\text{-}2H]^{2-}$ (m/z = 453). The precursor ions, i.e. ATP-peptide complex ions are highlighted by red and the fragment ions are highlighted by the following schemes: $[ATP\text{-}H]^-$ (blue), $[ADP\text{-}H]^-$ (green), $[ADP{\cdot}cArg\text{-}H]^-$ (orange), peptide ion (purple), and ions related to phosphate group (dark green).

In both channels cleavage of the $P_{\beta}O_3$-$P_{\gamma}O_3$ bond occurs, the key step in the hydrolysis of ATP. Especially the formation of $[ADP{\cdot}cArg\text{-}H]^-$ proves that ADP-peptide complex, the intermediate of ATP hydrolysis in biology, can be observed under this water-free condition. The formation of both $[ADP{\cdot}cArg\text{-}H]^-$ and $[ADP\text{-}H]^-$ indicates that cArg can binds to either the β-phosphate of ATP or the γ-phosphate or to both simultaneously (see Fig. 6.1). Hence, cArg seems to be an effective mimic to interact with ATP and induce ATP conversion into ADP.

This $P_{\beta}O_3$-$P_{\gamma}O_3$ bond breaking is only observed for $[ATP{\cdot}cArg\text{-}2H]^{2-}$. We observe that this reaction requires the highest collision energy to fragment 50% amount of presursor ion (see Fig. 6.3a, dianion series). Here, the hydrogen bonds between ATP and cArg in $[ATP{\cdot}cArg\text{-}2H]^{2-}$ are strong enough to compete with the dissociation of the phosphate bond, resulting in several simultaneous dissociation pathways during CID of this doubly deprotonated complex. For the more stable singly deprotonated complexes (see Fig. 6.3a, anion series), the dissociation channel in which bond fission of phosphate bond takes place is not observed,indicating that $P_{\beta}O_3$-$P_{\gamma}O_3$ is more stable than H-bonds between ATP and a peptide in the singly deprotonated complexes. Here, the observed altered relative stability of phosphate bond and the hydrogen bonds in singly and doubly deprotonated complexes possibly results from their different number of charges. The negative phosphate group attracts hydrogen from amide group of cArg side chain more intensely than neutral phosphate group does, which makes the H-bond formed between deprotonated phosphate group and cArg more stable. Hence, the H-bond in doubly deprotonated complex are expected to be stronger than that in singly deprotonated complex. Considering the general bond energy of the $P_{\beta}O_3$-$P_{\gamma}O_3$ bond (30.5 kJ/mol)[236] and that of the NH$\cdots$O H-bond (16.8-25.2 kJ/mol)[237], it is likely that the above described charge effect in the doubly deprotonated complex increases the strength of H-bond. Thereby allowing fragmentation into $[ADP{\cdot}cArg\text{-}H]^-$ and $[PO_3]^-$. However, it should be notice that the occurrence of a pathway depends on not only bond energy, but on the energy barrier as well. Because of the coulomb repulsion effect in the doubly deprotonated complex, the energy barrier for cleavage of $P_{\beta}O_3$-$P_{\gamma}O_3$ bond will be lower for the doubly deprotonated complex than for the singly deprotonated complex. As a result, during collision activation of $[ATP{\cdot}cArg\text{-}2H]^{2-}$, three simultaneous fragmentation channels are observed, in which both phosphate bond and H-bonds can be broken. Beside the two dissociation pathways resulting in $[ATP\text{-}H]^-$ or $[ADP{\cdot}cArg\text{-}H]^-$ a third dissociation pathway is observed. This involves the fission of the phosphate bond as well, however and leads to formation of $[ADP\text{-}H]^-$ and $[cArg{\cdot}PO_3]^-$. This is a very interesting process as ADP resulting from the conversion of ATP-peptide complex into ADP and PO_3-peptide, is observed here, which is the final product of ATP hydrolysis in nature. Although in proteins the production of ADP results from the dissociation of the intermediate ADP-Peptide complex, this channel indicates that under our experimental conditions ATP can be directly converted to ADP without the process to form an intermediate. However, based on the relative activation energy of relevant processes (see Table 6.1), the dissociation channel to form $[ADP{\cdot}cArg\text{-}H]^-$ is much preferred than that to $[ADP\text{-}H]^-$, which may partially account for the generation of ADP-Peptide complex in hydrolysis of ATP in nature.

6.3.2 Binding selectivity of ATPase towards ATP

Since ATP is effectively converted to ADP in the $[ATP{\cdot}cArg\text{-}2H]^{2-}$ complex, we have selected the cArg peptide to study the binding selectivity of ATP with respect to other phosphorylated biomolecules (PhBi). The ion survival yield of cArg-PhBi complexes as a function of relative collision energy in the CID experiments is shown in Figure 6.3.

It can be seen that the energy required to dissociate 50% of the precursor ionic

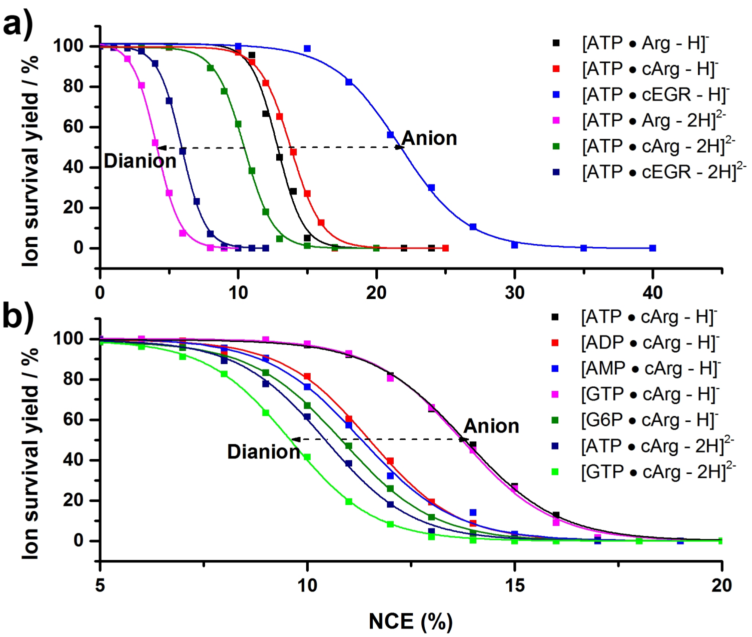

Figure 6.3: Ion survival yield of complexes formed by a) ATP with Arg, cArg or cEGR, b) cArg with ATP, ADP, AMP, GTP or G6P as a function of normalized collision energy (NCE,the factor determines the ion internal energy converted from collisional energy independent of m/z of parent ion) in CID experiments. The curves are fitted using sigmoid functions[108].

complex is significantly higher for the singly deprotonated complexes [ATP·cArg-H]$^-$ and [GTP·cArg-H]$^-$. This observation is consistent with both ATP and GTP containing three phosphate groups. These two molecules are able to form more H-bonds with cArg than the other phosphorylated biomolecules. This assumption is verified by the decreased energy order to dissociate 50% amount of initial [ADP·cArg-H]$^-$, [AMP·cArg-H]$^-$ and [G6P·cArg-H]$^-$, respectively. Moreover, examining the x-ray structures in the protein data bank show that in many proteins three H-bonds are formed between ATP and the Arginine residue while formation of only one or two H-bonds is preferred when ADP interacts with Arginine residue of proteins.[213;238–241]

The doubly deprotonated complexes [ATP·cArg-2H]$^{2-}$ and [GTP·cArg-2H]$^{2-}$ (other cArg-PhBi dianions are not observed in the mass spectra) are found to be less stable upon collision induced dissociation than the associated singly deprotonated complexes. The reduced stability of the doubly deprotonated complexes may find its origin in the Coulomb repulsion between the two negatively charged sites in the doubly deprotonated complexes, which lowers the threshold of this pathway.[242] Overall, ATP and GTP have higher binding affinities for cArg (the effective binding site mimic of ATPases) than other phosphorylated biomolecules, indicating the binding preference of ATPases (GTPases) to ATP (GTP). This is probably one of the reasons why ATP can be selectively recognized in the complex biological environment by ATPases.

6.3.3 ATP to ADP conversion mechanism

Although ATP is selectively recognized by ATP converting proteins via the formation of multiple hydrogen bonds, three different dissociation channels are observed in the CID of [ATP·cArg-2H]$^{2-}$, as can be seen from time-resolved CID MS in Figure 6.4. According to the hypothetical mechanism of bond fragmentation as shown in Figure 6.1, the formation of [ADP·cArg-H]$^{-}$ and [PO$_3$]$^{-}$ (Channel A) results from the cleavage of $P_\beta O_3$-$P_\gamma O_3$ bond and the cArg$\cdots\gamma$-phosphate group hydrogen bond. Breaking of $P_\beta O_3$-$P_\gamma O_3$ bond and the cArg$\cdots\beta$-phosphate group hydrogen bond generates [ADP-H]$^{-}$ and [cArg·PO$_3$]$^{-}$ (Channel B). In channel C two hydrogen bonds are broken, leading to production of [ADP-H]$^{-}$ and [cArg-H]$^{-}$. In order to address the question "Which process is favored by thermodynamics?", an energy-dependent kinetic method[109] is employed here to acquire the relative activation energies of these fragmentation channels.

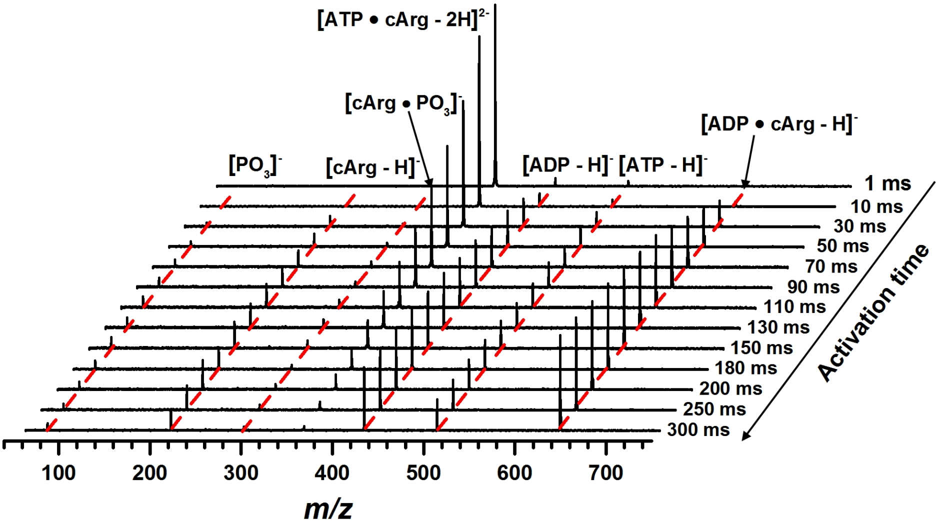

Figure 6.4: [ATP·cArg-2H]$^{2-}$ fragmentation followed by increasing collision time at 12% NCE.

Central to this kinetic method are measurements of the rates, k_j, for the formation of fragment j. The rates of fragment formation can be determined by measuring both the parent as the fragment intensities as a function of the collisional activation time (see Fig. 6.5a). It can be seen that the abundance of [ADP·cArg-H]$^-$ is the highest, followed by that of [ADP-H]$^-$ and the [ATP-H]$^-$ fragment has the lowest abundance. Therefore, we can conclude that the formation of [ADP·cArg-H]$^-$ is favored from the aspect of bond dissociation energy.

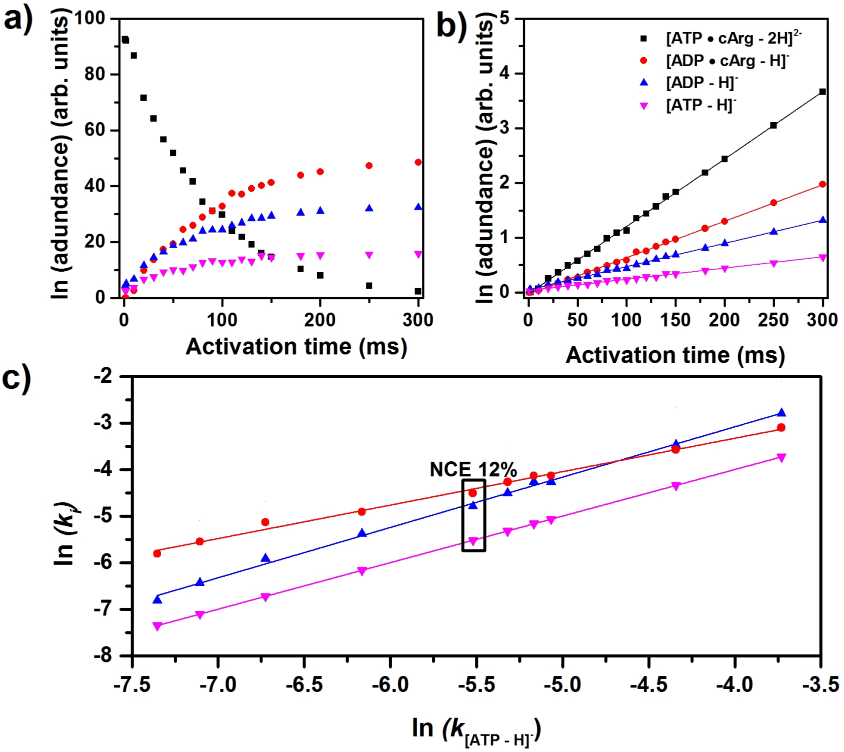

Figure 6.5: a) Relative abundances of parent and fragment ions as a function of activation time with 12% NCE, b) Kinetic plots of and fragment ions as a function of activation time with 12% NCE; the slopes of the fitted lines correspond to the rate constants of consuming (producing) precursor (fragment) ions. C) Rate constants of various dissociation channels as a function of the rate constant of producing [ATP-H]$^-$.

In an ion trap only the ion with a specific *m/z* can be resonantly accelerated and thereby collide with the buffer gas. All induced dissociation processes follow first-order kinetics, where the intensity of the parent ion of interest I_{parent} is given as a function of collision time t by

$$I_{\text{parent}}(t) = I_0 \exp\left(-k_{\text{parent}} t\right) \tag{6.4}$$

where I_0 is the parent intensity without collisional activation. The fragment intensities I_j are given by

$$I_j(t) = \frac{k_j}{k_{\text{parent}}} \left[I_0 - I_{\text{parent}}(t) \right]. \tag{6.5}$$

From Equations 6.4 and 6.5, it can be deduced that plots of $-\ln\left[I_{\text{parent}}(t)/I_0\right]$ and $I_j(t)\ln\left[I_{\text{parent}}(t)/I_0\right] / \left[I_{\text{parent}}(t) - I_0\right]$ versus t should yield straight lines with slopes equal to k_{parent} and k_j, respectively.

Figure 6.5b shows the kinetic plots constructed from the plots in Figure 6.5a. The slopes of the least-squares fitted straight lines are the rate constants corresponding to the dissociation of parent ion or the formation of fragment ions. The same analysis was performed at a set of values of NCE ranging from 8% to 25%. Hence a series of rate constants was obtained as a function of NCE. Based on Arrhenius' law, it is known that the activation energy E_{act} of a dissociation channel can be determined by measuring its rate constant k as a function of the effective temperature. However, the effective temperature increases with increasing NCE and cannot be controlled directly. A second fragmentation process has to be selected as a reference to eliminate the factor of effective temperature. Plotting $\ln k_1$ versus $\ln k_2$ (as shown in Equation 6.6) will yield a straight line with slope $E_{\text{act},1}/E_{\text{act},2}$, 2, i.e. the activation energy of dissociation channel 1 relative to the activation energy of channel 2.

$$\ln k_1 = \ln A_1 - \frac{E_{\text{act},1}}{E_{\text{act},2}} \ln A_2 + \frac{E_{\text{act},1}}{E_{\text{act},2}} \ln k_2. \tag{6.6}$$

The direct dissociation pathway (3), which result in the formation of [ATP-H]$^-$, has been used as a reference, i.e. its activation energy was set to 1. The natural logarithms of all rate constants were plotted against the natural logarithm of the rate constant of forming [ATP-H]$^-$, which is shown in Figure 6.5c. The slopes of the least-squares fitted straight lines correspond to the relative activation energies of the fragmentation processes and are presented in Table 6.1.

Table 6.1: Activation energies of competing fragmentation processes from [ATP·cArg-2H]$^{2-}$ relative to the activation energy of [ATP-H]$^-$ formation.

Ions of complexes	CID fragments	Activation Energy
[ATP·cArg-2H]$^{2-}$	[ATP-H]$^-$	1 (reference)
	[ADP-H]$^-$	1.08 ± 0.02
	[ADP·cArg-H]$^-$	0.72 ± 0.02

It can be seen that formation of [ADP·cArg-H]$^-$ has the lowest energy barrier of the investigated dissociation channels. The activation energy of the formation of [ADP-H]$^-$ and [ATP-H]$^-$ is very close. Nevertheless, according to the above described hypothetical fragmentation mechanism of [ATP·cArg-2H]$^{2-}$, one should expect a similar energy barrier for the dissociation channels that produce [ADP·cArg-H]$^{-}$ and [ADP-H]$^{-}$, since both channels involve breaking of the same $P_\beta O_3$-$P_\gamma O_3$ bond and a cArg$\cdots$phosphate group H-bond. The discrepancy probably reflects the difference in the stability of the dissociation products, i.e., [ADP·cArg-H]$^{-}$ should be more stable than [ADP-H]$^{-}$. This can easily be explained considering the structure of the [ADP·cArg-H]$^{-}$ complex, where the negative charge on ADP is stabilized by forming a complex with a proton donor, such as cArg. Moreover, considering the similar stability of [ATP-H]$^{-}$ and [ADP-H]$^{-}$ [242], it is not surprising to see that the activation energy of the dissociation channel resulting in [ATP-H]$^{-}$ is very close to that of [ADP-H]$^{-}$.

The here obtained relative activation energies can directly be connected to the general knowledge of ATP hydrolysis in biological environment. It is known that the hydrolysis of ATP, does not occur spontaneously indicative of a high energy barrier for this reaction. This energy barrier is strongly reduced when ATP binds to the binding site or hydrolase. The cleavage of $P_\beta O_3$-$P_\gamma O_3$ bond results in the production of the transient ADP-enzyme complex. It is interesting that in the hydrolysis of ATP, the formation of ADP-enzyme complex is preferred above that of generating free ADP. This observation may be partially because of the lower energy barrier in forming intermediate ADP-Peptide complex, which can be seen from the lowest activation energy of dissociation channel to [ADP·cArg-H]$^{-}$ in the CID of [ATP·cArg-2H]$^{2-}$. However, in nature breaking of the bond between ADP and peptide occurs immediately after the formation of ADP-peptide intermediate, which releases ADP. This is not observed in our experiments as CID is a resonant process in which only the selected ion [ATP·cArg-2H]$^{2-}$ is resonantly accelerated to collide with buffer gas while the produced fragment ions including [ADP·cArg-H]$^{-}$ will be trapped without any further collisions. Therefore, from a thermodynamic viewpoint, it can be concluded that nature favors the formation of a stable intermediate ADP-enzyme complex in hydrolysis of ATP.

Since has the lowest activation energy in the CID of ATP-cArg complex, it is also possible that formation of intermediate ADP-Peptide complex is because of its lower energy barrier than that of producing ADP directly; Besides, since CID in ion trap is a resonant process, only the selected ion [ATP·cArg-2H]$^{2-}$ is resonantly accelerated to collide with buffer gas while the produced fragment ions including [ADP·cArg-H]$^{-}$ will be trapped without any further collision.

6.4 Conclusions

ESI-MS coupled with collision induced dissociation technique was employed to study the complexes formed between phosphorylated biomolecule ATP, ADP, AMP, GTP or G6P and ATPases active site mimic peptides Arg, cArg and cEGR. The binding selectivity of ATPases towards ATP has been investigated by the relative stability of various complexes, while the relative activation energy in the CID of a specific complex reveals the preferred process in the ATP to ADP conversion. This method makes it possible to mimic the ATP to ADP conversion reaction even under the water-free conditions of our experiment. Collisional induced activation of the ATP-peptide complex ([ATP·cArg-2H]$^{2-}$) generates both the complex [ADP·cArg-H]$^{-}$ and [PO$_3$]$^{-}$.

CID experiments of the ionic complexes of cArg with various phosphrated biomolecules reveal that ATP and GTP bind more strongly to the selected argininge finger binding site peptides than other phosphrylated biomolecules. As the effect of nucleoside is not considered here, it is reasonable to see a similar binding strength of GTP-peptide complex to that of ATP-peptide complex. The strong interactions between the phosphate groups and the arginine finger peptides is one of the reasons why ATPases selectively bind to ATP in nature (other reasons may include such as binding preference of ATPases to Adenosine, etc.). Furthermore, an energy-dependent kinetic method is used to investigate the preferred dissociation pathway when activating the ATP-peptide complex [ATP·cArg-2H]$^{2-}$. The mass spectrum of this complex show three competing fragmentation channels, of which the ATP-to-ADP conversion channel producing [ADP·cArg-H]$^{-}$ has the lowest activation energy. This agrees well with the ATP hydrolysis reaction in nature, forming the ADP-enzyme complex. These experiments are a first, but important, step towards a detailed illustration of the ATP hydrolysis mechanism at the active site of ATPases at the molecular level, and thereby starting to bridge he gap between global and atomic scale. Ultimately it will provide more insight into this fascinating system.

7 Summary

The research described in this thesis focuses on 3-dimensional structure determination of small biomolecules with the goal of unfolding and visualizing relevant molecular interactions. An IR-UV double resonance spectroscopy technique together with a DFT based computational tool is employed to explore the structural preferences and intramolecular interactions of several small peptides, the building blocks of vital biomolecules, i.e. proteins. Compared with technologies used routinely in the laboratory for structure characterization, such as XRD, NMR, IR absorption spectroscopy, etc., the novel IR-UV ion dip spectroscopic method offers the following advantages: 1) It has a fast and simple sample preparation process (the powder of molecule of interest is mixed with matrix graphite powder and attached on the surface of a sample bar for laser desorption sampling or directly used without any pre-treatment for heating sampling) 2) Intrinsic properties of the sample are acquired without any external interference (the sample molecules are brought into gas phase and cooled through supersonic expansion in a pulsed molecular beam) 3) The spectroscopic measurement is mass and conformer selective (The high resolution spectra of isolated molecules with temperatures of only a few tens of Kelvins enables distinction of coexisting conformers, and time-of-flight analysis allows specific detection at the investigated ion mass) 4) The action way to obtain IR absorption spectra (monitoring UV REMPI signal as a function of the wavelength of precedent IR beam) makes this ion dip spectroscopy much more sensitive than direct absorption technique. By comparing the experimental obtained conformer-specific IR spectra with the spectra calculated using DFT, structure can be assigned to each conformer. In this way, the intramolecular interactions which play an important role in the formation of the 3-dimensional structure can be recovered from the DFT calculations.

Conformer-specific measurements require highly resolved spectra. Therefore, it is crucial that the internal temperature of molecules of interest should be very low (~ tens of Kelvins). Laser desorption or thermal heating normally produces a vapor at several hundred Kelvins, which makes cooling afterwards necessary. Pulsed molecular beam technique, in which a static high pressure (a few bars) gas is expanded into a vacuum chamber through a small nozzle (the diameter of which is ~ 0.2 - 1 mm), is found to be able to generate very cold molecules. In chapter 3, we introduce the design and operation of a new home-built valve baptized the Nijmegen Pulsed Valve (NPV). The NPV operation is based on the Lorentz force created by a pulsed current passing through an aluminum strip located in the presence of a magnetic field, which opens the nozzle periodically. It is found that NPV is able to produce a short (down to 20 μs) and rotationally cold (~ 1K rotational temperature) pulsed molecular beam with very high density. Apart from these characteristics, NPV is conceptually simple, easy to build and robust in operation, making itself in near future a very promising and competitive molecular beam source.

In the structures of biomolecules, which were characterized, the intramolecular hydrogen bond is present between many groups and has great importance in the stabilization of peptide structure. In chapter 4, we report a conformational analysis for two very similar dipeptides Ac-Phe-Ser-NH_2 (FS)(Ser side chain: CH_2OH) and Ac-Phe-Cys-NH_2 (FC)(Cys side chain: CH_2SH) using IR-UV ion dip spectroscopy. The effect of the difference in hydrogen bonding for an OH and SH group and consequences for the secondary structure is probed by this subtle side chain alternation. Experimentally, a conformer with β_L-γ_L backbone (C5-C7 hydrogen bonds) structure was observed for both FS and FC. Within this conformer, a side chain involved hydrogen bond S(O)H$\cdots$O=C as well as a dispersive interaction S(O)H-π also contribute to the stabilization of the formed structure. A 2nd conformer was found for FC, the backbone structure of which is in type of β-turn (C10 hydrogen bond). In short, intramolecular interactions including both hydrogen bonds and dispersion interactions are found to play an important role in the stabilization of the conformational structures. Apart from hydrogen bonds and dispersive interactions, another type of intramolecular interaction often influences the 3-dimensional structures of biomolecules, namely the salt bridge. As the strongest non-covalent interaction, this electrostatic force occurs between opposite charges, for instance a positively charged guanidine side chain of arginine and a negatively charged carboxylic acid side chain of glutamic acid. This type of interaction is often observed in solution as water or other polar solvent molecules support the occurrence of proton transfer and stable the charge separation, which is a prerequisite for salt bridge interaction. However, in gas phase, there is not any solvent effect. Whether can the salt bridge still be formed if the charges stay in each other's vicinity? In Chapter 5, a conformational analysis has been performed for the overall neutral biomolecules Z-Glu-Xxx-Arg-NH_2 (Xxx= Gly, Ala or Pro) under the controlled and isolated conditions of the molecular beam environment. The selected peptides allow us to study the effect of flexibility of peptide backbones on possible zwitterion formation, ranging from small and compact (Gly, Ala) to the rigid Pro residue. Generally, in the studied gas phase Glu-Xxx-Arg peptides proton transfer occurs readily, leading to the formation of zwitterions in the overall neutral peptides.

As can be seen from the applications described in chapter 4 and 5, IR-UV double resonance ion dip spectroscopy is a very powerful method for structure determination. However, it requires a UV chromophore to be part of the molecules so that the UV REMPI scheme can be applied. Furthermore, cold molecules are needed in order to obtain highly resolved spectra. Although at present this technique is limited to small biomolecules such as peptides containing up to 15 amino acid residues, with the development of relevant techniques for instance ultra-short pulse laser desorption, low temperature molecular beam, VUV ionization etc., it will be very promising to be applied in biomacromolecules in the near future. Intramolecular interactions are uncovered once the 3-dimensional structure of the molecule is known. However, for complex systems, structure determinations are not always feasible. Is it possible to probe the molecular interactions for instance the strength of a complex bond under this condition? In chapter 6, an ESI ion trap mass spectrometry together with a collision induced dissociation (CID) technique was employed to study ATP hydrolysis by small mimics of the active sites of ATPases. Based on the derived phenomenological binding energies from CID measurements, ATP is found to bind stronger than other phosphorylated biomolecules at the active site mimics of ATPases, indicating that ATP can be selectively recognized. In addition, by employing an energy-dependent kinetic method, the activation energy of hydrolysis-like reaction is found to be lower than that of any other reaction pathway once ATP binds to an appropriate active site mimic of ATPases. This shows that ATP hydrolysis reaction should be the one nature prefers. These experiments are the first steps towards a detailed description of the mechanism of ATP hydrolysis at the atomic level which should provide more insight into this fascinating system.

Samenvatting

Het onderzoek dat in deze dissertatie beschreven is draait om het bepalen van de 3-dimensionale structuur van kleine biomoleculen, met als doel om de relevante moleculaire interacties te visualiseren en begrijpen. Een IR-UV dubbel resonante spectroscopie techniek wordt toegepast samen met DFT berekeningen om de structurele voorkeuren en intramoleculaire interacties van kleine peptiden te verkennen, de bouwblokken van belangrijke biomoleculen zoals eiwitten. In vergelijking met veelgebruikte experimentele methoden zoals XRD, NMR en IR absorptie spectroscopie, biedt IR-UV ion dip spectroscopie de volgende voordelen: 1) De techniek is snel en kent een eenvoudige preparatietechniek (het moleculaire poeder wordt vermengd met grafiet poeder en gebonden aan het oppervlak van een grafieten staaf voor laser desorptie, of het moleculaire poeder wordt direct gebruikt zonder verdere behandeling in een verwarmbare bron). 2) We bestuderen de moleculen in de gasfase en na koeling tot temperaturen van ongeveer 10 Kelvin, waardoor er geen interferentie is door vreemde moleculen en ons hele monster bestaat uit bijna identieke moleculen (de rotatietoestand en conformatie kan nog verschillen). 3) De spectroscopische methode is zowel massa- als conformeer selectief (De hoge resolutie spectra van geïsoleerde en gekoelde moleculen maken het mogelijk onderscheid te maken tussen verschillende conformeren (ruimtelijke structuren verschillen) in dezelfde bundel, en de analyse van de vluchttijd van de moleculen maakt het mogelijk om enkel de ionen die van belang zijn te volgen). 4) Door actie spectroscopie toe te passen om IR spectra te meten (oftewel het meten van het UV REMPI signaal als functie van de golflengte van het voorgaande IR licht) kunnen er veel gevoeligere metingen worden gedaan dan met directe absorptie spectroscopie. Door de experimentele, conformeer-specifieke spectra te vergelijken met de spectra die volgen uit DFT berekeningen kunnen we structuren toewijzen aan elk gemeten conformeer. Op deze manier kunnen de intramoleculaire interacties die een belangrijke rol spelen in de vorming van de 3-dimensionale structuur uit de DFT berekening gehaald worden.

Voor het uitvoeren van conformeer specifieke metingen zijn goed opgeloste spectra nodig. Het is daarom cruciaal dat de interne temperatuur van de te meten moleculen erg laag is (ordegrootte 10 K). Zowel met laser desorptie als met normale verdamping wordt een damp van enkele honderden Kelvin gevormd, dus koeling is in beide gevallen noodzakelijk. Het gebruik van een gepulseerde klep, waarbij gas van een hoge druk (enkele Bar) het vacuüm in wordt geëxpandeerd door een kleine opening (met een diameter van 0.2 tot 1 mm), maakt het mogelijk om zeer koude moleculen te produceren. Na een inleiding in het veld en de experimentele techniek in de hoofdstukken 1 en 2 wordt in hoofdstuk 3 het ontwerp en de werking van een nieuwe gepulseerde klep gepresenteerd, de Nijmegen Pulsed Valve (NPV). De werking van de NPV is gebaseerd op de Lorentz kracht ten gevolge van een gepulseerde stroom door een strook aluminium in een magneetveld, die de klep periodiek opent. Uit ons onderzoek is gebleken dat de NPV zeer korte (tot wel 20 μs) en rotationeel koude (ongeveer 1 K rotationele temperatuur) gaspulsen kan produceren met een hoge gas dichtheid. Naast deze goede eigenschappen is het concept van de NPV simpel, is de klep makkelijk te bouwen en bovendien robuust. Vandaar dat de NPV een veelbelovende moleculaire bron is die in de nabije toekomst al competetief zal zijn.

Biomoleculen kennen verschillende interacties. De meest duidelijke zijn de chemische bindingen tussen atomen en die de primaire structuur van moleculen stabiliseren. De waterstofbrug en de dispersieve krachten tussen groepen zijn veel zwakker, maar zijn wel in staat om de moleculen te verbuigen en van structuur te laten wijzigen bijvoorbeeld gedurende hun reacties in een cel. In hoofdstuk 4 presenteren we onze analyse van de conformeren van twee vergelijkbare dipeptiden (peptiden bestaande uit twee aminozuren), namelijk Ac-Phe-Ser-NH_2 (FS)(Ser zijketen: CH_2OH) en Ac-Phe-Cys-NH_2 (FC)(Cys zijketen: CH_2SH), uitgevoerd door middel van IR-UV ion dip spectroscopie. Op deze wijze meten we het effect van de subtiele verschilen tussen deze twee zijgroepen, een zuurstofatoom in Ser en een zwavelatoom in Cys. Chemisch hebben deze twee atomen grote overeenkomsten. Zwavel is echter wat groter en de waterstofbrug is zwakker bij zwavel. Uit de experimenten blijkt dat zowel FC als FS een stabiele conformeer vertonen met een β_L-γ_L skelet structuur (C5-C7 waterstofbruggen). Bij deze conformeer dragen zowel een waterstofbrug van de zijgroep S(O)H$\cdots$O=C als een dispersie interactie S(O)H-π bij aan de stabiliteit van de gevormde structuur. Voor FC is er bovendien een tweede conformeer gevonden, waarin het skelet in een β-turn gevouwen is (C10 waterstofbrug). In het kort kunnen we zeggen dat intramoleculaire interacties zoals waterstofbruggen en dispersie interacties een belangrijke rol spelen in de stabilisatie van de structuur van conformeren.

Buiten de waterstof brug en de dispersie interactie is er nog een type intramoleculaire interactie die vaak de 3-dimensionale structuur van biomoleculen beïnvloedt, namelijk de zoutbrug. Deze electrostatische kracht - de sterkste niet-covalente interactie - treedt op tussen tegengesteld geladen groepen zoals de positief geladen zijgroep van arginine en de negatief geladen zijgroep van glutaminezuur. Dit type interactie wordt vaak gezien in een oplossing aangezien water en andere polaire oplosmiddelen proton overdracht makkelijker maken en bovendien de gescheiden ladingen kunnen stabiliseren, wat een vereiste is voor de zoutbrug interactie. In de gas fase is er echter geen stabiliserend effect van een oplosmiddel. Is het dan alsnog mogelijk om een zoutbrug te vormen als de ladingen dichtbij elkaar verblijven? In hoofdstuk 5 is een analyse van de conformeren van de neutrale (ongeladen) biomoleculen Z-Glu-Xxx-Arg-NH_2 (Xxx= Gly, Ala of Pro) uitgevoerd onder de gecontroleerde en geïsoleerde omstandigheden van de moleculaire bundel. Deze selectie van peptides zorgt ervoor dat we het effect van de flexibiliteit van het peptide skelet op de vorming van zwitterionen kunnen bestuderen, met kleine en compacte aminozuren zoals Gly en Ala tot het stijvere Proline. In het algemeen treedt proton overdracht redelijk gemakkelijk op voor de Z-Glu-Xxx-Arg-NH_2 peptide moleculen in de gas fase, wat leidt tot de aanwezigheid van zwitterionen in de netto ongeladen peptiden.

Zoals te zien is in hoofdstukken 4 en 5 is IR-UV dubbel resonantie ion dip spectroscopie een zeer krachtige techniek voor het bepalen van de structuur van moleculen. Er is echter wel altijd een UV chromophoor nodig in het te meten molecuul zodat REMPI spectroscopie mogelijk is. Bovendien is het noodzakelijk dat de moleculen effectief gekoeld worden zodat goed opgeloste spectra kunnen worden gemeten. Hoewel deze techniek momenteel beperkt is tot kleine biomoleculen zoals peptiden met maximaal 15 aminozuren, worden er momenteel vele nieuwe technieken ontwikkeld, zoals ultrasnelle laser desorptie, moleculaire bundels met nog lagere temperatuur en VUV ionisatie, om dubbel resonantie spectroscopie toe te passen op bio-macromoleculen.

De eigenschappen van de intramoleculaire interacties worden duidelijk zodra de 3-dimensionale structuur van het gehele molecuul duidelijk wordt. Voor sommige complexe systemen is het echter niet mogelijk om de structuur in detail te bepalen. Structuur van moleculen is één aspect van het functioneren van biomoleculen. Een ander en belangrijk aspect is het binden en loslaten van substraten in enzymatische reacties. Eén van de belangrijkste reacties is de hydrolyse en de vorming van adenosine trifosfaat (ATP), de energiedrager in ons lichaam. In hoofdstuk 6 wordt een ESI ionenval massaspectrometer samen met een botsing geinduceerde dissociatie (CID) techniek toegepast om de hydrolyse van ATP door kleine model-moleculen van het actieve centrum van het ATP-ase enzym te bestuderen. Variatie van de botsingsenergie en het volgen van de massa van de ionen maakt het mogelijk vast te stellen wat de bindingsenergieën zijn van ATP en ADP. Het blijkt dat ATP sterker bindt aan het actieve centrum van ATPase model systemen dan andere gefosforyleerde biomoleculen. ATP kan dus selectief worden herkend. Tegelijkertijd is ook aangetoond dat de activeringsenergie voor hydrolyse en ADP vorming de laagste is van alle mogelijk reacties, hetgeen laat zien dat ATP hydrolyse de voorkeursreactie is van de natuur. Deze experimenten zijn de eerste stappen in de richting van een gedetailleerde beschrijving van het mechanisme van de hydrolyse van ATP op atomair niveau en naar een antwoord op de vraag welke eigenschap van chemische reacties de natuur gebruikt om te voorkomen dat interne energie van ATP verloren gaat in warmte en om te zorgen dat de potentiële energie van ATP terecht komt in energie-kostende reacties zoals beweging en groei.

Bibliography

[1] P. J. Russell. *iGenetics: A Molecular Approach*. Pearson Education Inc., San Francisco, 3rd edition, 2010.

[2] K. Linderstrøm-Lang. *Proteins and enzymes*. Stanford university press, Stanford, CA, 1952.

[3] D. W. Ball, J. W. Hill, and R. J. Scott. *The Basics of General, Organic, and Biological Chemistry*. Flat World Knowledge, Irvington, NY, 1st edition, 2011.

[4] L. Mayne, S. W. Englander, R. Qiu, J. Yang, Y. Gong, E. J. Spek, and N. R. Kallenbach. Stabilizing effect of a multiple salt bridge in a prenucleated peptide. *Journal of the American Chemical Society*, 120(41):10643–10645, 1998.

[5] R. E. Hubbard and M. Kamran Haider. Hydrogen bonds in proteins: role and strength. *eLS*, 2010.

[6] S.-Y. Sheu, D.-Y. Yang, H. L. Selzle, and E. W. Schlag. Energetics of hydrogen bonds in peptides. *Proceedings of the National Academy of Sciences*, 100(22): 12683–12687, 2003.

[7] M. Matsumura, W. J. Becktel, M. Levitt, and B. W. Matthews. Stabilization of phage T4 lysozyme by engineered disulfide bonds. *Proceedings of the National Academy of Sciences*, 86(17):6562–6566, 1989.

[8] E. V Anslyn and D. A Dougherty. *Modern physical organic chemistry*. University Science Books, 2006.

[9] S. K. Burley and G. A. Petsko. Aromatic-aromatic interaction: a mechanism of protein structure stabilization. *Science*, 229(4708):23–28, 1985.

[10] M. H. F. Wilkins, A. R. Stokes, and H. R. Wilson. Molecular structure of nucleic acids: molecular structure of deoxypentose nucleic acids. *Nature*, 171(4356):738–740, 1953.

[11] R. E. Franklin and R. G. Gosling. Molecular configuration in sodium thymonucleate. *Nature*, 171:740–741, 1953.

[12] K. Wüthrich. Protein structure determination in solution by nuclear magnetic resonance spectroscopy. *Science*, 243(4887):45–50, 1989.

[13] R. Riek, S. Hornemann, G. Wider, M. Billeter, R. Glockshuber, and K. Wüthrich. NMR structure of the mouse prion protein domain prp (121-231). *Nature*, 382(6587):180–182, 1996.

[14] S. Raman, O. F. Lange, P. Rossi, M. Tyka, X. Wang, J. Aramini, G. Liu, T. A. Ramelot, A. Eletsky, T. Szyperski, et al. NMR structure determination for larger proteins using backbone-only data. *Science*, 327(5968):1014–1018, 2010.

[15] M. Baldassarre and A. Barth. Pushing the detection limit of infrared spectroscopy for structural analysis of dilute protein samples. *Analyst*, 139(21): 5393–5399, 2014.

[16] J. Kong and S. Yu. Fourier transform infrared spectroscopic analysis of protein secondary structures. *Acta Biochimica et Biophysica Sinica*, 39(8): 549–559, 2007.

[17] B. W. Caughey, A. Dong, K. S. Bhat, D. Ernst, S. F. Hayes, and W. S. Caughey. Secondary structure analysis of the scrapie-associated protein PrP 27-30 in water by infrared spectroscopy. *Biochemistry*, 30(31):7672–7680, 1991.

[18] M. R. Eftink. Fluorescence techniques for studying protein structure. *Methods of Biochemical Analysis: Protein Structure Determination*, 35:127–205, 1991.

[19] S. Nie and R. N. Zare. Optical detection of single molecules. *Annual review of biophysics and biomolecular structure*, 26(1):567–596, 1997.

[20] H. S. Chung, K. McHale, J. M. Louis, and W. A. Eaton. Single-molecule fluorescence experiments determine protein folding transition path times. *Science*, 335(6071):981–984, 2012.

[21] C. Louis-Jeune, M. A. Andrade-Navarro, and C. Perez-Iratxeta. Prediction of protein secondary structure from circular dichroism using theoretically derived spectra. *Proteins: Structure, Function, and Bioinformatics*, 80(2):374–381, 2012.

[22] N. Sreerama and R. W. Woody. Estimation of protein secondary structure from circular dichroism spectra: comparison of contin, selcon, and cdsstr methods with an expanded reference set. *Analytical biochemistry*, 287(2): 252–260, 2000.

[23] A. Huerta-Viga, S. R. Domingos, S. Amirjalayer, and S. Woutersen. A salt-bridge structure in solution revealed by 2D-IR spectroscopy. *Physical Chemistry Chemical Physics*, 16(30):15784–15786, 2014.

[24] K. C. Jones, C. S. Peng, and A. Tokmakoff. Folding of a heterogeneous β-hairpin peptide from temperature-jump 2D IR spectroscopy. *Proceedings of the National Academy of Sciences*, 110(8):2828–2833, 2013.

[25] A. M. Rijs, N. Sändig, M. N. Blom, J. Oomens, J. S Hannam, D. A. Leigh, F. Zerbetto, and W. J. Buma. Controlled hydrogen-bond breaking in a rotaxane by discrete solvation. *Angewandte Chemie*, 122(23):3988–3992, 2010.

[26] M. N. Blom, I. Compagnon, N. C. Polfer, G. von Helden, G. Meijer, S. Suhai, B. Paizs, and J. Oomens. Stepwise solvation of an amino acid: the appearance of zwitterionic structures. *The Journal of Physical Chemistry A*, 111(31): 7309–7316, 2007.

[27] M. A. Posthumus, P. G. Kistemaker, H. L. C. Meuzelaar, and M. C. Ten Noever de Brauw. Laser desorption-mass spectrometry of polar nonvolatile bio-organic molecules. *Analytical Chemistry*, 50(7):985–991, 1978.

[28] R. J. Levis. Laser desorption and ejection of biomolecules from the condensed phase into the gas phase. *Annual review of physical chemistry*, 45(1): 483–518, 1994.

[29] K. Markides and A. Gräslund. Advanced information on the nobel prize in chemistry 2002: Mass spectrometry (MS) and nuclear magnetic resonance (NMR) applied to biological macromolecules. URL `http://www.nobelprize.org/nobelprizes/chemistry/laureates/2002/advanced-chemistryprize2002.pdf`.

[30] T. Y. Samgina, E. A. Vorontsov, V. A. Gorshkov, K. A. Artemenko, R. A. Zubarev, and A. T. Lebedev. Mass spectrometric de novo sequencing of natural non-tryptic peptides: comparing peculiarities of collision-induced dissociation (CID) and high energy collision dissociation (HCD). *Rapid Communications in Mass Spectrometry*, 28(23):2595–2604, 2014.

[31] K. Biemann. Sequencing of peptides by tandem mass spectrometry and high-energy collision-induced dissociation. *Methods in enzymology*, 193: 455–479, 1990.

[32] H. Mizuno, T. K. Mal, K. I. Tong, R. Ando, T. Furuta, M. Ikura, and A. Miyawaki. Photo-induced peptide cleavage in the green-to-red conversion of a fluorescent protein. *Molecular cell*, 12(4):1051–1058, 2003.

[33] W. Gabryelski and L. Li. Photo-induced dissociation of electrospray generated ions in an ion trap/time-of-flight mass spectrometer. *Review of scientific instruments*, 70(11):4192–4199, 1999.

[34] J. R. Engen and D. L. Smith. Peer reviewed: Investigating protein structure and dynamics by hydrogen exchange ms. *Analytical chemistry*, 73(9):256A–265A, 2001.

[35] B. E. Winger, K. J. Light-Wahl, A. L. Rockwood, and R. D. Smith. Probing qualitative conformation differences of multiply protonated gas-phase proteins via hydrogen/deuterium isotopic exchange with water-d2. *Journal of the American Chemical Society*, 114(14):5897–5898, 1992.

[36] D. E. Clemmer, R. R. Hudgins, and M. F. Jarrold. Naked protein conformations: cytochrome c in the gas phase. *Journal of the American Chemical Society*, 117(40):10141–10142, 1995.

[37] C. S. Hoaglund-Hyzer, Y. J. Lee, A. E. Counterman, and D. E. Clemmer. Coupling ion mobility separations, collisional activation techniques, and multiple stages of ms for analysis of complex peptide mixtures. *Analytical chemistry*, 74(5):992–1006, 2002.

[38] T. S. Zwier. Laser spectroscopy of jet-cooled biomolecules and their water-containing clusters: Water bridges and molecular conformation. *The Journal of Physical Chemistry A*, 105(39):8827–8839, 2001.

[39] E. G. Robertson and J. P. Simons. Getting into shape: conformational and supramolecular landscapes in small biomolecules and their hydrated clusters. *Physical Chemistry Chemical Physics*, 3(1):1–18, 2001.

[40] T. R. Rizzo, Y. D. Park, and D. H. Levy. A molecular beam of tryptophan. *Journal of the American Chemical Society*, 107(1):277–278, 1985.

[41] F. Huisken, A. Kulcke, C. Laush, and J. M. Lisy. Dissociation of small methanol clusters after excitation of the O–H stretch vibration at 2.7 μ. *The Journal of chemical physics*, 95(6):3924–3929, 1991.

[42] W. Chin, J. P. Dognon, F. Piuzzi, B. Tardivel, I. Dimicoli, and M. Mons. Intrinsic folding of small peptide chains: Spectroscopic evidence for the formation of β-turns in the gas phase. *Journal of the American Chemical society*, 127(2):707–712, 2005.

[43] W. Chin, I. Compagnon, J.-P. Dognon, C. Canuel, F. Piuzzi, I. Dimicoli, G. von Helden, G. Meijer, and M. Mons. Spectroscopic evidence for gas-phase formation of successive β-turns in a three-residue peptide chain. *Journal of the American Chemical Society*, 127(5):1388–1389, 2005.

[44] W. Chin, J.-P. Dognon, C. Canuel, F. Piuzzi, I. Dimicoli, M. Mons, I. Compagnon, G. von Helden, and G. Meijer. Secondary structures of short peptide chains in the gas phase: Double resonance spectroscopy of protected dipeptides. *The Journal of chemical physics*, 122(5):054317, 2005.

[45] A. Abo-Riziq, J. E. Bushnell, B. Crews, M. Callahan, L. Grace, and M. S. De Vries. Gas phase spectroscopy of the pentapeptide fdasv. *Chemical physics letters*, 431(4):227–230, 2006.

[46] A. G. Abo-Riziq, B. O. Crews, M. P. Callahan, L. Grace, and M. S. de Vries. Spectroscopy of isolated gramicidin peptides. *Angewandte Chemie International Edition*, 45(31):5166–5169, 2006.

[47] P. Carcabal, R. A. Jockusch, I. Huenig, L. C. Snoek, R. T. Kroemer, B. G. Davis, D. P. Gamblin, I. Compagnon, J. Oomens, and J. P. Simons. Hydrogen bonding and cooperativity in isolated and hydrated sugars: Mannose, galactose, glucose, and lactose. *Journal of the American Chemical Society*, 127 (32):11414–11425, 2005.

[48] A. M. Rijs, G. Ohanessian, J. Oomens, G. Meijer, G. von Helden, and I. Compagnon. Internal proton transfer leading to stable zwitterionic structures in a neutral isolated peptide. *Angewandte Chemie International Edition*, 49 (13):2332–2335, 2010.

[49] V. A. Shubert and T. S. Zwier. IR-IR-UV Hole-burning: conformation specific IR spectra in the face of UV spectral overlap. *The Journal of Physical Chemistry A*, 111(51):13283–13286, 2007.

[50] A. Kantrowitz and J. Grey. A high intensity source for the molecular beam. part i. theoretical. *Review of Scientific Instruments*, 22(5):328–332, 1951.

[51] D. H. Levy. Laser spectroscopy of cold gas-phase molecules. *Annual Review of Physical Chemistry*, 31(1):197–225, 1980.

[52] R. J. Plowright, E. Gloaguen, and M. Mons. Compact folding of isolated four-residue neutral peptide chains: H-bonding patterns and entropy effects. *ChemPhysChem*, 12(10):1889–1899, 2011.

[53] P. D. Godfrey and R. D. Brown. Proportions of species observed in jet spectroscopy-vibrational energy effects: Histamine tautomers and conformers. *Journal of the American Chemical Society*, 120(41):10724–10732, 1998.

[54] G. T. Fraser, L.-H. Xu, R. D. Suenram, and C. L. Lugez. Rotational spectra of four of the five conformers of 1-pentene. *The Journal of Chemical Physics*, 112(14):6209–6217, 2000.

[55] E. Gloaguen, Y. Loquais, J. A. Thomas, D. W. Pratt, and M. Mons. Spontaneous formation of hydrophobic domains in isolated peptides. *The Journal of Physical Chemistry B*, 117(17):4945–4955, 2013.

[56] S.-i. Ishiuchi, H. Mitsuda, T. Asakawa, M. Miyazaki, and M. Fujii. Conformational reduction of dopa in the gas phase studied by laser desorption supersonic jet laser spectroscopy. *Physical Chemistry Chemical Physics*, 13 (17):7812–7820, 2011.

[57] V. A. Shubert, E. E. Baquero, J. R. Clarkson, W. H. James III, J. A. Turk, A. A. Hare, K. Worrel, M. A. Lipton, D. P. Schofield, K. D. Jordan, et al. Entropy-driven population distributions in a prototypical molecule with two flexible side chains: O-(2-acetamidoethyl)-n-acetyltyramine. *The Journal of chemical physics*, 127(23):234315, 2007.

[58] C. Cabezas, M. Varela, V. Cortijo, A. I. Jiménez, I. Peña, A. M. Daly, J. C. López, C. Cativiela, and J. L. Alonso. The alanine model dipeptide Ac-Ala-NH_2 exists as a mixture of $C_{eq}7$ and C5 conformers. *Physical Chemistry Chemical Physics*, 15(7):2580–2585, 2013.

[59] W. Chin, F. Piuzzi, I. Dimicoli, and M. Mons. Probing the competition between secondary structures and local preferences in gas phase isolated peptide backbones. *Physical Chemistry Chemical Physics*, 8(9):1033–1048, 2006.

[60] B. Yan, S. Jaeqx, W. J. van der Zande, and A. M. Rijs. A conformation-selective IR-UV study of the dipeptides Ac-Phe-Ser-NH_2 and Ac-Phe-Cys-NH_2: probing the SH$\cdots$O and OH$\cdots$O hydrogen bond interactions. *Physical Chemistry Chemical Physics*, 16(22):10770–10778, 2014.

[61] S. Jaeqx, J. Oomens, and A. M. Rijs. Gas-phase salt bridge interactions between glutamic acid and arginine. *Physical Chemistry Chemical Physics*, 15(38):16341–16352, 2013.

[62] M. D. Wheeler, S. M. Newman, A. J. Orr-Ewing, and M. N. R. Ashfold. Cavity ring-down spectroscopy. *Journal of the Chemical Society, Faraday Transactions*, 94(3):337–351, 1998.

[63] R. J. Conzemius and J. M. Capellen. A review of the applications to solids of the laser ion source in mass spectrometry. *International Journal of Mass Spectrometry and Ion Physics*, 34(3):197–271, 1980.

[64] M. L. Vestal. Ionization techniques for nonvolatile molecules. *Mass Spectrometry Reviews*, 2(4):447–480, 1983.

[65] G. Meijer, M. S. De Vries, H. E. Hunziker, and H. R. Wendt. Laser desorption jet-cooling of organic molecules. *Applied Physics B*, 51(6):395–403, 1990.

[66] D. H. Levy. The spectroscopy of very cold gases. *Science*, 214(4518):263–269, 1981.

[67] R. Tembreull and D. M. Lubman. Resonant two-photon ionization of small peptides using pulsed laser desorption in supersonic beam mass spectrometry. *Analytical Chemistry*, 59(7):1003–1006, 1987.

[68] J. Y. Zhang, D. S. Nagra, and L. Li. Molecular cooling and supersonic jet formation in laser desorption. *Analytical Chemistry*, 65(20):2812–2818, 1993.

[69] A. M. Rijs, B. O. Crews, M. S. de Vries, J. S. Hannam, D. A. Leigh, M. Fanti, F. Zerbetto, and W. J. Buma. Shaping of a conformationally flexible molecular structure for spectroscopy. *Angewandte Chemie International Edition*, 47(17):3174–3179, 2008.

[70] F. Hillenkamp, M. Karas, R. C. Beavis, and B. T. Chait. Matrix-assisted laser desorption/ionization mass spectrometry of biopolymers. *Analytical chemistry*, 63(24):1193A–1203A, 1991.

[71] A. Overberg, M. Karas, U. Bahr, R. Kaufmann, and F. Hillenkamp. Matrix-assisted infrared-laser (2.94 μm) desorption/ionization mass spectrometry of large biomolecules. *Rapid Communications in mass spectrometry*, 4(8):293–296, 1990.

[72] J. Sunner, E. Dratz, and Y. C. Chen. Graphite surface-assisted laser desorption/ionization time-of-flight mass spectrometry of peptides and proteins from liquid solutions. *Analytical chemistry*, 67(23):4335–4342, 1995.

[73] C. D. Mowry and M. V. Johnston. Internal energy of neutral molecules ejected by matrix-assisted laser desorption. *The Journal of Physical Chemistry*, 98(7):1904–1909, 1994.

[74] K. Dreisewerd. The desorption process in MALDI. *Chemical reviews*, 103 (2):395–426, 2003.

[75] B. B. Brady, L. A. Peteanu, and D. H. Levy. The electronic spectra of the pyrimidine bases uracil and thymine in a supersonic molecular beam. *Chemical physics letters*, 147(6):538–543, 1988.

[76] B. Friedrich, D. P. Pullman, and D. R. Herschbach. Alignment and orientation of rotationally cool molecules. *The Journal of Physical Chemistry*, 95(21): 8118–8129, 1991.

[77] H. L. Bethlem and G. Meijer. Production and application of translationally cold molecules. *International reviews in physical chemistry*, 22(1):73–128, 2003.

[78] M. S. Elioff, J. J. Valentini, and D. W. Chandler. Subkelvin cooling NO molecules via" billiard-like" collisions with argon. *Science*, 302(5652):1940–1943, 2003.

[79] S. Blanco, A. Lesarri, J. C. Lopez, and J. L. Alonso. The gas-phase structure of alanine. *Journal of the American Chemical Society*, 126(37):11675–11683, 2004.

[80] W. R. Gentry and C. F. Giese. Ten microsecond pulsed molecular beam source and a fast ionization detector. *Review of Scientific Instruments*, 49(5): 595–600, 1978.

[81] R. E. Smalley, L. Wharton, and D. H. Levy. Molecular optical spectroscopy with supersonic beams and jets. *Accounts of Chemical Research*, 10(4):139–145, 1977.

[82] A. Amirav, U. Even, and J. Jortner. Cooling of large and heavy molecules in seeded supersonic beams. *Chemical Physics*, 51(1):31–42, 1980.

[83] M. V. Johnston. Supersonic jet expansions in analytical spectroscopy. *TrAC Trends in Analytical Chemistry*, 3(2):58–61, 1984.

[84] N. P. Lockyer and J. C. Vickerman. Single photon ionization mass spectrometry using laser-generated vacuum ultraviolet photons. *Laser Chemistry*, 17:139–159, 1997.

[85] M. Schwell, H. W. Jochims, H. Baumgaertel, F. Dulieu, and S. Leach. VUV photochemistry of small biomolecules. *Planetary and Space Science*, 54(11): 1073–1085, 2006.

[86] R. Antoine and P. Dugourd. Visible and ultraviolet spectroscopy of gas phase protein ions. *Physical Chemistry Chemical Physics*, 13(37):16494–16509, 2011.

[87] L. C. Snoek, R. T. Kroemer, M. R. Hockridge, and J. P. Simons. Conformational landscapes of aromatic amino acids in the gas phase: Infrared and ultraviolet ion dip spectroscopy of tryptophan. *Physical Chemistry Chemical Physics*, 3(10):1819–1826, 2001.

[88] W. H. James, E. E. Baquero, V. A. Shubert, S. H. Choi, S. H. Gellman, and T. S. Zwier. Single-conformation and diastereomer specific ultraviolet and infrared spectroscopy of model synthetic foldamers: α/β-peptides. *Journal of the American Chemical Society*, 131(18):6574–6590, 2009.

[89] W. Y. Sohn, S. i. Ishiuchi, M. Miyazaki, J. Kang, S. Lee, A. Min, M. Choi, H. Kang, and M. Fujii. Conformationally resolved spectra of acetaminophen by UV-UV hole burning and IR dip spectroscopy in the gas phase. *Physical Chemistry Chemical Physics*, 15(3):957–964, 2013.

[90] T. S. Zwier. Laser probes of conformational isomerization in flexible molecules and complexes. *The Journal of Physical Chemistry A*, 110(12):4133–4150, 2006.

[91] V. A. Shubert, W. H. James, and T. S. Zwier. Jet-cooled electronic and vibrational spectroscopy of crown ethers: Benzo-15-crown-5 ether and 4'-amino-benzo-15-crown-5 ether. *The Journal of Physical Chemistry A*, 113(28), 2009.

[92] R. H. Page, Y. R. Shen, and Y.-T. Lee. Local modes of benzene and benzene dimer, studied by infrared-ultraviolet double resonance in a supersonic beam. *The Journal of Chemical Physics*, 88(8):4621–4636, 1988.

[93] R. N. Pribble and T. S. Zwier. Size-specific infrared spectra of benzene-(H_2O) n clusters (n= 1 through 7): evidence for noncyclic (H_2O) n structures. *Science*, 265(5168):75–79, 1994.

[94] J. M. Bakker, L. Mac Aleese, G. Meijer, and G. von Helden. Fingerprint ir spectroscopy to probe amino acid conformations in the gas phase. *Physical Review Letters*, 91(20):203003, 2003.

[95] E. J. Cocinero, P. Carcabal, T. D. Vaden, J. P. Simons, and B. G. Davis. Sensing the anomeric effect in a solvent-free environment. *Nature*, 469(7328):76–79, 2011.

[96] V. Hornak, R. Abel, A. Okur, B. Strockbine, A. Roitberg, and C. Simmerling. Comparison of multiple amber force fields and development of improved protein backbone parameters. *Proteins: Structure, Function, and Bioinformatics*, 65(3):712–725, 2006.

[97] W. D. Cornell, P. Cieplak, C. I. Bayly, I. R. Gould, K. M. Merz, D. M. Ferguson, D. C. Spellmeyer, T. Fox, J. W. Caldwell, and P. A. Kollman. A second generation force field for the simulation of proteins, nucleic acids, and organic molecules. *Journal of American Chemical Society*, 117(19):5179–5197, 1995.

[98] W. Kohn and L. J. Sham. Self-consistent equations including exchange and correlation effects. *Physical Review*, 140(4A):A1133, 1965.

[99] A. D. Becke. Density-functional thermochemistry. iii. the role of exact exchange. *The Journal of Chemical Physics*, 98(7):5648–5652, 1993.

[100] S. Grimme, J. Antony, T. Schwabe, and C. Mück-Lichtenfeld. Density functional theory with dispersion corrections for supramolecular structures, aggregates, and complexes of (bio) organic molecules. *Organic & biomolecular chemistry*, 5(5):741–758, 2007.

[101] S. Jaeqx. *Doctor thesis: Protein folding forces probed by infrared action spectroscopy*. Radboud University Nijmegen, Nijmegen, The Netherlands, 2014.

[102] J. B. Fenn, M. Mann, C. K. Meng, S. F. Wong, and C. M. Whitehouse. Electrospray ionization for mass spectrometry of large biomolecules. *Science*, 246:64–71, 1989.

[103] P. Kebarle and U. H. Verkerk. Electrospray: From ions in solution to ions in the gas phase, what we know now. *Mass Spectrometry Reviews*, 28(6): 898–917, 2009.

[104] R. E. March. Quadrupole ion trap mass spectrometer. In *Encyclopedia of Analytical Chemistry*. John Wiley & Sons, 2006. ISBN 9780470027318. doi: 10.1002/9780470027318.a6015.pub2. URL `http://dx.doi.org/10.1002/9780470027318.a6015.pub2`.

[105] R. O'Hair. The 3D quadrupole ion trap mass spectrometer as a complete chemical laboratory for fundamental gas-phase studies of metal mediated chemistry. *Chemical Communications*, (14):1469–1481, 2006.

[106] S. Gronert. Quadrupole ion trap studies of fundamental organic reactions. *Mass spectrometry reviews*, 24(1):100–120, 2005.

[107] Normalized Collision Energy Technology - Thermo Scientific Product Support Bulletin 104. URL `http://www.thermo.com/ms`.

[108] E.-L. Zins, C. Pepe, and D. Schroeder. Energy-dependent dissociation of benzylpyridinium ions in an ion-trap mass spectrometer. *Journal of Mass Spectrometry*, 45(11):1253–1260, NOV 2010.

[109] I. Compagnon and P. Dugourd. Energy-dependent kinetic method: Application to the multicompetitive fragmentation pathways of protonated peptides. *The Journal of Physical Chemistry A*, 111(42):10635–10639, 2007.

[110] U. Buck G. Scoles, D. Bassi and D. C. Laine. *Atomic and Molecular Beam Methods*. Oxford University Press, New York, 1989.

[111] R. C. Campargue. *Atomic and Molecular Beams: The State of the Art*. Springer, Berlin, 2001.

[112] O. F. Hagena and A. K. Varma. Time-of-flight velocity analysis of atomic and molecular beams. *Review of Scientific Instruments*, 39(1):47–52, 1968.

[113] K Bier and O Hagena. Optimum conditions for generating supersonic molecular beams. In *Rarefied Gas Dynamics, Volume 2*, volume 1, page 260, 1965.

[114] W. R. Gentry and C. F. Giese. Ten-microsecond pulsed molecular beam source and a fast ionization detector. *Review of Scientific Instruments*, 49(5): 595–600, 1978.

[115] J. B. Cross and J. J. Valentini. High repetition rate pulsed nozzle beam source. *Review of Scientific Instruments*, 53(1):38–42, 1982.

[116] P. Andresen, M. Faubel, D. Haeusler, G. Kraft, H. W. Luelf, and J. G. Skofronick. Characteristics of a piezoelectric pulsed nozzle beam. *Review of scientific instruments*, 56(11):2038–2042, 1985.

[117] D. Proch and T. Trickl. A high-intensity multi-purpose piezoelectric pulsed molecular beam source. *Review of Scientific Instruments*, 60(4):713–716, 1989.

[118] A. Flettner, J. Günther, M. B. Mason, U. Weichmann, R. Düren, and G. Gerber. High harmonic generation at 1 khz repetition rate with a pulsed valve. *Applied Physics B*, 73(2):129–132, 2001.

[119] L. Abad, D. Bermejo, V. J. Herrero, J. Santos, and I. Tanarro. Performance of a solenoid-driven pulsed molecular-beam source. *Review of scientific instruments*, 66(7):3826–3832, 1995.

[120] U. Even, J. Jortner, D. Noy, N. Lavie, and C. Cossart-Magos. Cooling of large molecules below 1 K and He clusters formation. *The Journal of Chemical Physics*, 112(18):8068–8071, 2000.

[121] M. Hillenkamp, S. Keinan, and U. Even. Condensation limited cooling in supersonic expansions. *The Journal of chemical physics*, 118(19):8699–8705, 2003.

[122] D. Irimia, D. Dobrikov, R. Kortekaas, H. Voet, D. A. van den Ende, W. A. Groen, and M. H. M. Janssen. A short pulse (7 μs fwhm) and high repetition rate (dc-5kHz) cantilever piezovalve for pulsed atomic and molecular beams. *Review of Scientific Instruments*, 80(11):113303, 2009.

[123] D. Irimia, R. Kortekaas, and M. H. M. Janssen. In situ characterization of a cold and short pulsed molecular beam by femtosecond ion imaging. *Physical Chemistry Chemical Physics*, 11(20):3958–3966, 2009.

[124] M. D. Barry, N. P. Johnson, and P. A. Gorry. A fast (30μs) pulsed supersonic nozzle beam source: application to the photodissociation of CS_2 at 193 nm. *Journal of Physics E: Scientific Instruments*, 19(10):815, 1986.

[125] K. Luria, W. Christen, and U. Even. Generation and propagation of intense supersonic beams. *The Journal of Physical Chemistry A*, 115(25):7362–7367, 2011.

[126] A. T. J. B. Eppink and D. H. Parker. Velocity map imaging of ions and electrons using electrostatic lenses: Application in photoelectron and photofragment ion imaging of molecular oxygen. *Review of Scientific Instruments*, 68(9):3477–3484, 1997.

[127] P. Jansen, D. W. Chandler, and K. E. Strecker. A compact molecular beam machine. *Review of Scientific Instruments*, 80(8):083105, 2009.

[128] A. Libson, M. Riedel, G. Bronshtein, E. Narevicius, U. Even, and M. G. Raizen. Towards coherent control of supersonic beams: a new approach to atom optics. *New Journal of Physics*, 8(5):77, 2006.

[129] M. C. Van Beek and J. J. Ter Meulen. An intense pulsed electrical discharge source for OH molecular beams. *Chemical physics letters*, 337(4):237–242, 2001.

[130] C. M. Western. Pgopher, a program for simulating rotational structure. *University of Bristol*, 7:108, 2010.

[131] O. Tkáč, A. K. Saha, J. Onvlee, C.-H. Yang, G. Sarma, C. K. Bishwakarma, S. Y. T. van de Meerakker, A. van der Avoird, D. H. Parker, and A. J. Orr-Ewing. State-to-state resolved differential cross sections for rotationally inelastic scattering of ND_3 with He. *Physical Chemistry Chemical Physics*, 16 (2):477–488, 2014.

[132] A. von Zastrow, J. Onvlee, S. N. Vogels, G. C. Groenenboom, A. van der Avoird, and S. Y. T. van de Meerakker. State-resolved diffraction oscillations imaged for inelastic collisions of NO radicals with He, Ne and Ar. *Nature chemistry*, 6(3):216–221, 2014.

[133] J. Onvlee, S. N. Vogels, A. von Zastrow, D. H. Parker, and S. Y. T. van de Meerakker. Molecular collisions coming into focus. *Physical Chemistry Chemical Physics*, 16(30):15768–15779, 2014.

[134] L. Stryer, J. L. Tymoczko, and J. M. Berg. *Biochemistry*. Freeman, New York, 5th edition, 2002.

[135] T. Steiner and G. Koellner. Hydrogen bonds with pi-acceptors in proteins: Frequencies and role in stabilizing local 3D structures. *Journal of Molecular Biology*, 305(3):535–557, 2001.

[136] A. G. Abo-Riziq, L. Grace, B. Crews, M. P. Callahan, T. van Mourik, and M. S. de Vries. Conformational structure of tyrosine, tyrosyl-glycine, and tyrosyl-glycyl-glycine by double resonance spectroscopy. *The Journal of Physical Chemistry A*, 115(23):6077–6087, 2011.

[137] G. Von Helden, I. Compagnon, M. N. Blom, M. Frankowski, U. Erlekam, J. Oomens, B. Brauer, R. B. Gerber, and G. Meijer. Mid-IR spectra of different conformers of phenylalanine in the gas phase. *Physical Chemistry Chemical Physics*, 10(9):1248–1256, 2008.

[138] R. Linder, K. Seefeld, A. Vavra, and K. Kleinermanns. Gas phase infrared spectra of nonaromatic amino acids. *Chemical Physics Letters*, 453(1):1–6, 2008.

[139] T. Häber, K. Seefeld, G. Engler, S. Grimme, and K. Kleinermanns. IR/UV spectra and quantum chemical calculations of Trp–Ser: Stacking interactions between backbone and indole side-chain. *Physical Chemistry Chemical Physics*, 10(19):2844–2851, 2008.

[140] H. Valdes, V. Spiwok, J. Rezac, D. Reha, A. G. Abo-Riziq, M. S. de Vries, and P. Hobza. Potential-energy and free-energy surfaces of glycyl-phenylalanyl-alanine (GFA) tripeptide: Experiment and theory. *Chemistry-A European Journal*, 14(16):4886–4898, 2008.

[141] A. M. Rijs, G. Ohanessian, J. Oomens, G. Meijer, G. Von Helden, and I. Compagnon. Internal proton transfer leading to stable zwitterionic structures in a neutral isolated peptide. *Angewandte Chemie International Edition*, 49 (13):2332–2335, 2010.

[142] E. J. Cocinero, P. Çarçabal, T. D. Vaden, J. P. Simons, and B. G. Davis. Sensing the anomeric effect in a solvent-free environment. *Nature*, 469(7328):76–79, 2011.

[143] E. Aguado, I. León, J. Millán, E. J. Cocinero, S. Jaeqx, A. M. Rijs, A. Lesarri, and J. Fernández. Unraveling the benzocaine–receptor interaction at molecular level using mass-resolved spectroscopy. *The Journal of Physical Chemistry B*, 117(43):13472–13480, 2013.

[144] J. C. Dean, E. G. Buchanan, and T. S. Zwier. Mixed 14/16 helices in the gas phase: Conformation-specific spectroscopy of Z-(Gly) n, n= 1, 3, 5. *Journal of American Chemical Society*, 134(41):17186–17201, 2012.

[145] K. Schwing, H. Fricke, K. Bartl, J. Polkowska, T. Schrader, and M. Gerhards. Isolated β-turn model systems investigated by combined IR/UV spectroscopy. *ChemPhysChem*, 13(6):1576–1582, 2012.

[146] E. M. Tan, S. Amirjalayer, S. Smolarek, A. Vdovin, A. M. Rijs, and W. J. Buma. Conformational heterogeneity of methyl 4-hydroxycinnamate: A gas-phase UV–IR spectroscopic study. *The Journal of Physical Chemistry B*, 117(17):4798–4805, 2013.

[147] Z. Gengeliczki, M. P. Callahan, M. Kabelác, A. M. Rijs, and M. S. de Vries. Structure of 2, 4-diaminopyrimidine–theobromine alternate base pairs. *The Journal of Physical Chemistry A*, 115(41):11423–11427, 2011.

[148] Y. Shimozono, K. Yamada, S. Ishiuchi, K. Tsukiyama, and M. Fujii. Revised conformational assignments and conformational evolution of tyrosine by laser desorption supersonic jet laser spectroscopy. *Physical Chemistry Chemical Physics*, 15(14):5163–5175, 2013.

[149] V. Brenner, F. Piuzzi, I. Dimicoli, B. Tardivel, and M. Mons. Spectroscopic evidence for the formation of helical structures in gas-phase short peptide chains. *The Journal of Physical Chemistry A*, 111(31):7347–7354, 2007.

[150] W. Chin, M. Mons, J. P. Dognon, F. Piuzzi, B. Tardivel, and I. Dimicoli. Competition between local conformational preferences and secondary structures in gas-phase model tripeptides as revealed by laser spectroscopy and theoretical chemistry. *Physical Chemistry Chemical Physics*, 6(10):2700–2709, 2004.

[151] E. Gloaguen, F. Pagliarulo, V. Brenner, W. Chin, F. Piuzzi, B. Tardivel, and M. Mons. Intramolecular recognition in a jet-cooled short peptide chain: γ-turn helicity probed by a neighbouring residue. *Physical Chemistry Chemical Physics*, 9(32):4491–4497, 2007.

[152] W. Chin, F. Piuzzi, J. P. Dognon, I. Dimicoli, and M. Mons. Gas-phase models of γ turns: Effect of side-chain/backbone interactions investigated by IR/UV spectroscopy and quantum chemistry. *The Journal of chemical physics*, 123(8):084301, 2005.

[153] R. J. Lavrich, D. F. Plusquellic, R. D. Suenram, G. T. Fraser, A. R. Walker, and M. J. Tubergen. Experimental studies of peptide bonds: Identification of the C7eq conformation of the alanine dipeptide analog N-acetyl-alanine N'-methylamide from torsion-rotation interactions. *Journal of Chemical Physics*, 118:1253–1265, 2003.

[154] I. Compagnon, J. Oomens, J. Bakker, G. Meijer, and G. von Helden. Vibrational spectroscopy of a non-aromatic amino acid-based model peptide: identification of the γ-turn motif of the peptide backbone. *Physical Chemistry Chemical Physics*, 7(1):13–15, 2005.

[155] B. C. Dian, A. Longarte, and T. S. Zwier. Conformational dynamics in a dipeptide after single-mode vibrational excitation. *Science*, 296(5577): 2369–2373, 2002.

[156] G. A. Chass, S. Lovas, R. F. Murphy, and I. G. Csizmadia. The role of enhanced aromatic-electron donating aptitude of the tyrosyl sidechain with respect to that of phenylalanyl in intramolecular interactions. *The European Physical Journal D-Atomic, Molecular, Optical and Plasma Physics*, 20(3):481–497, 2002.

[157] E. Gloaguen, H. Valdes, F. Pagliarulo, R. Pollet, B. Tardivel, P. Hobza, F. Piuzzi, and M. Mons. Experimental and theoretical investigation of the aromatic- aromatic interaction in isolated capped dipeptides. *The Journal of Physical Chemistry A*, 114(9):2973–2982, 2009.

[158] H. S. Biswal, E. Gloaguen, Y. Loquais, B. Tardivel, and M. Mons. Strength of NH···S hydrogen bonds in methionine residues revealed by gas-phase IR/UV spectroscopy. *The Journal of Physical Chemistry Letters*, 3(6):755–759, 2012.

[159] A. M. Rijs, E. R. Kay, D. A. Leigh, and W. J. Buma. IR spectroscopy on jet-cooled isolated two-station rotaxanes. *The Journal of Physical Chemistry A*, 115(34):9669–9675, 2011.

[160] P. M. Johnson and C. E. Otis. Molecular multiphoton spectroscopy with ionization detection. *Annual Review of Physical Chemistry*, 32(1):139–157, 1981.

[161] H. Zhu, M. Blom, I. Compagnon, A. M. Rijs, S. Roy, G. von Helden, and B. Schmidt. Conformations and vibrational spectra of a model tripeptide: change of secondary structure upon micro-solvation. *Physical Chemistry Chemical Physics*, 12(14):3415–3425, 2010.

[162] D. Oepts, A. Van der Meer, and P. Van Amersfoort. The free-electron-laser user facility felix. *Infrared Physics & Technology*, 36(1):297–308, 1995.

[163] S. Jaeqx, W. Du, E. J. Meijer, J. Oomens, and A. M. Rijs. Conformational study of Z-Glu-OH and Z-Arg-OH: dispersion interactions versus conventional hydrogen bonding. *The Journal of Physical Chemistry A*, 117(6): 1216–1227, 2012.

[164] B. Hess, C. Kutzner, D. Van Der Spoel, and E. Lindahl. Gromacs 4: Algorithms for highly efficient, load-balanced, and scalable molecular simulation. *Journal of chemical theory and computation*, 4(3):435–447, 2008.

[165] M. J. Frisch, G. W. Trucks, H. B. Schlegel, G. E. Scuseria, M. A. Robb, J. R. Cheeseman, G. Scalmani, V. Barone, B. Mennucci, G. A. Petersson, H. Nakatsuji, M. Caricato, H. P. Hratchian X. Li, A. F. Izmaylov, J. Bloino, G. Zheng, J. L. Sonnenberg, M. Hada, M. Ehara, K. Toyota, R. Fukuda, J. Hasegawa, M. Ishida, T. Nakajima, Y. Honda, O. Kitao, H. Nakai, T. Vreven, Jr. J. A. Montgomery, J. E. Peralta, F. Ogliaro, M. Bearpark, J. J. Heyd, E. Brothers, K. N. Kudin, V. N. Staroverov, R. Kobayashi, J. Normand, K. Raghavachari, A. Rendell, J. C. Burant, S. S. Iyengar, J. Tomasi, M. Cossi, N. Rega, J. M. Millam, M. Klene, J. E. Knox, J. B. Cross, V. Bakken, C. Adamo, J. Jaramillo, R. Gomperts, R. E. Stratmann, O. Yazyev, A. J. Austin, R. Cammi, C. Pomelli, J. W. Ochterski, R. L. Martin, K. Morokuma, V. G. Zakrzewski, G. A. Voth, P. Salvador, J. J. Dannenberg, S. Dapprich, A. D. Daniels, Ö. Farkas, J. B. Foresman, J. V. Ortiz, J. Cioslowski, and D. J. Fox. Gaussian 09, revision a.1, 2009.

[166] A. Šarić, T. Hrenar, M. Mališ, and N. Došlić. Quantum mechanical study of secondary structure formation in protected dipeptides. *Physical Chemistry Chemical Physics*, 12(18):4678–4685, 2010.

[167] F. Jensen. *Introduction to Computational Chemistry*. John Wiley & Sons, Ltd, Chichester, 2nd edition, 2007. ISBN 0-470-01186-6.

[168] L. A. Curtiss and M. S. Gordon. *Computational materials chemistry: Methods and applications*. Springer Science & Business Media, 2004.

[169] A. G. Abo-Riziq, B. Crews, J. E. Bushnell, M. P. Callahan, and M. S. De Vries. Conformational analysis of cyclo (Phe-Ser) by UV–UV and IR–UV double resonance spectroscopy and ab initio calculations. *Molecular Physics*, 103 (11-12):1491–1495, 2005.

[170] J. C. Dobrowolski, M. H. Jamróz, R. Kołos, J. E Rode, and J. Sadlej. Theoretical prediction and the first IR matrix observation of several L-cysteine molecule conformers. *ChemPhysChem*, 8(7):1085–1094, 2007.

[171] M. E. Sanz, S. Blanco, J. C. López, and J. L. Alonso. Rotational probes of six conformers of neutral cysteine. *Angewandte Chemie International Edition*, 47 (33):6216–6220, 2008.

[172] L. C. Snoek, R. T. Kroemer, and J. P. Simons. A spectroscopic and computational exploration of tryptophan–water cluster structures in the gas phase. *Physical Chemistry Chemical Physics*, 4(11):2130–2139, 2002.

[173] S. Campbell, M. T. Rodgers, E. M. Marzluff, and J. L. Beauchamp. Deuterium exchange reactions as a probe of biomolecule structure. fundamental studies of gas phase H/D exchange reactions of protonated glycine oligomers with D_2O, CD_3OD, CD_3CO_2D, and ND_3. *Journal of the American Chemical Society*, 117(51):12840–12854, 1995.

[174] O. P. Balaj, D. Semrouni, V. Steinmetz, E. Nicol, C. Clavaguéra, and G. Ohanessian. Structure of sodiated polyglycines. *Chemistry-A European Journal*, 18(15):4583–4592, 2012.

[175] N. C. Polfer, B. Paizs, L. C. Snoek, I. Compagnon, S. Suhai, G. Meijer, G. von Helden, and J. Oomens. Infrared fingerprint spectroscopy and theoretical studies of potassium ion tagged amino acids and peptides in the gas phase. *Journal of the American Chemical Society*, (23):8571–8579, 2005.

[176] N. C. Polfer, J. Oomens, and R. C. Dunbar. Alkali metal complexes of the dipeptides PheAla and AlaPhe: IRMPD spectroscopy. *ChemPhysChem*, 9(4):579–589, 2008.

[177] J. S. Prell, J. T. O'Brien, J. D. Steill, J. Oomens, and E. R. Williams. Structures of protonated dipeptides: the role of arginine in stabilizing salt bridges. *Journal of the American Chemical Society*, 131(32):11442–11449, 2009.

[178] E. Pluhařová, O. Marsalek, B. Schmidt, and P. Jungwirth. Peptide salt bridge stability: From gas phase via microhydration to bulk water simulations. *The Journal of chemical physics*, 137(18):185101, 2012.

[179] B. J. Bythell, I. P. Csonka, S. Suhai, D. F. Barofsky, and B. Paizs. Gas-phase structure and fragmentation pathways of singly protonated peptides with n-terminal arginine. *The Journal of Physical Chemistry B*, 114(46):15092–15105, 2010.

[180] Y. Sugita and Y. Okamoto. Molecular mechanism for stabilizing a short helical peptide studied by generalized-ensemble simulations with explicit solvent. *Biophysical journal*, 88(5):3180–3190, 2005.

[181] A. Okur, L. Wickstrom, and C. Simmerling. Evaluation of salt bridge structure and energetics in peptides using explicit, implicit, and hybrid solvation models. *Journal of Chemical Theory and Computation*, 4(3):488–498, 2008.

[182] J. Yang, J. Wu, J. M. Steichen, A. P. Kornev, M. S. Deal, S. Li, B. Sankaran, V. L. Woods Jr, and S. S. Taylor. A conserved Glu–Arg salt bridge connects coevolved motifs that define the eukaryotic protein kinase fold. *Journal of molecular biology*, 415(4):666–679, 2012.

[183] H. Kuroyanagi, Y. Watanabe, and M. Hagiwara. CELF family RNA–binding protein UNC-75 regulates two sets of mutually exclusive exons of the unc-32 gene in neuron-specific manners in caenorhabditis elegans. *PLoS genetics*, 9(2):e1003337, 2013.

[184] M. Dittrich, S. Hayashi, and K. Schulten. ATP hydrolysis in the β-TP and β-DP catalytic sites of F1-ATPase. *Biophysical journal*, 87(5):2954–2967, 2004.

[185] E. Kaiser, R. L. Colescott, C. D. Bossinger, and P. I. Cook. Completion of the coupling reaction was monitored by the kaiser test. *Analytical Biochemistry*, 34:595–598, 1970.

[186] A. L. Nicely, D. J. Miller, and J. M. Lisy. Charge and temperature dependence of biomolecule conformations: K^+ Tryptamine $(H_2O)_{n=0-1}Ar_{m=0-1}$ Cluster Ions. *Journal of the American Chemical Society*, 131(18):6314–6315, 2009.

[187] C. N. Stedwell, J. F. Galindo, K. Gulyuz, A. E. Roitberg, and N. C. Polfer. Crown complexation of protonated amino acids: influence on IRMPD spectra. *The Journal of Physical Chemistry A*, 117(6):1181–1188, 2012.

[188] E. Gloaguen, B. De Courcy, J.-P. Piquemal, J. Pilmé, O. Parisel, R. Pollet, H. S. Biswal, F. Piuzzi, B. Tardivel, M. Broquier, et al. Gas-phase folding of a two-residue model peptide chain: On the importance of an interplay between experiment and theory. *Journal of the American Chemical Society*, 132(34):11860–11863, 2010.

[189] M. S. de Vries and P. Hobza. Gas-phase spectroscopy of biomolecular building blocks. *Annu. Rev. Phys. Chem.*, 58:585–612, 2007.

[190] A. M. Rijs, I. Compagnon, J. Oomens, J. S. Hannam, D. A. Leigh, and W. J. Buma. Stiff, and sticky in the right places: Binding interactions in isolated mechanically interlocked molecules probed by mid-infrared spectroscopy. *Journal of the American Chemical Society*, 131(7):2428–2429, 2009.

[191] J. M. Bakker, C. Plützer, I. Hünig, T. Häber, I. Compagnon, G. von Helden, G. Meijer, and K. Kleinermanns. Folding structures of isolated peptides as revealed by gas-phase mid-infrared spectroscopy. *ChemPhysChem*, 6(1): 120–128, 2005.

[192] T. D. Vaden, S. A. N. Gowers, and L. C. Snoek. Infrared spectroscopy of forbidden peptide sequences. *Physical Chemistry Chemical Physics*, 11(27): 5843–5850, 2009.

[193] T. Watanabe, T. Ebata, S. Tanabe, and N. Mikami. Size-selected vibrational spectra of phenol-(H_2O) n (n= 1–4) clusters observed by IR–UV double resonance and stimulated Raman-UV double resonance spectroscopies. *The Journal of chemical physics*, 105(2):408–419, 1996.

[194] D. Pal and P. Chakrabarti. Cis peptide bonds in proteins: residues involved, their conformations, interactions and locations. *Journal of molecular biology*, 294(1):271–288, 1999.

[195] R. K. Soong, G. D. Bachand, H. P. Neves, A. G. Olkhovets, H. G. Craighead, and C. D. Montemagno. Powering an inorganic nanodevice with a biomolecular motor. *Science*, 290(5496):1555–1558, 2000.

[196] H. Liu, J. J. Schmidt, G. D. Bachand, S. S. Rizk, L. L. Looger, H. W. Hellinga, and C. D. Montemagno. Control of a biomolecular motor-powered nanodevice with an engineered chemical switch. *Nature materials*, 1(3):173–177, 2002.

[197] T. Fischer, A. Agarwal, and H. Hess. A smart dust biosensor powered by kinesin motors. *Nature Nanotechnology*, 4(3):162–166, 2009.

[198] S. Wilkens, F. W. Dahlquist, L. P. McIntosh, L. W. Donaldson, and R. A. Capaldi. Structural features of the ϵ subunit of the Escherichia coli ATP synthase determined by NMR spectroscopy. *Nature Structural & Molecular Biology*, 2(11):961–967, 1995.

[199] L. K. Lee, A. G. Stewart, M. Donohoe, R. A. Bernal, and D. Stock. The structure of the peripheral stalk of Thermus thermophilus H^+-ATPase/synthase. *Nature structural & molecular biology*, 17(3):373–378, 2010.

[200] J. P. Abrahams, A. G. Leslie, R. Lutter, and J. E. Walker. Structure at 2.8 Å resolution of F1-ATPase from bovine heart mitochondria. *Nature*, (370): 621–628, 1994.

[201] W. Kühlbrandt, J. Zeelen, and J. Dietrich. Structure, mechanism, and regulation of the neurospora plasma membrane H^+-ATPase. *Science*, 297(5587): 1692–1696, 2002.

[202] J. Zimmer, Y. Nam, and T. A. Rapoport. Structure of a complex of the ATPase SecA and the protein-translocation channel. *Nature*, 455(7215): 936–943, 2008.

[203] T. Masaike, F. Koyama-Horibe, K. Oiwa, M. Yoshida, and T. Nishizaka. Cooperative three-step motions in catalytic subunits of F1-ATPase correlate with 80 and 40 substep rotations. *Nature structural & molecular biology*, 15 (12):1326–1333, 2008.

[204] K. Adachi, K. Oiwa, M. Yoshida, T. Nishizaka, and K. Kinosita Jr. Controlled rotation of the F1-ATPase reveals differential and continuous binding changes for ATP synthesis. *Nature communications*, 3:1022, 2012.

[205] H. Noji, R. Yasuda, M. Yoshida, and K. Kinosita. Direct observation of the rotation of F1-ATPase. *Nature*, 386(6622):299–302, 1997.

[206] R. Yasuda, H. Noji, K. Kinosita, and M. Yoshida. F1-ATPase is a highly efficient molecular motor that rotates with discrete 120 steps. *Cell*, 93(7): 1117–1124, 1998.

[207] J. Hogan. Molecular microscopy: Focus on the living. *Nature*, 440(7080): 14–15, 2006.

[208] A. D. Mehta, R. S. Rock, M. Rief, J. A. Spudich, M. S. Mooseker, and R. E. Cheney. Myosin-v is a processive actin-based motor. *Nature*, 400(6744): 590–593, 1999.

[209] T. Uchihashi, R. Iino, T. Ando, and H. Noji. High-speed atomic force microscopy reveals rotary catalysis of rotorless F1-ATPase. *Science*, 333 (6043):755–758, 2011.

[210] P. D. Boyer. Atp synthase-past and future. *Biochimica et Biophysica Acta (BBA)-Bioenergetics*, 1365(1):3–9, 1998.

[211] S. Furuike, M. D. Hossain, Y. Maki, K. Adachi, T. Suzuki, A. Kohori, H. Itoh, M. Yoshida, and K. Kinosita. Axle-less F1-ATPase rotates in the correct direction. *Science*, 319(5865):955–958, 2008.

[212] H. Noji. The rotary enzyme of the cell: the rotation of F1-ATPase. *Science*, 282(5395):1844–1845, 1998.

[213] M. Zhao, S. Wu, Q. Zhou, S. Vivona, D. J. Cipriano, Y. Cheng, and A. T. Brunger. Mechanistic insights into the recycling machine of the snare complex. *Nature*, 518(7537):61–67, 2015.

[214] H. Itoh, A. Takahashi, K. Adachi, H. Noji, R. Yasuda, M. Yoshida, and K. Kinosita. Mechanically driven ATP synthesis by F1-ATPase. *Nature*, 427 (6973):465–468, 2004.

[215] P. Mitchell. Coupling of phosphorylation to electron and hydrogen transfer by a chemi-osmotic type of mechanism. *Nature*, 191(4784):144–148, 1961.

[216] P. Mitchell. A chemiosmotic molecular mechanism for proton-translocating adenosine triphosphatases. *FEBS letters*, 43(2):189–194, 1974.

[217] P. D. Boyer. A model for conformational coupling of membrane potential and proton translocation to atp synthesis and to active transport. *FEBS letters*, 58(1):1–6, 1975.

[218] P. D. Boyer, R. L. Cross, and W. Momsen. A new concept for energy coupling in oxidative phosphorylation based on a molecular explanation of the oxygen exchange reactions. *Proceedings of the National Academy of Sciences*, 70(10):2837–2839, 1973.

[219] C. Montemagno and G. Bachand. Constructing nanomechanical devices powered by biomolecular motors. *Nanotechnology*, 10(3):225, 1999.

[220] Q. Ren, Y.-P. Zhao, J. C. Yue, and Y. B. Cui. Biological application of multi-component nanowires in hybrid devices powered by F1-ATPase motors. *Biomedical microdevices*, 8(3):201–208, 2006.

[221] V. Balzani, A. Credi, and M. Venturi. Molecular machines working on surfaces and at interfaces. *ChemPhysChem*, 9(2):202–220, 2008.

[222] X. Bi, R. A. Corpina, and J. Goldberg. Structure of the Sec23/24–Sar1 pre-budding complex of the COPII vesicle coat. *Nature*, 419(6904):271–277, 2002.

[223] S. Nadanaciva, J. Weber, S. Wilke-Mounts, and A. E. Senior. Importance of F1-ATPase residue α-Arg-376 for catalytic transition state stabilization. *Biochemistry*, 38(47):15493–15499, 1999.

[224] L. M. S. Elles and O. C. Uhlenbeck. Mutation of the arginine finger in the active site of escherichia coli DbpA abolishes ATPase and helicase activity and confers a dominant slow growth phenotype. *Nucleic acids research*, 36 (1):41–50, 2008.

[225] Y. Komoriya, T. Ariga, R. Iino, H. Imamura, D. Okuno, and H. Noji. Principal role of the arginine finger in rotary catalysis of F1-ATPase. *Journal of Biological Chemistry*, 287(18):15134–15142, 2012.

[226] S. Hayashi, H. Ueno, A. R. Shaikh, M. Umemura, M. Kamiya, Y. Ito, M. Ikeguchi, Y. Komoriya, R. Iino, and H. Noji. Molecular mechanism of atp hydrolysis in F1-ATPase revealed by molecular simulations and single-molecule observations. *Journal of the American Chemical Society*, 134 (20):8447–8454, 2012.

[227] X. Pan, S. Eathiraj, M. Munson, and D. G. Lambright. TBC-domain GAPs for Rab GTPases accelerate GTP hydrolysis by a dual-finger mechanism. *Nature*, 442(7100):303–306, 2006.

[228] H. Resat, T. Straatsma, D. A. Dixon, and J. H. Miller. The arginine finger of RasGAP helps Gln-61 align the nucleophilic water in GAP-stimulated hydrolysis of GTP. *Proceedings of the National Academy of Sciences*, 98(11): 6033–6038, 2001.

[229] J. Sun, E. N. Kitova, W. Wang, and J. S. Klassen. Method for distinguishing specific from nonspecific protein-ligand complexes in nanoelectrospray ionization mass spectrometry. *Analytical chemistry*, 78(9):3010–3018, 2006.

[230] W. Wang, E. N. Kitova, and J. S. Klassen. Influence of solution and gas phase processes on protein-carbohydrate binding affinities determined by nanoelectrospray fourier transform ion cyclotron resonance mass spectrometry. *Analytical chemistry*, 75(19):4945–4955, 2003.

[231] P. Carçabal, R. A. Jockusch, I. Hünig, L. C. Snoek, R. T. Kroemer, B. G. Davis, D. P. Gamblin, I. Compagnon, J. Oomens, and J. P. Simons. Hydrogen bonding and cooperativity in isolated and hydrated sugars: mannose, galactose, glucose, and lactose. *Journal of the American Chemical Society*, 127 (32):11414–11425, 2005.

[232] S. A. Hofstadler and K. A. Sannes-Lowery. Applications of ESI-MS in drug discovery: interrogation of noncovalent complexes. *Nature Reviews Drug Discovery*, 5(7):585–595, 2006.

[233] L. M. Young, J. C. Saunders, R. A. Mahood, C. H. Revill, R. J. Foster, L. Tu, D. P. Raleigh, S. E. Radford, and A. E. Ashcroft. Screening and classifying small-molecule inhibitors of amyloid formation using ion mobility spectrometry–mass spectrometry. *Nature chemistry*, 7(1):73–81, 2015.

[234] C Uetrecht and A. Heck. Modern biomolecular mass spectrometry and its role in studying virus structure, dynamics, and assembly. *Angewandte Chemie International Edition*, 50(36):8248–8262, 2011.

[235] F. H. Cederkvist, A. D. Zamfir, S. Bahrke, V. G. H. Eijsink, M. Sørlie, J. Peter-Katalinić, and M. G. Peter. Identification of a high-affinity-binding oligosaccharide by (+) nanoelectrospray quadrupole time-of-flight tandem mass spectrometry of a noncovalent enzyme–ligand complex. *Angewandte Chemie International Edition*, 45(15):2429–2434, 2006.

[236] Nelson D. L. and Cox M. M. *Principles of Biochemistry*. WH Freeman, New York, 2008.

[237] M. M. Deshmukh and S. R. Gadre. Estimation of N-H$\cdots$O=C intramolecular hydrogen bond energy in polypeptides. *The Journal of Physical Chemistry A*, 113(27):7927–7932, 2009.

[238] G. L. Orriss, A. G. W. Leslie, K. Braig, and J. E. Walker. Bovine F1-ATPase covalently inhibited with 4-chloro-7-nitrobenzofurazan: the structure provides further support for a rotary catalytic mechanism. *Structure*, 6(7):831–837, 1998.

[239] M. A. Bianchet, J. Hullihen, P. L. Pedersen, and L. M. Amzel. The 2.8-Å structure of rat liver F1-ATPase: configuration of a critical intermediate in ATP synthesis/hydrolysis. *Proceedings of the National Academy of Sciences*, 95 (19):11065–11070, 1998.

[240] C. Gibbons, M. G. Montgomery, A. G. W. Leslie, and J. E. Walker. The structure of the central stalk in bovine F1-ATPase at 2.4 Å resolution. *Nature Structural & Molecular Biology*, 7(11):1055–1061, 2000.

[241] R. I. Menz, A. G. W. Leslie, and J. E. Walker. The structure and nucleotide occupancy of bovine mitochondrial F1-ATPase are not influenced by crystallisation at high concentrations of nucleotide. *FEBS letters*, 494(1):11–14, 2001.

[242] R. M. Burke, J. K. Pearce, W. E. Boxford, A. Bruckmann, and C. E. H. Dessent. Stabilization of excess charge in isolated adenosine 5′-triphosphate and adenosine 5′-diphosphate multiply and singly charged anions. *The Journal of Physical Chemistry A*, 109(43):9775–9785, 2005.

Publications

Publications of the work described in this thesis:

[1] **Bin Yan**, Peter F.H. Claus, Bas G.M. van Oorschot, Leander Gerritsen, Andre T.J.B. Eppink, Sebastiaan Y.T. van de Meerakker and David H. Parker
Review of Scientific Instruments **84(2)**, 023102 (2013)
"A new high intensity and short-pulse molecular beam valve"
Chapter 3 of this thesis

[2] **Bin Yan**, Sander Jaeqx, Wim J. van der Zande and Anouk M. Rijs
Physical Chemistry Chemical Physics **16(22)**, 10770 (2014)
"A conformation-selective IR-UV study of the dipeptides Ac-Phe-Ser-NH_2 and Ac-Phe-Cys-NH_2: probing the $SH\cdots O$ and $OH\cdots O$ hydrogen bond interactions"
Chapter 4 of this thesis

[3] **Bin Yan**, Sjors Bakels, Robbert C. Ouwersloot, Dennis W. P. M. Löwik and Anouk M. Rijs
Submitted to *Physical Chemistry Chemical Physics*
"Zwitterionic interactions in gas phase neutral peptides: The effect of the backbone rigidity on the salt bridge formation"
Chapter 5 of this thesis

[4] **Bin Yan**, Koen K.W. van Asseldonk, Baptiste Schindler, Isabelle Compagnon and Anouk M. Rijs
In preparation
"Exploring ATP hydrolysis on the molecular level: ion trap mass spectrometry study of ATP binding with ATPase active site "
Chapter 6 of this thesis

Other publications:

[1] Zahid Farooq, Dimitri A. Chestakov, **Bin Yan**, Gerrit C. Groenenboom, Wim J. van der Zande and David H. Parker
Physical Chemistry Chemical Physics **16(7)**, 3305 (2014)
"Photodissociation of singlet oxygen in the UV region"

Acknowledgements

At the end, I would like to express my sincere acknowledgements to some people without the help of whom I could not finish my thesis.

First, I want to thank Dr. Anouk M. Rijs, my Phd 2nd phase (since Sep. 2012) daily supervisor. Anouk, I still remember the first time we met when I visited you in Rijnhuizen. You were performing experiments in the lab and you introduced me your setup (which I would use later to obtain many great results) very patiently. After that, I met you several times at conferences, although I did not know yet that you would become my supervisor. When it happened, I felt very confused (upset to leave the previous lab and exciting to start a new challenge). However, after a short time, I quickly adapted to the new environment with the support from the whole group. Especially important is your guidance and encouragement, which helped me a lot in doing lab experiments, in running computer calculations, in writing publishable papers and the thesis here. Anouk, thanks a lot for your time and effort during the past two years. Your profound knowledge in the Spectroscopy field and your keep-improving spirit benefited me a lot. Also, your cheerful character makes our scientific life full of joy. Besides, you are greatly appreciated for your help with my personal career development: supporting me in job/postdoc applications and offering me necessary assistance in solving difficulties in life. Thanks a lot. It is a super wonderful experience to do a Phd research in your group.

Secondly, I would like to thank Prof. David H. Parker, my Phd 1st phase (Oct. 2010 - Sep. 2012) daily supervisor. Dave, thank you for offering me the chance to be here in Nijmegen to do my Phd. When we (my wife and I) arrived here on the first day, it was you picked us up at the station. Thanks a lot. At the start of my time in the lab, I really struggled, because of a big change in the area compared to that of my master project, and I could not find a feeling to get some nice results. However, you were always patient enough and explained me the project again and again. Sometimes you even came to the lab to show me the tricks in manipulating the instrument. Gradually, under your guidance, I got the control of the project and obtained more and more results, which finally resulted in my first paper. Dave, you are greatly appreciated for coaching and encouraging me, which makes me step into the correct way to get a Phd.

Third, I would also like to express my gratitude to Prof. Wim van der Zande, my other thesis Supervisor. Wim, I was deeply impressed by your flying-speed thinking in the first meeting with you. You are always so creative and full of solutions. It seems that no problem can really stump you. Working with you, people can easily get energized. Although not directly participating in your project, I still benefited a lot from discussion with you. Thanks a lot for your time and effort in helping me to improve the writing of my papers and thesis.

Moreover, I would like to say thanks to the following people for their great support and valuable suggestions to my Phd research: Giel, thanks a lot for your help with the OPO laser operation and beneficial discussions about various scientific problems, also thank you for the endless fun when talking with you in the party after class; Jos and Joost, thanks for your assistance in solving various problems occurred during running DFT calculations; Lex and Britta, without your contribution and effort, I could not acquire my far-infrared data before the termination of my Phd contract, thanks a lot; Andre (Eppink), I would also like to thank you so much for your help at the beginning of my Phd: planning travels to the conferences, organizing small group meetings, assisting me running experiments and correcting my writings, all you work is greatly appreciated; Bas (van de Meerakker), thanks a lot for your great experimental idea to characterize NPV (the 3rd chapter of this thesis); Also, I am very grateful to Dr. Isabelle Compagnon and Baptiste Schindler for their great support and help during my visit to their lab in Lyon (the work did there is described in chapter 6). Besides, I would also like to express my thanks to Leander, thank you for your countless technical support to my experiment and also thanks a lot for helping me in relocation, I hope you will fully recover.

Furthermore, the support from other members of the groups I stayed in are great appreciated. Magda and Miriam, thanks a lot for your assistance in dealing with various administrative works and also your effort in the organization of group activities. Rene, Theo, Michel, Andre (van Roij), Cor, Wouter, Arian, Brian, Guus, Peter and Chris, you are greatly appreciated for the technical support, which made my Phd work much more smooth.

In addition, I would like to express my acknowledgements to my colleagues: Sander, thanks a lot for your great help in teaching me to operate the setup and run the calculation. You are so good at making complex scientific issues into simple tasks that I mastered the research methods quickly by learning from you; besides, I also want to thank Daniel, Sjors,(thank you two for your time and effort in translating my English summary into Dutch), Jordy, Jonathan, Josipa, Juehan, Denis, Nico, Koen, Rob from Felix laboratory and Zahid, Gautum, Ashim, Chandan, Jolijn, Roy from MLF, it was so pleasant time to work together with you.

Of course, the acknowledgement should also be given to my Chinese friends. With their help, support and company, my life in the Netherlands can be so colourful. They are Baomin, Huairong, Mengzhi, Danni, Jiemeng, An Jie, Xumin, Tan Tao, Yuwei, An An, Weibin, Xie Fang, Wensi, Li Chong and Tianhong. It is such a nice experience to get along with you. Besides, I would also say thanks to Yifan, with whom I had lots of fun when talking, taking dinner and watching football matches together. Hope we could have a chance to visit San Siro soon.

Last but not least, I want to thank the most important people in my life: my families. 继玉，感谢你陪伴我来到这个陌生的过度，让我在他乡求学时还能感受到家庭的温暖。感谢你这几年来无私的奉献，照顾我的饮食起居。每天下班一回到家，我都能享用到丰盛可口的饭菜，倍感幸福。在荷兰的这段时间，与你一起畅游了欧洲的很多国家和景点，我们自己安排所有的行程，经过繁琐但体验却很

美妙。希望我们能一起走遍世界的每个角落。此外，我还想就过去生活上的一些小摩擦给你带来的委屈深表抱歉，我十分感激你的包容，无以回报。同时，最令我感动的是在我完成学业的这一刻，我们的孩子即将出生，感谢你带给我们这份珍贵的礼物。你是这个世界最可爱的人。我还得感谢我的父母：爸，妈，你们含辛茹苦抚养我，教育我，省吃俭用供我求学一直到现在，我真的很感激你们；自从读大学，我就离开了你们的身边，每年只有寒暑假短短个把月能与你们团聚，直到后来出国留学，跟你们在一起的时间就更少了，每周跟你们通电话时我都能感受到你们深深的牵挂，对于不能陪伴你们身边我很愧疚。如今我已学成，虽然今后的路还很长，但我相信一定会有更多的时间多陪陪你们。爸，妈，你们辛苦了，谢谢你们。此外，我还得感谢小舅，谢谢你一如既往的在物质上的支持和在精神上的鼓励，谢谢你在我不在的时候对我父母给予的关照。没有你的帮助，我不可能这么安心顺利地完成学业。你在这个家里总是任劳任怨，操心各种琐碎繁杂大大小小的事，对此我深表感激，谢谢你对于我和对整个大家所做的一切。同时，我还要感谢其他的家庭成员：小舅妈，大舅，大舅妈，姑姑，大伯，感谢你们无微不至的关心和帮助，让我每次回国都能感受到浓浓的亲情。最后，我还想借此论文告慰因在外求学而错失最后一面的外婆和爷爷，对不起不能送你们最后一程，我永远爱你们。

Curriculum vitae

Bin Yan
Born on 23rd August, 1985
In Zhenjiang, Jiangsu Province, China

10. 2010 - 02. 2015	Phd student in the Department of Molecular and Biophysics / Molecular and Laser Physics Radboud University Nijmegen, The Netherlands
09. 2007 - 06. 2010	Master of Science in Analytical Chemistry Xiamen University, China Thesis title: Laser ionization time-of-flight mass spectrometry for speciation analysis
09. 2003 - 06. 2007	Bachelor of Science in Chemistry Xiamen University, China